Cell

A convergent uPAR-positive tumor ecosystem creates broad vulnerability to CAR T cell therapy

Graphical abstract

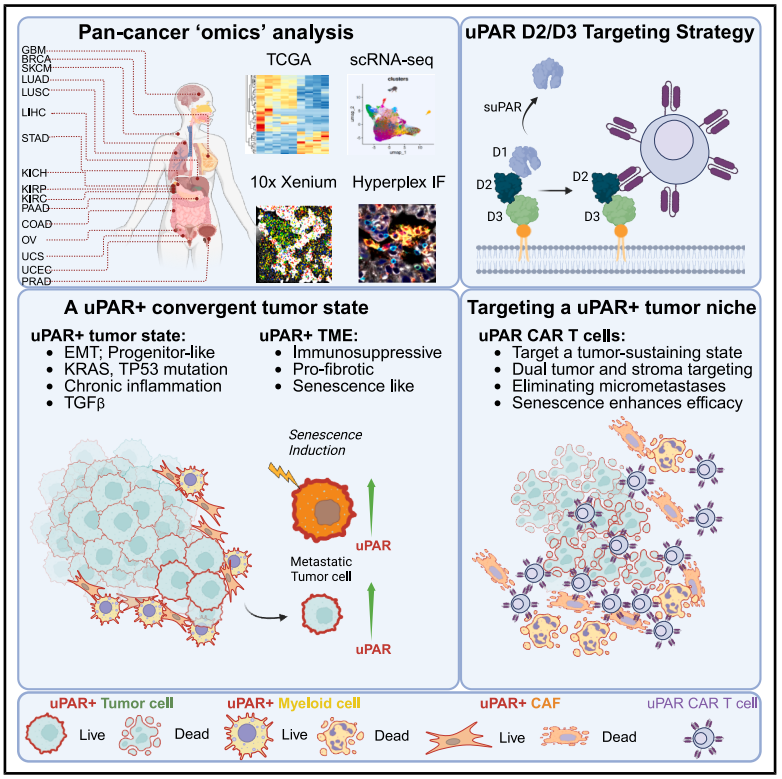

Highlights

- uPAR marks p53-mutant tumors with fibrotic, immunosuppressive niches
- uPAR CAR T cells target both tumor cells and their supportive stroma
- uPAR CAR T cells clear primary and metastatic tumors with minimal myelodepletion
- Senescence-inducing therapies upregulate uPAR and enhance uPAR CAR T cell efficacy

Authors

Zeda Zhang, Yu-Jui Ho, Xin Fang, ..., Aveline Filliol, Michel Sadelain, Scott W. Lowe

Correspondence

filliola@mskcc.org (A.F.), mws2188@cumc.columbia.edu (M.S.), lowes@mskcc.org (S.W.L.)

In brief

Synergizing with senescence-inducing therapies, uPAR CAR T cells eradicate primary and metastatic solid tumors with minimal myelodepletion by targeting both tumor cells and the stroma in preclinical models.

Zhang et al., 2026, Cell *189*, 2898–2917
May 14, 2026
https://doi.org/10.1016/j.cell.2026.03.002

CellPress

CellPress
OPEN ACCESS

Cell

Article

A convergent uPAR-positive tumor ecosystem creates broad vulnerability to CAR T cell therapy

Zeda Zhang,[1] Yu-Jui Ho,[1] Xin Fang,[1] Minseo Kim,[1,2,27] Marguerite Li,[1,27] Wei Luan,[1] Clemens Hinterleitner,[1] Sascha Haubner,[3] Friederike Kogel,[4] Edwin C. Pratt,[5] Elif Ozcelik,[1,2] José Reyes,[1,6] Qingwen Jiang,[5] Vincent W. Yang,[1] Yu-Jung Chen,[1] Tao Wang,[1,2] Haijiao Liu,[7] Haonan Hu,[7] Xueqian Zhuang,[1] Jin Park,[6] Stella V. Paffenholz,[1,8] Kevin Chen,[9] Qing Chang,[9] Amanda Kulick,[9] Jing Zhang,[4] Eric Chan,[10] Eric Rosiek,[10] Ning Fan,[10] Riley A. Williams,[9] Adam C. Wang,[11] Samuel Freeman,[12] Sha Tian,[1] Gertrude Gunset,[3] Andreina Garcia Angus,[3] Nicolas Lecomte,[13] Selma Yeni Yildirim,[13] Emily Ali,[13] Michelle Wu,[12] Ileana C. Miranda,[14] Cristina R. Antonescu,[13] Olca Basturk,[13] Zeynep Tarcan,[13] Natasha Rekhtman,[13] Christina Wilson,[13] Merve Basar,[13] Jennifer L. Sauter,[13] Hikmat A. Al-Ahmadie,[13] Samuel Singer,[15] Christine Iacobuzio-Donahue,[13] Charles Rudin,[5,15] Elisa de Stanchina,[9] Karuna Ganesh,[5] Paul B. Romesser,[16] Britta Weigelt,[13] Dan Dongeun Huh,[7] Josef Leibold,[17] Judith Feucht,[18] Ignacio Vázquez-García,[12,19,20] Matthew J. Bott,[21] Dmitriy Zamarin,[22] Sohrab P. Shah,[12] Jason S. Lewis,[5,23] Corina Amor,[24] Dana Pe'er,[6,26] Jorge Mansilla-Soto,[25] Aveline Filliol,[1,*] Michel Sadelain,[3,*] and Scott W. Lowe[1,26,28,*]

[1]Cancer Biology and Genetics Program, Memorial Sloan Kettering Cancer Center, New York, NY, USA
[2]Weill Cornell Graduate School of Medical Sciences, New York, NY, USA
[3]Columbia Initiative in Cell Engineering and Therapy, Department of Medicine, Columbia University, New York, NY, USA
[4]Immunology Program, Memorial Sloan Kettering Cancer Center, New York, NY, USA
[5]Molecular Pharmacology Program, Memorial Sloan Kettering Cancer Center, New York, NY, USA
[6]Computational and Systems Biology Program, Memorial Sloan Kettering Cancer Center, New York, NY, USA
[7]Department of Bioengineering, University of Pennsylvania, Philadelphia, PA, USA
[8]Gerstner Sloan Kettering Graduate School of Biomedical Sciences, New York, NY, USA
[9]Antitumor Assessment Core Facility, Memorial Sloan Kettering Cancer Center, New York, NY, USA
[10]Molecular Cytology Core Facility, Memorial Sloan Kettering Cancer Center, New York, NY, USA
[11]Weill Cornell/Rockefeller/Sloan Kettering Tri-Institutional MD-PhD Program, New York, NY, USA
[12]Computational Oncology, Department of Epidemiology and Biostatistics, Memorial Sloan Kettering Cancer Center, New York, NY, USA
[13]Department of Pathology and Laboratory Medicine, Memorial Sloan Kettering Cancer Center, New York, NY, USA
[14]Laboratory of Comparative Pathology, Memorial Sloan Kettering Cancer Center, Weill Cornell Medicine, and The Rockefeller University, New York, NY, USA
[15]Department of Medicine, Memorial Sloan Kettering Cancer Center, New York, NY, USA
[16]Department of Radiation Oncology, Memorial Sloan Kettering Cancer Center, New York, NY, USA
[17]Cluster of Excellence iFIT (EXC 2180) "Image-guided and Functionally Instructed Tumor Therapies", Department of Medical Oncology and Pneumology, University Children's Hospital Tübingen, Germany
[18]Cluster of Excellence iFIT, (EXC 2180) "Image-guided and Functionally Instructed Tumor Therapies", University Children's Hospital Tübingen, Tübingen, Germany
[19]Department of Pathology, Center for Cancer Research, Massachusetts General Hospital and Harvard Medical School, Boston, MA, USA
[20]Broad Institute of MIT and Harvard, Cambridge, MA, USA
[21]Thoracic Service, Department of Surgery, Fiona and Stanley Druckenmiller Center for Lung Cancer Research, Memorial Sloan Kettering Cancer Center, New York, NY 10065, USA
[22]Precision Immunology Institute, Icahn School of Medicine at Mount Sinai, New York, NY, USA
[23]Department of Radiology, Memorial Sloan Kettering Cancer Center, New York, NY, USA
[24]Cold Spring Harbor Laboratory, New York, NY, USA
[25]Departments of Immunology, Bioengineering, Blood and Marrow Transplant and Cellular Immunotherapies, H. Lee Moffitt Cancer Center and Research Institute, Tampa, FL, USA
[26]Howard Hughes Medical Institute, Memorial Sloan Kettering Cancer Center, New York, NY, USA
[27]These authors contributed equally
[28]Lead contact
*Correspondence: filliola@mskcc.org (A.F.), mws2188@cumc.columbia.edu (M.S.), lowes@mskcc.org (S.W.L.)
https://doi.org/10.1016/j.cell.2026.03.002

SUMMARY

Chimeric antigen receptor (CAR) T cells have transformed hematologic cancer therapy but remain limited in solid tumors by antigen heterogeneity and a suppressive, pro-fibrotic microenvironment. We previously identified the urokinase plasminogen activator receptor (uPAR) as upregulated in senescent, pro-fibrotic cells and showed that uPAR-directed CAR T cells could safely reverse fibrosis in mice. Integrative analyses now reveal that uPAR is broadly expressed in solid tumors enriched for *TP53* and RAS pathway mutations.

These tumors adopt a progenitor-like state supported by a niche of uPAR-positive stromal cells with senescence features. Human uPAR CAR T cells eliminate tumor cells and their stromal support, induce durable regressions across diverse models, eradicate systemic metastases, and are potentiated by senescence-inducing therapies. Importantly, these cells achieve robust antitumor activity without sustained myelosuppression in mice reconstituted with human immune systems. Together, these findings establish uPAR as a broadly applicable CAR T target capable of overcoming major barriers in solid tumor therapy.

INTRODUCTION

Chimeric antigen receptor (CAR) T cell therapy has transformed the treatment of hematologic malignancies, with CD19-directed products achieving durable remissions in otherwise refractory disease.[1,2] More recently, the extension of CD19 CAR T cells into autoimmune indications has demonstrated that engineered T cells can be harnessed to eliminate pathogenic but non-malignant populations,[3,4] underscoring the broader potential of adoptive cell therapy beyond oncology. However, CAR T cells have shown limited efficacy in solid tumors, largely due to heterogeneous antigen expression and an immune-suppressive, fibrotic tumor microenvironment (TME) that restricts T cell infiltration and function.[5,6] Current strategies rely on lineage-restricted/biased targets such as CD19, FOLR1, or prostate-specific membrane antigen (PSMA), which constrain applicability and fail to address aggressive tumor states that drive progression and resistance.[7] Overcoming these barriers will require targets that demarcate dynamic, tumor-maintaining cell states while enabling simultaneous remodeling of the pathological TME.

The urokinase plasminogen activator receptor (uPAR) may exemplify such a target. uPAR is a glycosylphosphatidylinositol-anchored receptor that regulates pericellular proteolysis, extracellular matrix (ECM) remodeling, and cell migration during wound healing.[8,9] Its expression is minimal in most normal tissues, except for subsets of myeloid cells, yet it is consistently upregulated in malignant and fibrotic contexts, where high levels correlate with poor clinical outcome.[10–14] Functional studies link uPAR to metastasis,[15–18] while in fibrosis, aberrant expression contributes to chronic inflammation and pathological tissue remodeling.[19] Inflammatory environments can also promote proteolytic cleavage of uPAR—most often within the D1 domain—releasing soluble uPAR (suPAR), a validated biomarker of disease severity in chronic kidney disease, cirrhosis, and idiopathic pulmonary fibrosis.[19–21] Together, these observations suggest that uPAR marks and reinforces aggressive, therapy-refractory disease states embedded within fibrotic and immune-suppressive niches.

Our interest in uPAR emerged from studies of cellular senescence, a growth-arrest program that suppresses tumor initiation but drives fibrosis, immune suppression, and tissue dysfunction when senescent cells accumulate.[22–24] uPAR is consistently induced in fibroblasts, macrophages, and other cell types that adopt senescent-like states during fibrosis,[25] and it is similarly upregulated in cancer following cytotoxic or targeted therapies that induce therapy-associated senescence.[25,26] In preclinical models of fibrosis and aging, uPAR-directed cellular therapies selectively eliminated senescent cells, reduced fibrosis, restored organ function, and were well tolerated even after long-term persistence.[25,27–30]

Here, we establish uPAR as a broadly expressed cancer target that marks aggressive tumor states defined by distinctive molecular and microenvironmental features, including their embedding within pro-fibrotic niches enriched for uPAR-positive stromal cells with senescence-associated programs. We further show that uPAR CAR T cells exhibit potent activity across diverse cancer models, enhanced by senescence-inducing therapies that increase antigen density, and that targeting uPAR enables simultaneous elimination of malignant cells and the pathological stromal compartments that sustain immune exclusion (where effector T cells are confined to the peritumoral stroma, with poor penetration into tumor nests) and therapeutic resistance. Together, these findings provide a framework for next-generation CAR T cell therapies that transcend lineage, dismantle tumor-maintaining ecosystems, and may extend beyond oncology to fibrotic and degenerative diseases.

RESULTS

uPAR defines a conserved molecular tumor state

Previous studies indicate that uPAR is overexpressed in some cancers, but a systematic pan-cancer analysis was lacking. We analyzed expression of the uPAR-encoding gene, *PLAUR*, in publicly available bulk RNA sequencing (RNA-seq) data derived from >10,000 tumor samples and organ-matched normal tissues across 14 tumor types. Transcriptomic analysis revealed that *PLAUR* expression is significantly elevated in 12 of these 14 types, with particularly high levels in subsets of ovarian, pancreatic, colon, lung, and brain cancers (Figure S1A).

Because bulk RNA-seq analysis cannot distinguish stromal from tumor-cell uPAR expression, we performed 4–5 markers multiplexed immunofluorescence (multi-IF) analysis in 1,074 patient tumors spanning multiple cancer types and histologic subtypes, incorporating antibodies against uPAR and markers that distinguish tumor cells (e.g., pan-cytokeratin [PanCK] and mutant p53) from immune cells (e.g., CD45) and stromal cells (e.g., alpha smooth muscle actin [αSMA]) (Figure 1A; Data S1.1). Tumor-associated uPAR expression was quantified by scoring uPAR-positivity in tumor cells (PanCK+, or, for brain tumors and sarcomas, by scoring cells negative for stromal and immune markers) across tissue microarrays (TMAs) and whole sections. Based on the percentage of uPAR+ tumor cells, tumors were stratified as high, intermediate, low, or negative (>50%, 30%–50%, 5%–30%, and <5%, respectively) (Figures 1A and S1B). Using these criteria, ∼15% of tumors exhibited high uPAR expression in the tumor compartment, with frequencies

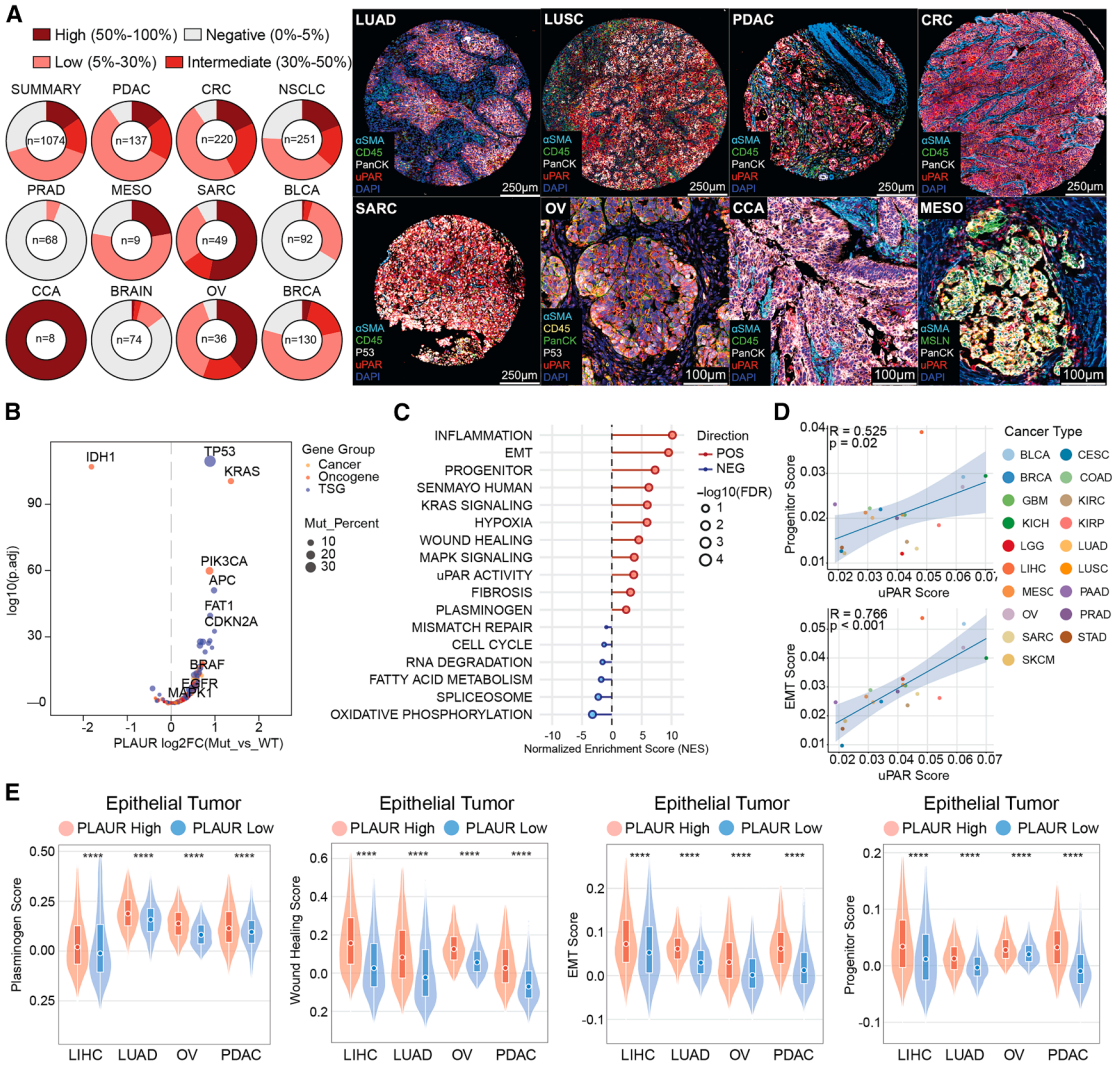

Figure 1. uPAR marks a distinct cell state enriched in *TP53* mutations and EMT programs

(A) Multiplex immunofluorescence (multi-IF) across human tumor samples. Left: representative cores stained for uPAR, tumor cells (PanCK, p53, or MSLN), fibroblasts (αSMA), immune cells (CD45), and nuclei (DAPI). Right: donut plots showing the fraction of samples per tumor type stratified by the percentage of uPAR+ tumor cells: high (>50%), intermediate (30%–50%), low (5%–30%), and negative (<5%), and *n* indicates the number of patients analyzed per tumor type or number of tumors for OV and BLCA (patient information in Table S1A).

(B–D) The Cancer Genome Atlas (TCGA) analysis (*n* = 10,071) showing (B) *PLAUR* expression stratified by mutation status across 456 cancer-relevant genes (MSK-IMPACT)[31]; (C) pathway enrichment in *PLAUR*-high (>66th percentile) versus *PLAUR*-low (<33rd percentile) tumors; and (D) correlation of uPAR activity with the indicated transcriptional signatures across cancer types (each dot represents one cancer type).

(E) scRNA-seq analysis of epithelial tumor cells from liver (*n* = 79), lung (*n* = 9), ovarian (*n* = 41), and pancreatic (*n* = 16) cancers comparing *PLAUR*-high (>66th percentile) and *PLAUR*-low (<33rd percentile) for the indicated signatures.BLCA, bladder urothelial carcinoma; BRAIN, brain tumor (multiple subtypes); BRCA, breast invasive carcinoma; CCA, cholangiocarcinoma; CRC, colorectal cancer; MESO, mesothelioma; NSCLC, non-small-cell lung cancer; OV, ovarian cancer; PDAC, pancreatic ductal adenocarcinoma; PRAD, prostate adenocarcinoma; SARC, sarcoma.

Statistics: Wilcoxon test (B and E), permutation test (C), and Pearson correlation test (D). Scale bars, 100 or 250 μm.

See also Figure S1.

ranging from 0% to 100% across tumor types (Figure 1A; Tables S1A and S1B).

uPAR-high tumors have been linked to aggressive molecular and clinical features.[12] To systematically evaluate these associations, we integrated genomic, transcriptomic, and clinical data from >10,000 patients across 19 cancer types. *PLAUR*-high tumors were strongly enriched for inactivating *TP53* mutations and activating alterations in *KRAS* and other mitogen-activated protein kinase (MAPK) pathway genes (e.g., *BRAF* and *EGFR*) (Figure 1B; Data S1.2). Although not universal, these associations were observed within many tumor types (Figure S1C; Tables S1C and S1D), suggesting shared genetic drives

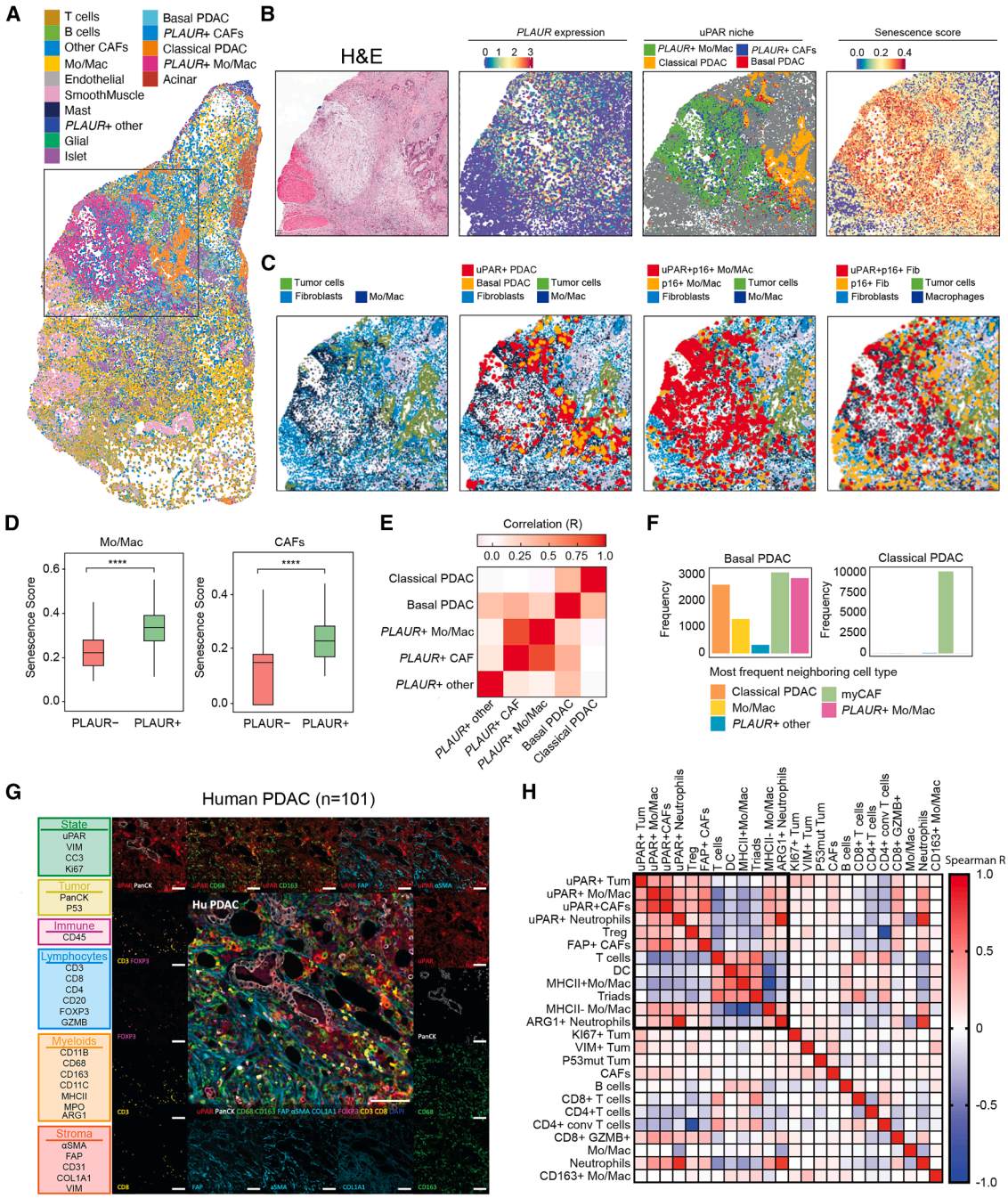

Figure 2. uPAR+ tumor, CAF, and myeloid cells define a fibrotic, immunosuppressive niche

(A and B) Spatial transcriptomics (10× xenium) of a treatment-naive human PDAC specimen showing the cell-type map (A) and H&E staining from an adjacent section with xenium feature plots of *PLAUR* expression, *PLAUR*+ cells, and senescence signature scores (B). Full sections are shown in Data S1.3E.

(C) Multi-IF-based spatial map from an adjacent section showing enrichment of uPAR+ PDAC cells near uPAR+/p16+ stromal cells. Cell types: tumor cells (PanCK+), fibroblasts (α SMA+), monocytes/macrophages (Mo/Mac and CD68+), and basal PDAC cells (KRT17+PanCK+).
Full sections are shown in Data S1.3H.

(D) Senescence scores in *PLAUR*+ versus *PLAUR*− Mo/Mac and CAF populations identified in (A).

(E) Spatial co-localization heatmap for selected cell populations (complete heatmap in Figure S2E).

(F) Frequency of neighboring cell types around basal versus classical PDAC neighborhoods.

(legend continued on next page)

underlying uPAR-high tumor-cell states. In other tumor types, non-genetic mechanisms such as stress and inflammation may also contribute.[32]

At the transcriptional level, stratifying tumors by high versus low *PLAUR* expression (top 1/3 versus bottom 1/3) revealed enrichment for programs linked to "plasminogen activation," "KRAS signaling," "EMT," "inflammation," "fibrosis," and "angiogenesis"—hallmarks of aggressive cancers with altered TMEs (Figures 1C and 1D).[33,34] This pattern was preserved within individual tumor types (Figures S1D and S1E; Table S1E). Analysis of publicly available single-cell RNA-seq (scRNA-seq) datasets from liver, lung, ovarian, and pancreatic cancers confirmed that *PLAUR*-high tumor cells share conserved transcriptional states[35–38] (Figure 1E). Consistent with prior reports,[10–14] high *PLAUR* expression was prominent in metastatic tumor cells (Figure S1F) and correlated with reduced overall, disease-free, and progression-free survival across most cancer types (Figure S1G; Data S1.2; Table S1F).

The convergence of *TP53* and MAPK pathway alterations with EMT-associated programs in uPAR-high tumors mirrors functional studies in mice showing that p53 is selectively activated in a uPAR-expressing, progenitor-like state arising early during KRAS-initiated pancreatic tumorigenesis.[39] Although normally kept transient, this state dramatically expands upon p53 loss during malignant progression.[39] In human cancers, *PLAUR*-high tumors are enriched for the same progenitor-like EMT program (Figures 1C–1E and S1D), indicating that this p53-constrained state becomes a defining feature of advanced disease. These findings provide a mechanistic rationale for the association of uPAR expression with aggressive *TP53* mutant tumors.

uPAR defines a conserved fibrotic and immune-suppressive niche

Beyond the tumor-cell compartment, our multi-IF analyses revealed abundant uPAR+ stromal cells within the TME (Data S1.3A–S1.3B). Similar accumulation of uPAR+ fibroblasts and macrophages occurs in human and murine fibrosis models, where they adopt a senescent-like state that contributes to pathology.[25,28,29] Moreover, in early pancreatic neoplasia, the emergence of uPAR+ progenitor-like epithelial cells is accompanied by the co-evolution of a niche of uPAR+ fibroblasts and macrophages—also expressing senescence features.[39]

To define the spatial organization of *PLAUR+* cell states in advanced tumors, we first performed spatial transcriptomics (10× xenium) on a human primary pancreatic ductal adenocarcinoma (PDAC) sample using a curated marker panel (Figures 2A and S2A–S2C; Table S2A). Subpopulation analysis defined three *PLAUR*-high groups: (1) basal PDAC tumor cells (*HMGA2-high* and *ANXA10-low*; analogous to the progenitor-like state[39]), (2) a subset of *PDGFRA/B*+ cancer-associated fibroblasts (CAFs) expressing the myofibroblastic CAF (myCAF) marker *ACTA2* together with *SERPINE1* (hereafter uPAR+ CAF), and (3) a subset of *CD68+/MRC1+* monocytes and macrophages expressing *SPP1* (hereafter uPAR+ myeloid) (Figures S2B–S2E; Table S2B).

PLAUR-high tumor cells co-localized with stromal niches enriched for *PLAUR*+ CAFs and *PLAUR*+ myeloid cells (Figure 2B). Multi-IF of serial sections confirmed concordant spatial patterns of uPAR in tumor cells (Figure S2F) and revealed co-localization of collagen I-rich regions together with αSMA+ fibroblasts and CD68+ macrophages (Figure S2G). uPAR+ CAFs and myeloid cells were also enriched for senescence signature (see STAR Methods) and expressed the senescence marker p16 (Figures 2C, 2D, and S2H–S2J).

We next quantified local co-occurrence of cell states across 500-μm neighborhoods (see STAR Methods; Figure S3A). Correlation analysis revealed strong co-localization of uPAR+ basal PDAC cells with uPAR+ CAFs and uPAR+ myeloid subsets, a pattern largely absent from classical PDAC regions (Figure 2E). Basal PDAC cells typically localized to the periphery of tumor glands,[40] forming epithelial-stromal interfaces where diverse uPAR+ populations converged (Figure S3B). Permutation analysis further distinguished these niches, revealing greater cellular diversity in basal regions compared with more uniform, myCAF-dominated classical neighborhoods (Figure 2F). Together, these findings position basal PDAC as a spatial and functional transition zone between tumor epithelium and a complex uPAR+ stromal niche, contrasting with the more homogeneous classical subtype.[41]

To assess generalizability, we performed 24-plex hyperplex IF (defined as ≥20 markers cyclic IF) (see STAR Methods) on TMAs comprising >3.5 million cells from PDAC (n = 101), lung adenocarcinoma (LUAD) (n = 55), lung squamous cell carcinoma (LUSC) (n = 49), CRC adenocarcinoma (n = 137), and mucinous CRC (n = 51) (Figures 2G, 2H, and S3C; Data S1.3 and S1.4; Table S3). Across tumor types, uPAR+ tumor cells, myeloid cells (tumor-associated macrophages [TAMs] and tumor-associated neutrophils [TANs]), and CAFs consistently clustered, forming a conserved uPAR+ spatial niche (Figures 2G, 2H, and S3C; Data S1.3 and S1.4). Of note, a subset of uPAR+ tumor cells expressed the EMT marker vimentin (VIM) (Figure S3D). Although variable in magnitude, this niche was enriched for Tregs and exhibited features consistent with immune exclusion and immunosuppression (Figures 2G and 2H; Data S1.3 and S1.4). These associations were strongest in PDAC, where uPAR-positive regions harbored fewer conventional CD4+ T cells, dendritic cells, and major histocompatibility complex (MHC) class II+ TAMs, alongside expansion of FAP+ myCAFs, MHC class II$^-$ TAMs, and ARG1+ TANs, and fewer immune stimulatory DC-CD4-CD8 "triads."[42] Additionally, many uPAR+ fibroblasts co-expressed FAP (Figure S3E), a marker linked to T cell exclusion and resistance to immune checkpoint blockade.[43,44] Across cancers, uPAR+ tumor cells, CAFs, and myeloid populations consistently co-localized, indicating that uPAR marks a conserved pro-fibrotic and immunosuppressive niche rather than a tumor-type-restricted phenomenon.

(G and H) Hyperplex 24-plex IF images from PDAC tumors (n = 101 cases and 649,581 cells analyzed) (G) and Spearman correlation analysis among cell populations (quantification in Data S1.4A) (H).
Statistics: Wilcoxon test (D) and Spearman correlation (H) (p values shown in Figure S2H). Scale bar, 100 μm.
See also Figures S2 and S3.

To further characterize stromal states, we analyzed scRNA-seq data from human cancers (described in Figure 1E),[35–38] focusing on uPAR+ stromal populations. *PLAUR*-high CAFs expressed myCAF signatures and were enriched for senescence-related programs (senescence score, senescence-associated secretory phenotype [SASP] score, *CDKN2a*, and *CDKN1a*) relative to *PLAUR*-low CAFs (Figures S3F and S3G). In ovarian and liver cancers, *PLAUR* was also expressed in subsets of iCAFs. *PLAUR*-high myeloid cell populations also resembled previously described immune-suppressive subsets, including (1) angio-TAMs (SSP1+, angiogenic, immunosuppressive, and hypoxia-associated), (2) inflam-TAMs (neutrophil/monocyte-recruiting and necrosis-associated), and (3) interferon (IFN)-TAMs (Figure S3H).[45]

Finally, transcriptional signatures derived from *PLAUR* (uPAR)-positive fibroblast and myeloid subpopulations that surround uPAR+ progenitor-like epithelial cells in early murine pancreatic neoplasia[39] were preferentially enriched in uPAR-high CAFs and tumor-associated myeloid cells across liver, lung, ovarian, and pancreatic cancers (Figure S3I). Thus, the uPAR+ niche observed in premalignant pancreas is conserved across tumor types and defines spatially organized tumor-stroma ecosystems characterized by fibrosis, senescence, and immune exclusion—features linked to aggressive disease and poor outcome.

Broad antitumor activity of uPAR CAR T cells

The high expression of uPAR on tumor cells and senescent-like cells within the TME suggests that uPAR-targeted therapies, including CAR T cells, could disrupt uPAR+ niches and exert potent antitumor activity. To develop uPAR-directed CAR T cells, we performed hybridoma and phage-display screening, yielding a panel of single-chain fragment variants (scFvs) against human uPAR, including the less frequently shed D2-D3 domain (Figure 3A), and identified two lead candidates—uPAR T1 and uPAR A1 (see STAR Methods). In antibody format, both binders exhibit nanomolar affinity and D2-D3 domain selectivity, as confirmed by surface plasmon resonance analysis and competitive binding assays (Figures S4A–S4C).

To generate CAR T cells, T1 and A1 scFvs were cloned into an SFG-γ-retroviral vector encoding the human CD28 co-stimulatory and CD3ζ signaling domains (h.uPAR-T1-h.28z and h.uPAR-A1-h.28z). Transduced human peripheral blood T cells exhibited low tonic signaling, with minimal cytokine release (e.g., tumor necrosis factor alpha [TNF-α], IFN-γ, and interleukin [IL]-2) in the absence of antigen (Figure S4D). Upon co-culture with uPAR+ target cells, both CAR constructs induced robust T cell activation and antigen-dependent cytotoxicity, whereas untransduced T cells (UTD) or CD19 CAR T cells (h.19-h.28z) induced no activity (Figures S4D–S4F). *PLAUR*-deficient targets generated by CRISPR-Cas9 were resistant to killing, confirming on-target specificity (Figures S4E and S4F). These results establish T1 and A1 CARs as specific human uPAR CARs suitable for *in vivo* testing.

We next defined the antigen density required for cytotoxicity by quantifying surface expression across human cancer cells, using quantitative flow cytometry on 71 human cancer cell lines spanning 12 tumor types, together with two normal cell lines and a *PLAUR*-knockout (KO) control (Data S1.5A). We used quantitative flow cytometry with calibration beads and then converted mean fluorescence intensity to absolute molecule number, yielding a range from <100 to >60,000 molecules per cell (Figure 3B). uPAR CAR T cells displayed robust *in vitro* killing above a threshold of ∼1,500 molecules per cell (Figure 3B; Data S1.5B), whereas KO cells remained resistant (Figures S4E and S4F), supporting antigen engagement as the primary determinant of cytotoxicity. Expression of death receptors (CD95(FAS), DR1, DR2, DR4, and DR5) did not correlate with sensitivity as has been described in some contexts (Data S1.5C).[46,47] Using a D2-D3-specific binder versus a uPAR polyclonal antibody (pAb), we found that many cancer cell lines preferentially express the D2-D3 form under standard culture conditions (Data S1.5D).

uPAR CAR T cells exhibited potent antitumor activity *in vivo*. Across cell line-derived xenograft (CDX) models of lung, pancreatic, and ovarian cancers expressing 6,000–40,000 uPAR molecules per cell (Figures 3B and 3C), a single infusion of T1 CAR T cells induced rapid and durable tumor regressions and significantly extended survival, whereas CD19 CAR T cells had no effect (Figures 3D and 3E). Immunofluorescence at day 7 revealed dense infiltrates of granzyme B-positive CAR T cells (Figures 3F, S4G, and S4H). Similar efficacy was observed in nine additional CDX, patient-derived xenograft (PDX), and patient-derived organoid (PDO) models (Figures S5A–S5G). Notably, baseline heterogeneity of uPAR expression and fibrotic uPAR+ stroma—features also observed in patient tumors—did not prevent this response (Figures 1A, 3C, and S5D; Data S1.3B).

Although most tumors regressed durably, a subset relapsed with high uPAR expression, implying that antigen loss was not the mechanism of escape (Figures S5H and S5I). These data are consistent with reports indicating that uPAR can be required for aggressive cancer states,[32,48] and, indeed, CRISPR-mediated uPAR KO in ovarian cancer cells markedly impaired tumor growth and metastasis in both murine and human metastatic models (Figures S5J–S5L). Aiming to improve durability, we tested a next-generation "1.XX" CAR optimized for persistence and reduced dosing,[49,50] which produced more sustained tumor control than the 28z backbone in the ovarian PDX model (Figure S5G). These findings implicate CAR T cell exhaustion in relapse and highlight opportunities to enhance persistence to improve outcomes. Together, these results demonstrate that uPAR CAR T cells have potent and broadly effective antitumor activity.

uPAR CAR T cells eliminate ovarian cancer and its metastases

High-grade serous ovarian cancer (HGSOC) is a lethal malignancy with limited therapeutic options.[51] We analyzed whole-tissue sections from 36 HGSOC specimens obtained from the SPECTRUM cohort[37] (treatment-naive; n = 23) and the MSKCC Biobank (treated; 13 tumor sites from 9 patients). Multi-IF revealed that ∼40% of tumors exhibited high, tumor-cell-specific uPAR expression, defined by co-localization with PanCK and mutant p53 (Figures 4A, S6A, and S6B), the latter frequently stabilized owing to the near-universal *TP53* mutations in HGSOC.[52] As in other cancers, uPAR-high HGSOC typically

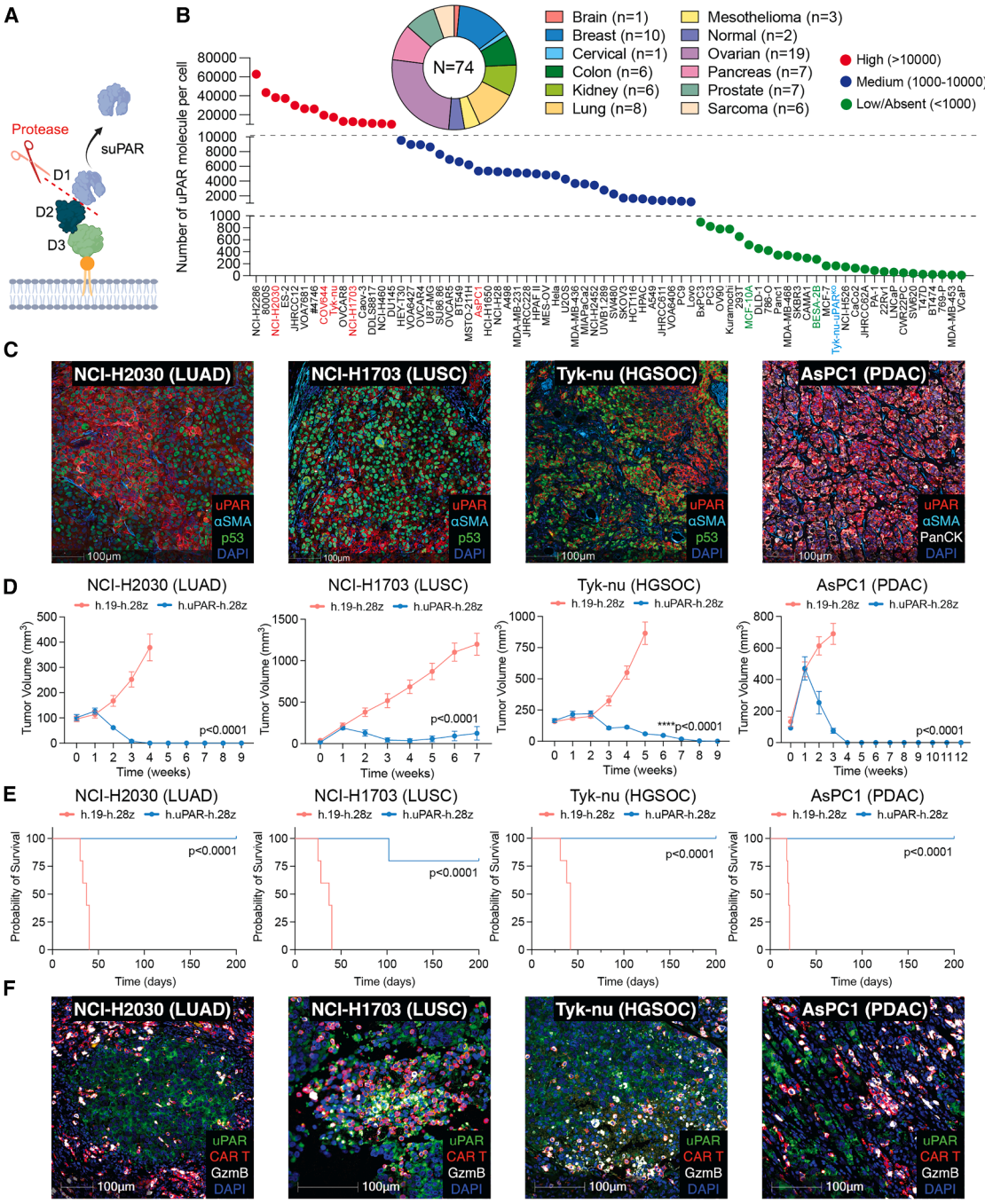

Figure 3. uPAR CAR T cells exhibit potent antitumor activity across multiple cancer models

(A) Schematic of uPAR proteolytic cleavage and release of soluble uPAR (suPAR). Created with BioRender.com.

(B) Quantification of uPAR surface density across 71 human cancer cell lines by flow cytometry. Non-cancer cells are indicated in green, uPAR-KO ($uPAR^{KO}$) in blue, and cell lines exhibiting durable *in vivo* tumor regression in red (see D and E).

(C) Multi-IF staining for uPAR in subcutaneous xenografts of lung adenocarcinoma (LUAD), lung squamous cell carcinoma (LUSC), high-grade serous ovarian carcinoma (HGSOC), and pancreatic ductal adenocarcinoma (PDAC).

(D–F) Antitumor efficacy of uPAR CAR T cells expressing the uPAR-binding scFv (T1-h.28z) versus a CD19 control CAR (h.19-h.28z), administered intravenously (2×10^6 cells per mouse): (D) tumor volume, (E) overall survival, and (F) CAR T cell infiltration assessed by anti-CD3 multi-IF staining 7 days after treatment. Statistics: multiple *t* test (D) and log-rank test (E). Error bars indicate SEM. Scale bar, 100 μm.

See also Figures S4 and S5.

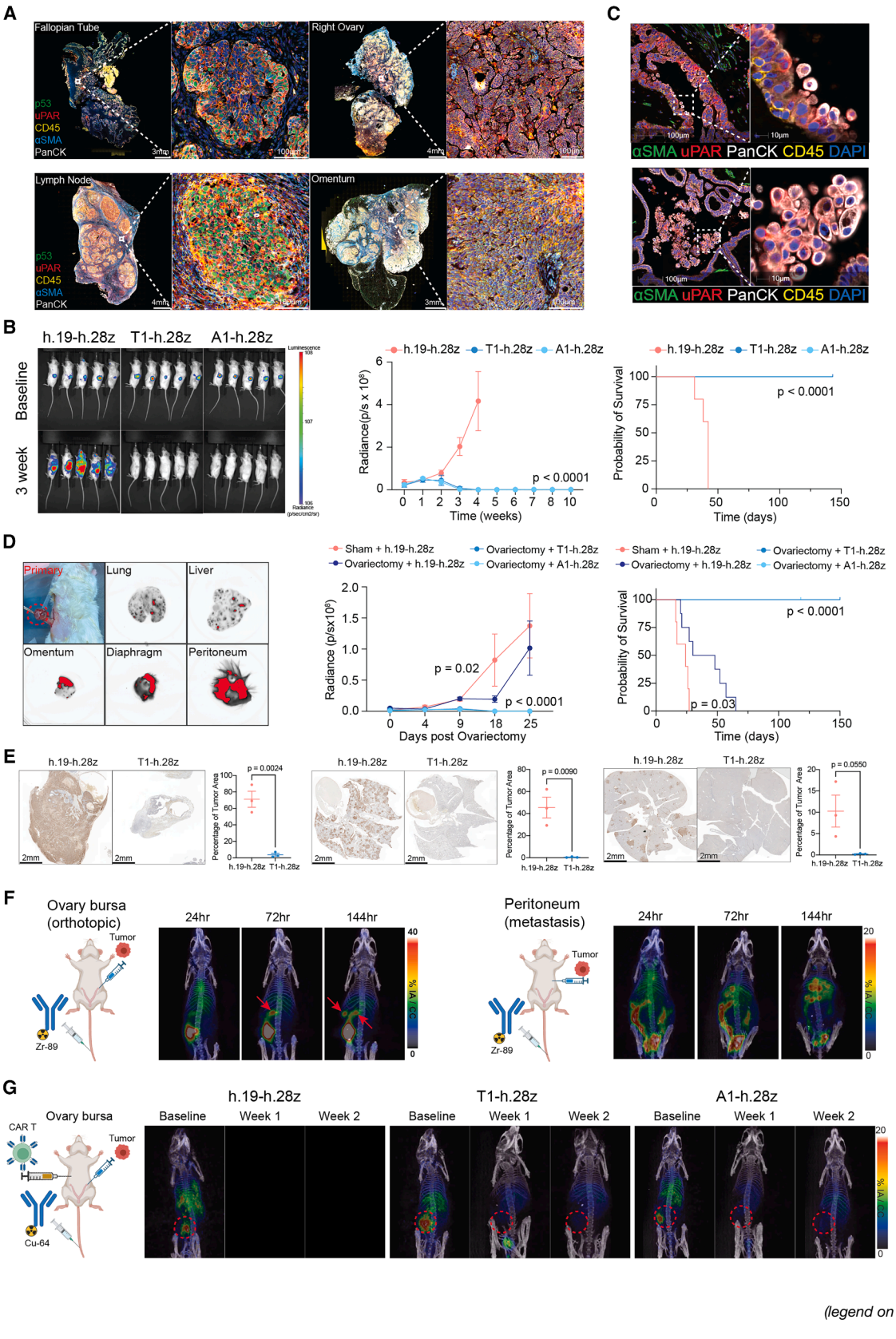

(legend on next page)

contained an abundance of uPAR-positive stromal cells (Figures 4A and S6A–S6C; Data S1.3B). High uPAR expression was associated with elevated transforming growth factor β (TGF-β) signaling but not with genomic subtype. Nevertheless, uPAR-high tumors were detected within aggressive HGSOC subsets harboring fold-back inversion (FBI) events or CCNE1 amplification (Figure S6D; Table S1G).[37]

To assess uPAR as a therapeutic target, we evaluated uPAR CAR T cell activity in both HGSOC and mucinous ovarian cancer (MOC) CDX and PDX models with uPAR expression. Tumors were engineered with firefly luciferase (Fluc), orthotopically implanted into the ovarian bursa of NOD scid gamma (NSG) mice, and treated with T1 or A1 h.uPAR CAR T cells or control h.CD19-28z CAR T cells. uPAR CAR T cells, but not controls, induced complete remissions across both (Figures 4B and S6E), with efficacy in HGSOC and MOC subcutaneous PDX models as well (Figures S5F and S5G). Post-treatment serum showed uPAR CAR T activation (TNF-α, IFN-γ, and granzyme B) (Data S1.6A–S1.6C), and peripheral blood at 8 weeks harbored circulating memory-enriched CD4+ and CD8+ populations (Data S1.6D). Functional persistence was confirmed by uPAR CAR T cell rechallenge: mice previously cleared of Tyk-nu tumors resisted parental but not uPAR-null tumor engraftment (Data S1.6E).

Multi-organ metastases are a major cause of mortality in advanced ovarian cancer,[53,54] as confirmed in the Memorial Sloan Kettering (MSK) pan-cancer metastasis cohort (Figure S6F). Consistent with a prior report, scRNA-seq of HGSOC samples from the MSKCC-SPECTRUM cohort[37] revealed particularly high *PLAUR* expression in tumor cells from ascites (Figures S6G, S6H, and S7A), and analysis of ovarian tissue sections revealed uPAR-high tumor cells at invasive fronts or in small detached tumor-cell clusters (Figures 4C and S7B). These results suggest that uPAR CAR T cells might have activity against disseminated disease.

In agreement, uPAR CAR T cells eradicated widespread intraperitoneal (i.p.) disease in Tyk-nu (HGSOC) and COV644 (MOC) metastasis models, with mice remaining tumor free for >150 days (Figures S7C and S7D). In an orthotopic spontaneous metastasis model incorporating debulking surgery to mimic an adjuvant clinical setting (Figures 4D and S7E), a single dose of 1×10^6 T1 or A1 uPAR CAR T cells eliminated residual disease, whereas surgery alone provided only transient benefit (Figures 4D, S7F, and S7G). CAR T cells infiltrated all metastatic sites, expressed granzyme B, and cleared detectable tumors (Figures 4E and S7H; Data S1.7A). Thus, uPAR-directed CAR T cells eradicate both established and disseminated ovarian cancer, including in clinically relevant adjuvant settings.

We next evaluated whether uPAR expression could enable non-invasive disease monitoring. The levels of suPAR—a biomarker of fibrotic and inflammatory pathology[55,56]—tracked tumor burden in HGSOC models, increasing in mice with uPAR$^+$ tumors and declining after therapy, as measured by human-uPAR-specific ELISA (Data S1.7B). We also developed ^{89}Zr-labeled T1 and A1 uPAR antibodies for positron emission tomography (PET) imaging, which detected orthotopic ovarian tumors, monitored progression, and identified distant metastases, confirmed by autoradiography (Figure 4F; Video S1). To enable longitudinal imaging, we generated a shorter-lived ^{64}Cu-labeled uPAR antibody ($t_{1/2}$ = 12 h versus 78.41 h for ^{89}Zr), capturing rapid tumor regression after uPAR CAR T cell therapy (Figure 4G). Together, these findings demonstrate that uPAR-directed CAR T cells can be highly effective against ovarian cancer models and support complementary suPAR- and PET-based strategies for real-time monitoring of therapeutic responses and recurrence.

uPAR CAR T cells can target both tumor and pro-fibrotic stroma

Our current results and prior work demonstrate potent activity of uPAR CAR T cells against tumors (this study) and fibrosis,[25] raising the possibility that uPAR CAR T cells may target both malignant tumor cells and the pro-fibrotic tumor stroma. Although our rapidly growing models do not achieve the entrenched stroma of human tumors, they contain substantial fibrotic components with strong murine uPAR expression (Figures 5A, S8A, and S8B). To test stromal targeting directly, we exploited species-selective recognition by our murine uPAR scFv (m.uPAR) in mice bearing orthotopic Tyk-nu HGSOC tumors or a head-and-neck PDX. Indeed, Gaussia-luciferase (Gluc)-labeled m.uPAR CAR T cells, but not h.CD19 controls, selectively homed to tumors, producing strong bioluminescent signals (Figures 5B and S8C).

Figure 4. Efficacy of uPAR CAR T cells in ovarian cancer xenografts

(A) Representative multi-IF images from the MSK SPECTRUM HGSOC cohort.

(B) Orthotopic ovarian cancer model (Tyk-nu^{luc}) treated with control CD19 CAR T cells (h.19-h.28z; 2×10^6) or uPAR CAR T cells (T1-h.28z or A1-h.28z; 2×10^6). Tumor burden was monitored by bioluminescence (images, left; quantification, middle) and overall survival (Kaplan-Meier, right).

(C) Multi-IF of a human HGSOC specimen showing uPAR-expressing tumor cells (left) and higher magnification views highlighting uPAR+ tumor cells within detached tumor-cell clusters (right).

(D) Spontaneous metastasis model using orthotopic Tyk-nu^{luc} xenografts. Left: *in vivo* imaging following oophorectomy and *ex vivo* bioluminescence of metastatic dissemination (see schematic in Figure S7E). Right: metastatic tumor burden (middle) and Kaplan-Meier survival analysis (right) after treatment with control or uPAR CAR T cells.

(E) Immunohistochemistry for GFP and quantification of tumor burden in the adnexa (left) and metastatic lesions in the lung (middle) and liver (right).

(F) Longitudinal ^{89}Zr-labeled uPAR PET imaging of primary (orthotopic; left) and metastatic (intraperitoneal; right) Tyk-nu tumors. Schematic created with BioRender.com.

(G) Longitudinal ^{64}Cu-labeled uPAR PET imaging of Tyk-nu tumors following treatment with control or uPAR CAR T cells at the indicated time points. Schematic created with BioRender.com.

Statistics: multiple *t* test (B, middle; D, middle), Student's *t* test (E), and log-rank test (B, right; D, right). Error bars indicate SEM (B and D) or SD (E).

See also Figures S6 and S7.

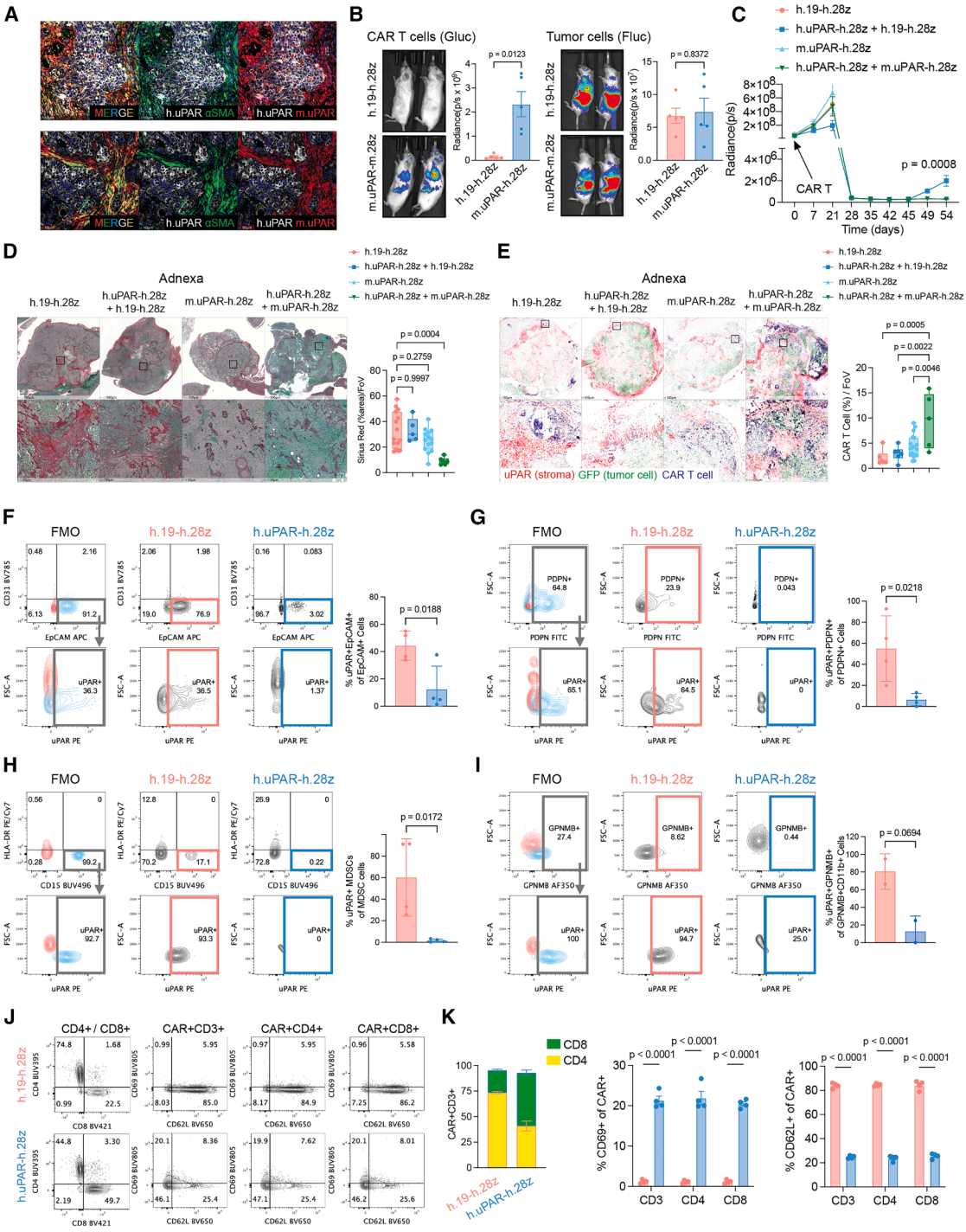

Figure 5. uPAR CAR T cells target both tumor cells and their fibrotic stroma

(A) Multi-IF images of orthotopic Tyk-nu (top) and COV644 (bottom) xenograft tumors showing human uPAR+ tumor cells and αSMA+ fibrotic murine stroma (left panel; scale bar, 50 μm) and murine uPAR+ stromal cells, including fibroblasts (αSMA+, right panel; scale bar, 10 μm).

(B) *In vivo* bioluminescence imaging of Gaussia-luciferase (Gluc)-labeled CAR T cells expressing a murine uPAR-targeting CAR (m.uPAR-h.28z) or control CD19 CAR (h.19-h.28z) in mice bearing orthotopic Tyk-nu^{luc} tumors expressing firefly luciferase (Fluc). Mice were imaged using a Gluc substrate (stromal targeting) or a Fluc substrate (tumor burden) 24 h after intravenous CAR T cell infusion and 4 weeks after tumor implantation, and radiance quantification is shown (n = 5 mice).

(C) Fluc tumor burden in mice bearing orthotopic Tyk-nu^{luc} tumors treated with h.19-h.28z, h.uPAR-h.28z, m.uPAR-h.28z, or combinations, and CAR T cell infusion timing is indicated (n = 5 mice)

(legend continued on next page)

We next used the species specificity of uPAR scFvs to isolate the contribution of stromal targeting to uPAR CAR T therapeutic efficacy. Because high-dose h.uPAR CAR T cells (2×10^6) typically produce complete remissions, we administered a subtherapeutic dose (0.5×10^6) alone or combined with m.uPAR CAR T cells for stromal targeting or h.CD19 controls. In both orthotopic and metastatic Tyk-nu models, h.uPAR CAR T alone produced transient responses that relapsed by 7 weeks, whereas dual tumor-stroma targeting sustained tumor control (Figures 5C and S8D–S8E). Dual tumor-stroma targeting also produced marked reductions in fibrosis across ovarian, lung, and liver lesions (Figures 5D and S8F), accompanied by increased infiltration of h.uPAR CAR T cells at primary and metastatic sites (Figures 5E and S8G).

We further evaluated whether h.uPAR CAR T directly targets stromal populations from human tumors. Tumors from surgical resections (4 HGSOC and 1 LUAD) were dissociated and co-cultured with h.uPAR CAR T cells or h.CD19 CAR T cells. After 16 h, flow cytometry revealed that uPAR CAR T cells selectively eliminated uPAR+ tumor cells (EpCAM+), CAFs (PDPN+), and myeloid-derived suppressor cells (MDSCs, CD45+Lin−CD11b+CD14−HLADR−CD15+ or CD45+Lin−CD11b+GPNMB+)[57] (Figures 5F–5I, S8H, and S8I). Orthogonal assays confirmed uPAR CAR T cells directly target and kill patient-derived primary CAFs and immunosuppressive M2-like macrophages generated from peripheral blood monocytes (Figures S9A–S9F). In these cultures, uPAR CAR T cells, compared with CD19 control, exhibited a higher CD8/CD4 ratio and increased activation (with increased CD69 and decreased CD62L expression) across both CD4 and CD8 T cell subsets, consistent with productive antigen engagement (Figures 5J, 5K, S9G, and S9H). While neither mouse models nor *ex vivo* tumor suspensions capture the clinical setting, these data indicate that uPAR CAR T cells are uniquely capable of targeting both tumor and stromal compartments.

Safety profile of uPAR CAR T cells

uPAR is absent or lowly expressed in most vital organs but detectable on a subset of myeloid cells.[25] Prior studies showed that high doses of murine uPAR CAR T cells (3×10^6) caused transient weight loss and cytokine release syndrome, whereas lower doses (still sufficient to ameliorate fibrosis and metabolic syndrome, including in aged mice) were well tolerated, with CAR T cells persisting for >1 year.[25,30] To further assess on-target/off-tumor risk, we quantified uPAR expression across normal tissues using The Cancer Genome Atlas (TCGA) and the Human Protein Atlas, benchmarking uPAR against other clinically targeted cell-surface proteins. *PLAUR* was selectively enriched in tumors relative to matched normal tissues, and uPAR protein expression in adult tissues was largely restricted to myeloid cells (Figure S10A). Expression in vital organs was substantially lower than that of PSMA and TROP2 (Figures S10B and S10C), two cell-surface proteins targeted by FDA-approved therapies.

Given the risk of cytokine release syndrome at high CAR T cell doses and the dose-limiting hematologic toxicities of many anticancer treatments, we rigorously evaluated the safety of uPAR CAR T cells in tumor-bearing mice under conditions of robust on-target engagement. One approach used an electroporation-based genetically engineered ovarian cancer mouse model (EPO-GEMM) (Figure 6A)[58] driven by MYC overexpression with *Trp53* deletion (MP) or combined *Trp53* plus *Brca1* deletion (MPB1). These tumors spontaneously metastasized i.p., including the omentum, and frequently produced ascites[58] (Figures 6B and 6C). Immunohistochemistry of primary tumors and flow cytometry of MP/MPB1 tumor-derived cell lines revealed spontaneous upregulation of surface uPAR during tumorigenesis (Figures 6C and S10D).

Murine uPAR CAR T cells (m.uPAR-m.28z[25]) secreted cytokines and exhibited potent cytotoxicity against MP or MPB1 cells *in vitro* but not against CRISPR-engineered uPAR-deficient derivatives (Figures S10D–S10F). *In vivo*, treatment of autochthonous MP tumors induced robust tumor regression and significantly extended survival (Figure 6D), whereas untransduced T cells had no effect. Similar activity was observed in an i.p. MPB1 metastasis model (Figure S10G). Treated mice exhibited only transient weight loss, and peripheral blood analysis at remission showed no sustained perturbation of myeloid or other immune cell compartments at 1 month (Figures 6E, 6F, and S10H), indicating effective tumor control without overt toxicity.

To assess potential toxicities of human uPAR CAR T cells, we performed parallel studies in mice reconstituted with a human immune system.[59] Human hematopoietic stem and progenitor cells (HSPCs) restored lymphoid and myeloid compartments,

(D) Sirius red staining of lung metastasis sections from Tyk-nu^{luc}-bearing mice treated with the indicated CAR T cells, with quantification of fibrosis area per field of view (FoV) using Fiji (see STAR Methods) (n = 5 mice). Scale bars, 1 mm (top) and 50 μm (bottom).
(E) Multi-IF of Tyk-nu lung metastases showing m.uPAR+ stromal cells (red), GFP+ tumor cells (green), and CD3+ CAR T cells (blue) after treatment. Pseudocolor images and quantification of CAR T cell infiltration per FoV (n = 5 mice). Scale bars, 10 μm.
(F–I) Flow cytometry of dissociated human HGSOC tumors after 16 h co-culture with the indicated CAR T cells (representative gating and quantification; n = 4 patients): (F) EpCAM+ tumor cells and the fraction of uPAR+EpCAM+ cells within EpCAM+ cells; (G) PDPN+ CAFs and the fraction of uPAR+PDPN+ cells within PDPN+ cells. Parental gate: live+CD45-CD31-EpCAM−; (H) MDSCs (CD45+Lin−CD11b+CD14−HLA−DR−CD15+; Lin− excludes CD3/CD19/CD56) and the fraction of uPAR+MDSCs; (I) GPNMB+CD11b+ myeloid cells (CD45+Lin−CD11b+GPNMB+; Lin− excludes CD3/CD19/CD56) and the fraction of uPAR+GPNMB+ cells within GPNMB+CD11b+ myeloid cells.
(J and K) Flow cytometry analysis of CAR T cells following co-culture with primary HGSOC CAFs (n = 4).
(J) Representative flow cytometry plots showing the percentages of CD4+ and CD8+ CAR T cells, as well as CD69+/CD62L+ cells within the CD4+ or CD8+ CAR T populations.
(K) Quantification of the data shown in (J). CAR expression was assessed by LNGFR staining.
In all flow cytometry plots, positive gates were defined using fluorescence minus one (FMO) controls. Statistics: Student's t test (B and F–I), multiple t tests (C), and one-way ANOVA (D, E, and K). Error bars indicate SEM (C) or SD (F–K).
See also Figures S8 and S9.

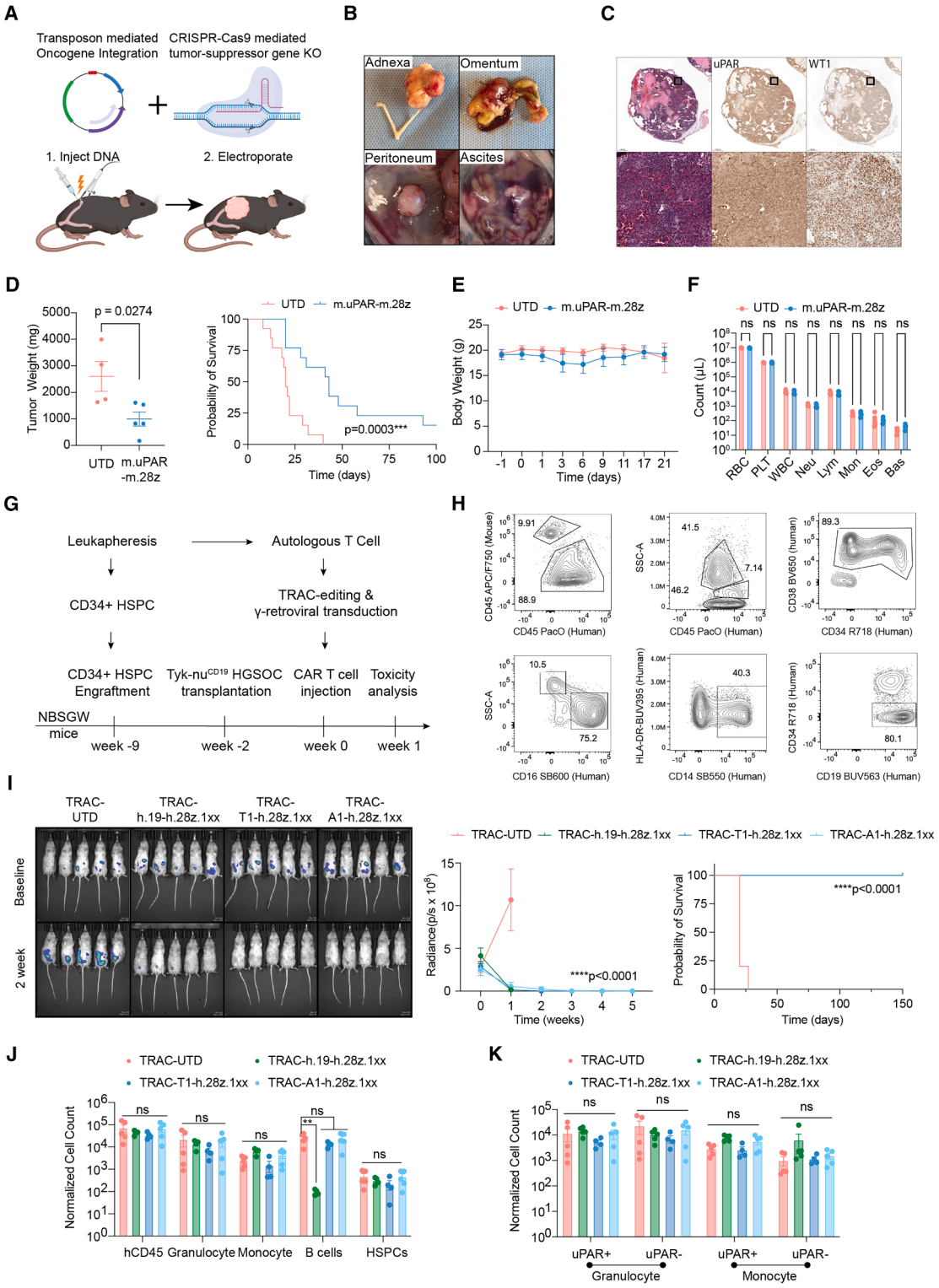

Figure 6. uPAR CAR T cells exhibit a favorable safety profile

(A) Schematic of the electroporation-based genetically engineered mouse model (EPO-GEMM) enabling transposon-mediated oncogene integration (*MYC*) and CRISPR-Cas9-mediated tumor suppressor KO (*Trp53* and *Brca1*) in the ovary/fallopian tube to generate autochthonous ovarian tumors. Created with BioRender.com.

(B) Representative images of established *MYC*^{OE}; *Trp53*^{KO} EPO-GEMM tumors, and spontaneous metastases.

(legend continued on next page)

including uPAR-expressing monocytes (Figures 6G, 6H, and S11A). Orthotopic Tyk-nu tumors expressing human CD19 enabled CD19 CAR T cells to serve as positive toxicity controls (Figure S11B). Mice were treated with untransduced T cells, CD19 1XX-CAR T cells, or uPAR 1XX-CAR T cells (Figure S11C), and CAR T cells were CRISPR-Cas9-edited at *TRAC* to prevent graft-vs-host disease (Figures S11D and S11E).[60] Both CD19 and uPAR CAR T cells exhibited potent cytotoxicity *in vitro* and eradicated $CD19^+$/uPAR+ tumors *in vivo*, achieving complete regression within 1–2 weeks and resistance to tumor rechallenge (Figures 6I, S11F, and S11G).

As expected, CD19 CAR T cells depleted the B cell compartment. By contrast, uPAR CAR T had no significant impact on monocytes, granulocytes, or neutrophils, despite uPAR expression on subsets of these populations (Figures 6J, 6K, and S11H–S11J; Data S1.8). In *ex vivo* co-cultures, normal uPAR+ monocytes were depleted by uPAR CAR T cells (Figures S11K and S11L), but if such targeting occurred *in vivo*, it was not sustained, hinting that these populations have the potential to rapidly regenerate. Supporting this possibility, analysis of human peripheral blood revealed that pro-monocytes—the precursors of circulating monocytes—express minimal uPAR (Figure S11M). Together, these findings indicate that uPAR CAR T cells maintain strong antitumor efficacy with a tolerable safety profile, providing a compelling rationale for clinical translation.

Senescence-inducing therapies enhance uPAR CAR T cell antitumor activity

Our initial interest in uPAR stemmed from its consistent induction in senescent cells, which accumulate in fibrotic organs and tumors, but also in tumors exposed to cytotoxic or targeted therapies.[25] Across multiple human tumor types, bulk RNA-seq of pre- and post-treatment samples, together with multi-IF and scRNA-seq restricted to the tumor compartment, revealed increased *PLAUR* expression following therapy or progression, coinciding with enrichment of EMT and senescence signatures (Figures 7A–7C, S12A, and S12B; Data S1.9A and S1.9B). Similarly, gene set enrichment analysis (GSEA) of matched HGSOC samples[61] before and after treatment with cisplatin (a DNA-crosslinking agent that triggers DNA damage response, leading to replication stress, apoptosis, or senescence)[62] showed *PLAUR* upregulation alongside senescence- and fibrosis-associated programs and loss of an E2F-driven proliferation signature (Figures 7D and S12C–S12E). Elevated *PLAUR* expression was also observed in colorectal, lung, PDAC, and ovarian tumor cells treated with cisplatin, ionizing radiation, or irinotecan and in publicly available RNA-seq datasets from 9 of 13 cancer types (including lung, liver, colon, and breast) treated with established senescence inducers such as etoposide or alisertib (Figures 7E and S12F).

We hypothesized that therapies inducing an injury- or senescent-like state, which increases uPAR levels and/or enriches for uPAR+ tumor cells, would improve the efficacy of uPAR CAR T cell therapy. To test this, we used our previously established murine MPB1 HGSOC model (see Figure 6), which responds to cisplatin treatment by engaging a senescence program[58] and also triggers uPAR upregulation as assessed by western blot, flow cytometry, and ^{89}Zr-based uPAR imaging (Figures 7F, 7G, and S12G–S12I). As expected, this increased antigen density was associated with greater *in vitro* cytotoxicity of uPAR CAR T cells following cisplatin treatment (Figure 7H; Data S1.9C).

Extending these findings *in vivo*, we treated mice bearing metastatic MPB1 tumors with cisplatin, uPAR CAR T cells, or both and monitored tumor responses by bioluminescence and survival. The combination produced superior outcomes: greater CAR T cell infiltration, improved tumor control, and prolonged survival compared with either agent alone, without added toxicity as assessed by body weight and temperature measurement, as well as blood counts 1-month post-treatment (Figures 7I–7L and S12J; Data S1.9D). Of note, 80% of mice receiving the combination remained tumor-free beyond 300 days, whereas all mice treated with cisplatin alone succumbed by day 55 (Figure 7K). Similar results were observed in an orthotopic $Kras^{G12D}$;$p53^{R172H}$ (KP) murine lung cancer model, where cisplatin plus uPAR CAR T cells outperformed either monotherapy without added toxicity (Figures S12K and S12L). These data indicate that senescence-inducing chemotherapy increases the prevalence of uPAR-positive tumor cells with high antigen density, thereby enhancing CAR T cell efficacy.

Together with our other results across multiple tumor types and models, these findings underscore the broad therapeutic potential of uPAR CAR T cells—as both monotherapy and in rational combinations—for solid tumor treatment.

(C) Representative H&E and immunohistochemistry staining for uPAR and WT1 in MYC^{OE}; $Trp53^{KO}$ (MP) tumors.
(D–F) Mice bearing autochthonous MP tumors were treated with 2×10^6 control untransduced T cells (UTD) or murine uPAR CAR T cells (m.uPAR-m.28z): (D) tumor weight at 2 weeks post-treatment (left) and overall survival (right), (E) body weight over time post treatment, and (F) complete blood counts (at day 40 post treatment).
(G) Schematic for testing CAR T cells in mice with a humanized immune system (see STAR Methods).
(H) Flow cytometry of bone marrow from humanized mice 6 weeks after HSPC transplantation and prior to tumor implantation (see STAR Methods).
(I) Effects of the indicated TRAC-edited CAR T cells in humanized mice bearing Tyk-nu^{CD19} xenografts: bioluminescence images (left), radiance quantification of tumor (middle), and overall survival (right).
(J) Flow cytometry showing relative abundance of human immune cell populations in bone marrow at tumor remission (day 7 post CAR T treatment) normalized to mouse CD45+ cells.
(K) uPAR expression in human granulocytes ($CD16+SSA^{high}$) and monocytes (CD14+) was assessed by flow cytometry using a human-specific uPAR antibody (gated as $hCD45^+CD19^-CD3^-$).
TRAC denotes TRAC-locus-edited CAR T cells. 1XX denotes CARs with inactivation of immunoreceptor tyrosine-based activation motifs 2 and 3 (ITAM2/3).[50]
UTD, untransduced T cells. Statistics: Student's *t* test (D and F), multiple *t* test (I, middle), log-rank test (D, right; I, right), and one-way ANOVA (J and K). Error bars indicate SD (D) or SEM (E and I–K).
See also Figures S10 and S11.

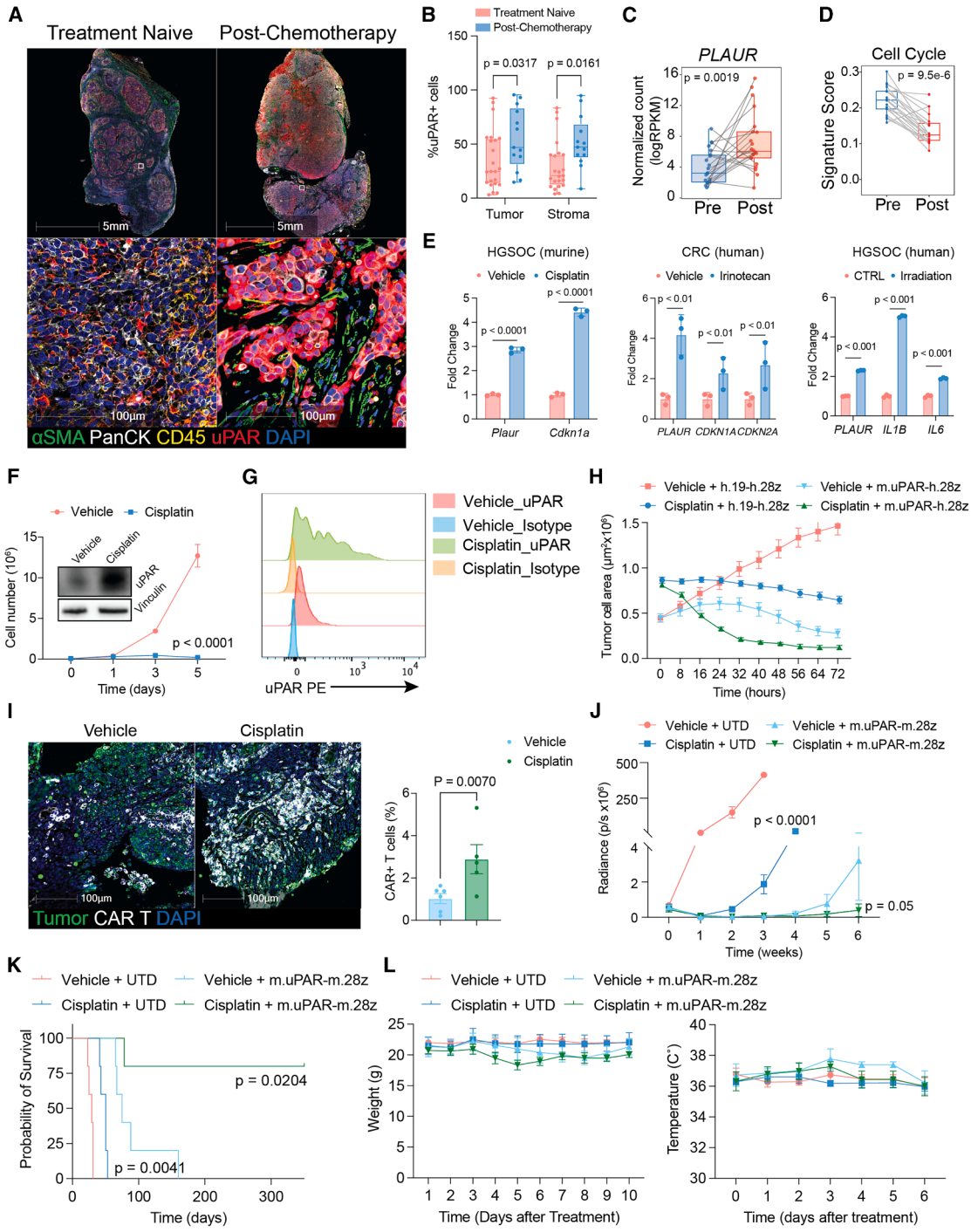

Figure 7. Therapy-induced senescence enhances CAR T cell efficacy

(A) Representative multi-IF images of HGSOC tumors from treatment-naive (n = 23) or post-chemotherapy (n = 13) patients.

(B) Quantification of uPAR+ cells among PanCK+ (tumor) or PanCK− (stromal) populations from (A) (each dot represents one tumor).

(C and D) Bulk RNA-seq analysis of matched pre- and post-cisplatin-treated ovarian cancer samples[61] showing *PLAUR* expression (C) and cell-cycle signature scores (D).

(E) qPCR analysis of the indicated genes in MPB1, 136p, and OVCAR8 cells after 72 h exposure to the indicated senescence-inducing treatments *in vitro*.

(F) Proliferation curves and immunoblotting showing uPAR upregulation in MPB1 cells 72 h after cisplatin (1 μM).

(G) Flow cytometry analysis of surface uPAR expression in MPB1 cells treated with vehicle or cisplatin (1 μM) for 72 h.

(legend continued on next page)

DISCUSSION

This study establishes uPAR as an actionable cancer target that marks an aggressive tumor-cell state and demonstrates the therapeutic potential of uPAR CAR T cells across solid tumors. Integrated genomic, transcriptomic, and spatial analyses show uPAR is broadly elevated across malignancies and associated with *TP53* and RAS/MAPK pathway mutations, as well as transcriptional programs linked to EMT, inflammation, and fibrosis. Consistent with functional data implicating uPAR in tumor maintenance and metastasis,[48,63] these findings distinguish uPAR from lineage-restricted targets, such as CD19, FOLR1, or PSMA. Unlike these targets, uPAR does not define a specific cell lineage but instead represents a marker of a conserved tumor-maintaining state. Accordingly, CAR T cells targeting the D2-D3 domain of uPAR display broad antitumor activity in xenograft, syngeneic, and patient-derived models, including in adjuvant and combination settings, supporting the concept that targeting conserved malignant cell states can enable therapeutic strategies that transcend tumor type.

A defining feature of uPAR-high tumors is that they are embedded within a pro-fibrotic, immunosuppressive niche enriched for uPAR-positive fibroblasts and myeloid cells that are also found in murine and human fibrotic tissues and exhibit senescence-associated transcriptional programs.[25,64] Spatial analyses show that these tissue regions are depleted of effector T cells and are enriched for programs reminiscent of pathological wound-healing responses.[65–68] Collectively, these data support a model in which uPAR marks not only malignant cells but also a conserved pathological tumor-stroma ecosystem that is associated with features consistent with immune exclusion and therapeutic resistance, distinguishing it from targets confined to the tumor-cell compartment.

Mechanistic insight from genetically engineered mouse models further supports this co-evolutionary framework. During KRAS-driven pancreatic neoplasia, a uPAR-expressing progenitor/EMT-like state expands alongside a uPAR-positive, senescence-enriched stromal niche.[39] Loss of p53 permits expansion of both compartments, driving fibrosis, immune evasion, and malignant progression. That uPAR-high tumors are enriched for similar tumor and stromal cell states suggests that a normally transient, p53-restrained, wound-healing response[69,70] becomes stabilized in advanced disease, providing a mechanistic explanation for the association between uPAR expression, *TP53* mutations, and aggressive clinical behavior. In this view, p53 functions not only as a guardian of genomic integrity but also as a guardian of cellular plasticity, restraining a dangerous cell state whose persistence promotes immune evasion, tissue remodeling, and cancer progression.

This conceptual framework highlights an unexpected therapeutic opportunity. Although *TP53* is mutated in most cancers and its activation can be curative in select hematologic malignancies, efforts to harness p53 biology in solid tumors have largely focused on restoring its biochemical activities, with longstanding debate over which downstream effector programs are most critical to engage for tumor suppression.[71] Our findings instead suggest that a central biological output of p53 is the elimination of a pathological cell state and its co-evolving niche.[39] By directly targeting uPAR-defined tumor and stromal compartments, uPAR-directed therapies may functionally recapitulate this tumor-suppressive function, thereby repressing the progenitor-like, niche-forming states that drive the most aggressive features of *TP53*-mutant disease. In this view, CAR T cells are not simply tumor-selective cytotoxic agents but can be effective tools to therapeutically constrain malignant plasticity.

These insights also address two central barriers to CAR T cell therapy in solid tumors: antigen heterogeneity and stromal exclusion.[5,6] Antigen heterogeneity may be less limiting for uPAR-directed therapy because uPAR marks a dynamic and tumor-maintaining cell state, helping explain the deep responses observed even in tumors with variable baseline expression. Moreover, antigen density can be further increased through rational "one-two punch" strategies,[72] in which cytotoxic or targeted therapies induce senescence-like programs[22,26,73–75] that elevate uPAR expression and sensitize residual disease to CAR T cell elimination. In parallel, uPAR expression on senescent-like fibroblasts and myeloid cells provides a means to dismantle the suppressive stromal niche. Consistent with this, our prior work shows that uPAR CAR T cells targeting senescent cells remodel fibrotic tissues,[25] and, as shown herein, this remodeling is associated with CAR T cell infiltration and cytotoxic activity. Similarly, parallel work demonstrates that uPAR CAR T cells exhibit potent efficacy in glioblastoma models and can co-target supportive stromal cells (see also Maich et al., in press). Together, these properties distinguish uPAR as a rare solid-tumor target less prone to issues of antigen heterogeneity and microenvironmental resistance.

Finally, uPAR-directed therapy appears to have a favorable therapeutic index. uPAR expression in vital tissues is limited relative to other clinical targets, and in both syngeneic and humanized models, uPAR CAR T cells achieved durable tumor clearance without sustained myeloid depletion or major toxicity. These observations are consistent with engagement of

(H) Incucyte-based viability analysis of proliferating (vehicle) or senescent (cisplatin; 1 μM) MPB1 cells co-cultured with control (h.19-h.28z) or murine uPAR CAR T cells (m.uPAR-h.28z).

(I) Multi-IF images (left) and quantification (right) of GFP+ MPB1 tumor cells (green) and m.uPAR-m.28z CAR T cells (white) 1 week after treatment of mice bearing metastatic MPB1 tumors (2×10^6 CAR T cells).

(J–L) Response of mice bearing MPB1^{luc} tumors treated with cisplatin (3 mg/kg), UTD T cells, m.uPAR-m.28z CAR T cells (2×10^6), or the combination. Tumor burden was monitored by bioluminescence (J), overall survival was shown by Kaplan-Meier plot (K), and body weight (L, left) and temperature (L, right) were assessed as an indicator of systemic toxicities.

Statistics: two-way ANOVA (B and E), Student's *t* test (C, D, F, and I), multiple *t* test (J), and log-rank test (K). Error bars indicate SD (B, E, F, and I) or SEM (H and J–L).

See also Figure S12.

emergency myelopoiesis, which rapidly regenerates myeloid populations in both mice and humans.[76] Such adaptations may be facilitated by negligible uPAR expression in monocyte precursors and could explain the rapid resolution of cytokine-release symptoms observed following high-dose uPAR CAR T cell administration.[25]

Beyond oncology, the association of uPAR with senescent and pro-fibrotic cell states suggests broader applications in chronic degenerative and inflammatory diseases.[25,27,30] Consistent with this potential, the clinical-grade uPAR binders described here support multiple therapeutic and diagnostic formats, including CAR T cells, antibody-drug conjugates, and PET imaging. Together, these findings define uPAR as a biologically grounded and clinically tractable entry point for therapies designed to eliminate pathological cell states their supportive niches, with implications that extend from solid tumors to a spectrum of fibrosis- and senescence-driven diseases.

Limitations of the study

Our human tissue and spatial analyses have several limitations. Tumor-cell quantification relied on the epithelial marker PanCK, which may underestimate tumor burden in cells undergoing a full EMT, and multiplex IF provides threshold-based classifications rather than absolute quantification of uPAR positivity, and the calculation of ~15% of tumors harboring high and relatively uniform uPAR expression is biased by the number and types of tumors analyzed. In addition, data linking uPAR-high tumors to genomic and transcriptional features were based on *PLAUR* mRNA expression and not tumor-specific protein expression. Spatial transcriptomics was limited to a single section per case, though high probe density enabled robust mapping of organized cell states and integration with scRNA-seq data across many patients. This was further complemented by a ~350-sample 20+-plex hyperplex IF cohort that identified recurrent spatial patterns across five cancer subtypes. Finally, senescence was inferred from published or in-house generated gene-expression signatures and markers such as p16. Accordingly, we refer to these populations as occupying a "senescent-like state" to acknowledge the incomplete definition of senescence *in vivo*.

Our preclinical studies combined syngeneic, cell line xenograft, PDX, and PDO models. These systems were used to demonstrate efficacy, safety, and dual targeting of uPAR-high tumor cells and their pro-fibrotic stroma but do not fully recapitulate the desmoplastic architecture or immune complexity of advanced human tumors. Species-specific uPAR scFvs enabled selective targeting of tumor and stromal cells but introduced cross-species differences in stromal cells and cell-cell signaling potential that undoubtedly differ from advanced human tumors. Future work incorporating multicellular *ex vivo* models or tumor slides may address this gap. While human-specific ELISA data from xenograft models indicate that circulating suPAR can derive from tumor cells, suPAR levels in cancer patients will include signals from chronic inflammation and fibrosis, limiting specificity, although pairing with uPAR PET imaging may improve interpretability. Our toxicity assessment is constrained by the lack of cross reactivity of human scFvs with murine uPAR, necessitating complementary studies using murine uPAR CAR T cells in syngenetic mouse models or human uPAR CAR T cells in mice with a humanized immune system that can only undergo short-term evaluation. Therefore, delayed toxicities cannot yet be excluded. The mechanisms underlying preservation of the myeloid compartment warrant further study.

RESOURCE AVAILABILITY

Lead contact

Further information and requests for resources and reagents should be directed to and will be fulfilled by the lead contact, Scott Lowe (lowes@mskcc.org).

Materials availability

The biological materials generated and/or analyzed during this study are available from the lead contact author (S.W.L.) on reasonable request.

Data and code availability

Bulk RNA-seq datasets include matched pre-post chemotherapy samples from HGSOC patients,[61] the Cancer SENESCopedia,[26] and vehicle- or cisplatin-treated MPB1 cancer cell lines.[58] Single-cell RNA-seq datasets include the MSK SPECTRUM HGSOC cohort[37]; the HTAN MSK colon cancer cohort[77]; NSCLC pre- and post-therapy samples[78]; and LUAD, PDAC, and liver cancer datasets. Accession numbers and repository information are provided in the STAR Methods. The 10× Genomics xenium spatial transcriptomics dataset generated in this study has been deposited in the NCBI Gene Expression Omnibus (GEO) under the accession number GEO: GSE293800. Due to their multi-terabyte size, hyperplex IF images cannot be easily deposited in a public repository and are available from the lead contact upon reasonable request. All custom code used for data processing, analysis, and figure generation in this study is publicly available. For previously published datasets, associated analysis code is available through the original studies' GitHub repositories.[77,78]

ACKNOWLEDGMENTS

We thank C.J. Sherr for insightful discussions; Mara Sherman for inputs and technical help for fibroblast biology; Ninghui Mao, Ning Fan, Besnik Qeriqi, Huiyong Zhao, Wenfei Kang, Afsar Barlas, and Xiaoping Chen for technical assistance; and Prasad Adusumilli for providing tissue samples. We thank Nayan Jain, Anton Dobrin, Zeguo Zhao, Margaret Kennedy, Andrea Chaikovsky, Caroline Broderick, Domhnall McHugh, Nalin Ratnayeke, and members of the Lowe and Sadelain laboratories for helpful discussions, as well as Janelle Simon for technical support and Janet Novak for manuscript editing. We thank Dr. Mark Carey for providing human low grade serous ovarian cancer cell lines VOA4627, VOA6406, and VOA7681. We thank C. Amor, J. Leibold, and J. Feucht for CAR T cell-related reagents and protocols. We thank C. Antonescu for providing sarcoma TMAs. This work was supported by the National Institute on Aging (5R01AG065396); the MSK Technology Development Fund and Experimental Therapeutics Center (FP00009954) (S.W.L. and M.S.); the Mark Foundation for Cancer Research Endeavor Award (S.W.L., P.B.R., D.P., and M.S.); the Pershing Square Sohn LOTUS Award (M.S.); Cycle for Survival; the Marie Josée and Henry Kravis Cancer Ecosystems Project; and by the NIH SPORE Soft Tissue Sarcoma P50 CA217694-06A1 and The Sarcoma Center at MSKCC (S.W.L.). Q.J. was supported by the MSK GMTEC Fellowship (#20422); A.C.W. by T32GM152349; J.R. and Z.Z. by Damon Runyon Cancer Research Foundation fellowships (DRG-2383-19 and DRG-2467-22) and HHMI; Z.Z. additionally by the American Federation for Aging Research and the Foundation for Women's Cancer (St. Louis Ovarian Cancer Awareness Research Grant); E.C.P. by F32CA268912 and K99CA276804; J.S.L. by R35CA232130; E.R. and E.C. by P30CA008748; J.F. by ERC Starting Grant 949667; and A.F. by the NIH SPORE in Soft Tissue Sarcoma P50 CA217694-06A1 and The Sarcoma Center at MSKCC. S.W.L. is the Geoffrey Beene Chair of Cancer Biology and an investigator of the Howard Hughes Medical Institute. We thank the Memorial Sloan Kettering Flow Cytometry, Molecular Cytology, Biobank and Tissue Division, Animal Facility, Antitumor

Assessment, Laboratory for Comparative Pathology, Bioinformatics, and Integrated Genomics Operation Cores for support. Schematics in the graphical abstract and Figures 3, 4, and 6 were created with BioRender.com.

AUTHOR CONTRIBUTIONS

Z.Z., S.V.P., C.A., M.S., and S.W.L. conceived the study. Z.Z., A.F., and S.W.L. designed experiments. Z.Z., S.T., and A.F. performed multiplex and hyperplex IF. E.R., E.C., S.T., and A.F. conducted spatial image analysis, with A.F. supervising and providing resources. Z.Z. and J.M.-S. designed h.uPAR CARs. Z.Z., X.F., V.W.Y., and W.L. generated CAR T cells. Y.-J.H. performed bulk bioinformatics. I.V.-G. and S.F. analyzed scRNA-seq data from the MSK-SPECTRUM HGSOC cohort. Q.J. analyzed MSK-CRC scRNA-seq data. Z.Z., X.F., S.H., and F.K. conducted humanized mouse studies. E.C.P. performed uPAR PET imaging, epitope mapping, and uptake assays. Z.Z., M.L., and M.K. performed toxicity studies. E.O. conducted spatial transcriptomics under J.R.'s supervision. Z.Z., X.F., M.L., W.L., K.C., and A.K. performed animal experiments. All authors contributed critical reagents and patient specimens. Z.Z. and S.W.L. wrote the manuscript, and Z.Z., J.R., E.O., A.F., M.S., and S.W.L. edited it.

DECLARATION OF INTERESTS

M.S.K. has filed patent applications 17/426728, 18/535012, and 18/534969 covering human uPAR binders and their applications (inventors: Z.Z., C.A., M.S., and S.W.L.). J.F. is an inventor on patents for senolytic uPAR CAR (WO2020160518A1) and 1XX CAR (WO2019133969A2). D.Z. reports institutional grants from Merck, Genentech, AstraZeneca, Xencor, Zymeworks, and Synthekine; personal fees from AstraZeneca, Xencor, Memgen, Daiichi Sankyo, Gilead, Synthekine, Immunos, Hervolution, Accurius, Replimune, and Calidi Biotherapeutics; and patent ownership related to oncolytic Newcastle disease virus therapy. S.W.L. is a founder and scientific advisory board member of Blueprint Medicines, Mirimus, Inc., ORIC Pharmaceuticals, and Faeth Therapeutics and serves on the scientific advisory board of PMV Pharmaceuticals. S.D.L. serves on the scientific advisory boards of Nybo Therapeutics and Episteme Prognostics.

STAR★METHODS

Detailed methods are provided in the online version of this paper and include the following:

SUPPLEMENTAL INFORMATION

Supplemental information can be found online at https://doi.org/10.1016/j.cell.2026.03.002.

Received: August 19, 2025
Revised: December 3, 2025
Accepted: March 2, 2026
Published: March 30, 2026

REFERENCES

1. Brentjens, R.J., Davila, M.L., Riviere, I., Park, J., Wang, X., Cowell, L.G., Bartido, S., Stefanski, J., Taylor, C., Olszewska, M., et al. (2013). CD19-targeted T cells rapidly induce molecular remissions in adults with chemotherapy-refractory acute lymphoblastic leukemia. Sci. Transl. Med. *5*, 177ra38. https://doi.org/10.1126/scitranslmed.3005930.
2. June, C.H., and Sadelain, M. (2018). Chimeric Antigen Receptor Therapy. N. Engl. J. Med. *379*, 64–73. https://doi.org/10.1056/NEJMra1706169.
3. Mackensen, A., Müller, F., Mougiakakos, D., Böltz, S., Wilhelm, A., Aigner, M., Völkl, S., Simon, D., Kleyer, A., Munoz, L., et al. (2022). Anti-CD19 CAR T cell therapy for refractory systemic lupus erythematosus. Nat. Med. *28*, 2124–2132. https://doi.org/10.1038/s41591-022-02017-5.
4. Wang, X., Wu, X., Tan, B., Zhu, L., Zhang, Y., Lin, L., Xiao, Y., Sun, A., Wan, X., Liu, S., et al. (2024). Allogeneic CD19-targeted CAR-T therapy in patients with severe myositis and systemic sclerosis. Cell *187*, 4890–4904. https://doi.org/10.1016/j.cell.2024.06.027.
5. Albelda, S.M. (2024). CAR T cell therapy for patients with solid tumours: key lessons to learn and unlearn. Nat. Rev. Clin. Oncol. *21*, 47–66. https://doi.org/10.1038/s41571-023-00832-4.
6. Guzman, G., Reed, M.R., Bielamowicz, K., Koss, B., and Rodriguez, A. (2023). CAR-T Therapies in Solid Tumors: Opportunities and Challenges. Curr. Oncol. Rep. *25*, 479–489. https://doi.org/10.1007/s11912-023-01380-x.
7. Khan, S.H., Choi, Y., Veena, M., Lee, J.K., and Shin, D.S. (2024). Advances in CAR T cell therapy: antigen selection, modifications, and current trials for solid tumors. Front. Immunol. *15*, 1489827. https://doi.org/10.3389/fimmu.2024.1489827.
8. Blasi, F., and Carmeliet, P. (2002). uPAR: a versatile signalling orchestrator. Nat. Rev. Mol. Cell Biol. *3*, 932–943. https://doi.org/10.1038/nrm977.
9. Smith, H.W., and Marshall, C.J. (2010). Regulation of cell signalling by uPAR. Nat. Rev. Mol. Cell Biol. *11*, 23–36. https://doi.org/10.1038/nrm2821.
10. Eefsen, R.L., Christensen, I.J., Johansen, A.Z., Chen, I.M., Calatayud, D., Pfeiffer, P., Andersen, F., Johansen, J.S., and Høyer-Hansen, G. (2025). Elevated levels of cleaved soluble forms of urokinase-type plasminogen activator receptor are associated with poor survival in advanced pancreatic cancer. Eur. J. Cancer *231*, 116095. https://doi.org/10.1016/j.ejca.2025.116095.
11. Zhai, B.T., Tian, H., Sun, J., Zou, J.B., Zhang, X.F., Cheng, J.X., Shi, Y.J., Fan, Y., and Guo, D.Y. (2022). Urokinase-type plasminogen activator receptor (uPAR) as a therapeutic target in cancer. J. Transl. Med. *20*, 135. https://doi.org/10.1186/s12967-022-03329-3.

12. Metrangolo, V., Ploug, M., and Engelholm, L.H. (2021). The Urokinase Receptor (uPAR) as a "Trojan Horse". Cancers (Basel) *13*, 5376. https://doi.org/10.3390/cancers13215376.

13. Blomberg, K., Hansen, T.F., Brasen, C.L., Madsen, J.B., Jensen, L.H., and Thomsen, C.B. (2021). The Soluble Urokinase-Type Plasminogen Activator Receptor as a Biomarker for Survival and Early Treatment Effect in Metastatic Colorectal Cancer. Cancers (Basel) *13*, 5100. https://doi.org/10.3390/cancers13205100.

14. Langkilde, A., Hansen, T.W., Ladelund, S., Linneberg, A., Andersen, O., Haugaard, S.B., Jeppesen, J., and Eugen-Olsen, J. (2011). Increased plasma soluble uPAR level is a risk marker of respiratory cancer in initially cancer-free individuals. Cancer Epidemiol. Biomarkers Prev. *20*, 609–618. https://doi.org/10.1158/1055-9965.EPI-10-1009.

15. Xing, R.H., and Rabbani, S.A. (1996). Overexpression of urokinase receptor in breast cancer cells results in increased tumor invasion, growth and metastasis. Int. J. Cancer *67*, 423–429. https://doi.org/10.1002/(SICI)1097-0215(19960729)67:3<423::AID-IJC18>3.0.CO;2-8.

16. Crowley, C.W., Cohen, R.L., Lucas, B.K., Liu, G., Shuman, M.A., and Levinson, A.D. (1993). Prevention of metastasis by inhibition of the urokinase receptor. Proc. Natl. Acad. Sci. USA *90*, 5021–5025. https://doi.org/10.1073/pnas.90.11.5021.

17. Mauro, C.D., Pesapane, A., Formisano, L., Rosa, R., D'Amato, V., Ciciola, P., Servetto, A., Marciano, R., Orsini, R.C., Monteleone, F., et al. (2017). Urokinase-type plasminogen activator receptor (uPAR) expression enhances invasion and metastasis in RAS mutated tumors. Sci. Rep. *7*, 9388. https://doi.org/10.1038/s41598-017-10062-1.

18. Jo, M., Takimoto, S., Montel, V., and Gonias, S.L. (2009). The urokinase receptor promotes cancer metastasis independently of urokinase-type plasminogen activator in mice. Am. J. Pathol. *175*, 190–200. https://doi.org/10.2353/ajpath.2009.081053.

19. Kanno, Y. (2023). The uPA/uPAR System Orchestrates the Inflammatory Response, Vascular Homeostasis, and Immune System in Fibrosis Progression. Int. J. Mol. Sci. *24*, 1796. https://doi.org/10.3390/ijms24021796.

20. Hamada, M., Varkoly, K.S., Riyadh, O., Beladi, R., Munuswamy-Ramanujam, G., Rawls, A., Wilson-Rawls, J., Chen, H., McFadden, G., and Lucas, A.R. (2024). Urokinase-Type Plasminogen Activator Receptor (uPAR) in Inflammation and Disease: A Unique Inflammatory Pathway Activator. Biomedicines *12*, 1167. https://doi.org/10.3390/biomedicines12061167.

21. Skorecki, K.L., and Freedman, B.I. (2015). A suPAR Biomarker for Chronic Kidney Disease. N. Engl. J. Med. *373*, 1971–1972. https://doi.org/10.1056/NEJMe1512997.

22. Schmitt, C.A., Wang, B., and Demaria, M. (2022). Senescence and cancer - role and therapeutic opportunities. Nat. Rev. Clin. Oncol. *19*, 619–636. https://doi.org/10.1038/s41571-022-00668-4.

23. Gorgoulis, V., Adams, P.D., Alimonti, A., Bennett, D.C., Bischof, O., Bishop, C., Campisi, J., Collado, M., Evangelou, K., Ferbeyre, G., et al. (2019). Cellular Senescence: Defining a Path Forward. Cell *179*, 813–827. https://doi.org/10.1016/j.cell.2019.10.005.

24. Serrano, M., Lin, A.W., McCurrach, M.E., Beach, D., and Lowe, S.W. (1997). Oncogenic ras provokes premature cell senescence associated with accumulation of p53 and p16INK4a. Cell *88*, 593–602. https://doi.org/10.1016/s0092-8674(00)81902-9.

25. Amor, C., Feucht, J., Leibold, J., Ho, Y.J., Zhu, C., Alonso-Curbelo, D., Mansilla-Soto, J., Boyer, J.A., Li, X., Giavridis, T., et al. (2020). Senolytic CAR T cells reverse senescence-associated pathologies. Nature *583*, 127–132. https://doi.org/10.1038/s41586-020-2403-9.

26. Jochems, F., Thijssen, B., De Conti, G., Jansen, R., Pogacar, Z., Groot, K., Wang, L., Schepers, A., Wang, C., Jin, H., et al. (2021). The Cancer SENESCopedia: A delineation of cancer cell senescence. Cell Rep. *36*, 109441. https://doi.org/10.1016/j.celrep.2021.109441.

27. Eskiocak, O., Gewolb, J., Shah, V., Rouse, J.A., Chowdhury, S., Akyildiz, E.O., Fernández-Maestre, I., Boyer, J.A., Filliol, A., Harris, A.S., et al. (2026). Anti-uPAR CAR T cells reverse and prevent aging-associated defects in intestinal regeneration and fitness. Nat Aging *6*, 108–126. https://doi.org/10.1038/s43587-025-01022-w.

28. Zhang, Z., Ma, B., Li, B., Li, Z., Gao, M., Zhao, H., Peng, R., Hu, J., Wang, Y., You, W., et al. (2025). Cardiolipin-mimic lipid nanoparticles without antibody modification delivered senolytic in vivo CAR-T therapy for inflamm-aging. Cell Rep. Med. *6*, 102209. https://doi.org/10.1016/j.xcrm.2025.102209.

29. Ming, X., Yang, Z., Huang, Y., Wang, Z., Zhang, Q., Lu, C., Sun, Y., Chen, Y., Zhang, L., Wu, J., et al. (2025). A chimeric peptide promotes immune surveillance of senescent cells in injury, fibrosis, tumorigenesis and aging. Nat Aging *5*, 28–47. https://doi.org/10.1038/s43587-024-00750-9.

30. Amor, C., Fernández-Maestre, I., Chowdhury, S., Ho, Y.J., Nadella, S., Graham, C., Carrasco, S.E., Nnuji-John, E., Feucht, J., Hinterleitner, C., et al. (2024). Prophylactic and long-lasting efficacy of senolytic CAR T cells against age-related metabolic dysfunction. Nat Aging *4*, 336–349. https://doi.org/10.1038/s43587-023-00560-5.

31. Zehir, A., Benayed, R., Shah, R.H., Syed, A., Middha, S., Kim, H.R., Srinivasan, P., Gao, J., Chakravarty, D., Devlin, S.M., et al. (2017). Mutational landscape of metastatic cancer revealed from prospective clinical sequencing of 10,000 patients. Nat. Med. *23*, 703–713. https://doi.org/10.1038/nm.4333.

32. Chan, J.E., Pan, C.H., Rub, J., Guzman, G., Krause, K., Brown, E., Zhang, Z., Styers, H., Hartmann, G., Li, Z., et al. (2026). Critical role for a high-plasticity cell state in lung cancer. Nature. https://doi.org/10.1038/s41586-025-09985-x.

33. Grivennikov, S.I., Greten, F.R., and Karin, M. (2010). Immunity, inflammation, and cancer. Cell *140*, 883–899. https://doi.org/10.1016/j.cell.2010.01.025.

34. MacCarthy-Morrogh, L., and Martin, P. (2020). The hallmarks of cancer are also the hallmarks of wound healing. Sci. Signal. *13*, eaay8690. https://doi.org/10.1126/scisignal.aay8690.

35. Xiang, H., Pan, Y., Sze, M.A., Wlodarska, M., Li, L., van de Mark, K.A., Qamar, H., Moure, C.J., Linn, D.E., Hai, J., et al. (2024). Single-Cell Analysis Identifies Notch3-Mediated Interactions between Stromal Cells That Promote Microenvironment Remodeling and Invasion in Lung Adenocarcinoma. Cancer Res. *84*, 1410–1425. https://doi.org/10.1158/0008-5472.CAN-23-1183.

36. Xue, R., Zhang, Q., Cao, Q., Kong, R., Xiang, X., Liu, H., Feng, M., Wang, F., Cheng, J., Li, Z., et al. (2022). Liver tumour immune microenvironment subtypes and neutrophil heterogeneity. Nature *612*, 141–147. https://doi.org/10.1038/s41586-022-05400-x.

37. Vázquez-García, I., Uhlitz, F., Ceglia, N., Lim, J.L.P., Wu, M., Mohibullah, N., Niyazov, J., Ruiz, A.E.B., Boehm, K.M., Bojilova, V., et al. (2022). Ovarian cancer mutational processes drive site-specific immune evasion. Nature *612*, 778–786. https://doi.org/10.1038/s41586-022-05496-1.

38. Steele, N.G., Carpenter, E.S., Kemp, S.B., Sirihorachai, V.R., The, S., Delrosario, L., Lazarus, J., Amir, E.D., Gunchick, V., Espinoza, C., et al. (2020). Multimodal Mapping of the Tumor and Peripheral Blood Immune Landscape in Human Pancreatic Cancer. Nat. Cancer *1*, 1097–1112. https://doi.org/10.1038/s43018-020-00121-4.

39. Reyes, J., Del Priore, I., Chaikovsky, A.C., Pasnuri, N., Elhossiny, A.M., Krause, T., Moorman, A., Snopkowski, C., Takizawa, M., Burdziak, C., et al. (2025). Oncogenic and tumor-suppressive forces converge on a progenitor niche at the benign-to-malignant transition. Cell *189*. https://doi.org/10.1016/j.cell.2026.03.032.

40. Williams, H.L., Dias Costa, A., Zhang, J., Raghavan, S., Winter, P.S., Kapner, K.S., Ginebaugh, S.P., Väyrynen, S.A., Väyrynen, J.P., Yuan, C., et al. (2023). Spatially Resolved Single-Cell Assessment of Pancreatic Cancer Expression Subtypes Reveals Co-expressor Phenotypes and Extensive Intratumoral Heterogeneity. Cancer Res. *83*, 441–455. https://doi.org/10.1158/0008-5472.CAN-22-3050.

41. Grünwald, B.T., Devisme, A., Andrieux, G., Vyas, F., Aliar, K., McCloskey, C.W., Macklin, A., Jang, G.H., Denroche, R., Romero, J.M., et al. (2021).

Spatially confined sub-tumor microenvironments in pancreatic cancer. Cell *184*, 5577–5592. https://doi.org/10.1016/j.cell.2021.09.022.

42. Espinosa-Carrasco, G., Chiu, E., Scrivo, A., Zumbo, P., Dave, A., Betel, D., Kang, S.W., Jang, H.J., Hellmann, M.D., Burt, B.M., et al. (2024). Intratumoral immune triads are required for immunotherapy-mediated elimination of solid tumors. Cancer Cell *42*, 1202–1216. https://doi.org/10.1016/j.ccell.2024.05.025.

43. Grout, J.A., Sirven, P., Leader, A.M., Maskey, S., Hector, E., Puisieux, I., Steffan, F., Cheng, E., Tung, N., Maurin, M., et al. (2022). Spatial Positioning and Matrix Programs of Cancer-Associated Fibroblasts Promote T-cell Exclusion in Human Lung Tumors. Cancer Discov. *12*, 2606–2625. https://doi.org/10.1158/2159-8290.CD-21-1714.

44. Feig, C., Jones, J.O., Kraman, M., Wells, R.J.B., Deonarine, A., Chan, D.S., Connell, C.M., Roberts, E.W., Zhao, Q., Caballero, O.L., et al. (2013). Targeting CXCL12 from FAP-expressing carcinoma-associated fibroblasts synergizes with anti-PD-L1 immunotherapy in pancreatic cancer. Proc. Natl. Acad. Sci. USA *110*, 20212–20217. https://doi.org/10.1073/pnas.1320318110.

45. Ma, R.Y., Black, A., and Qian, B.Z. (2022). Macrophage diversity in cancer revisited in the era of single-cell omics. Trends Immunol. *43*, 546–563. https://doi.org/10.1016/j.it.2022.04.008.

46. Singh, N., Lee, Y.G., Shestova, O., Ravikumar, P., Hayer, K.E., Hong, S.J., Lu, X.M., Pajarillo, R., Agarwal, S., Kuramitsu, S., et al. (2020). Impaired Death Receptor Signaling in Leukemia Causes Antigen-Independent Resistance by Inducing CAR T-cell Dysfunction. Cancer Discov. *10*, 552–567. https://doi.org/10.1158/2159-8290.CD-19-0813.

47. Dufva, O., Koski, J., Maliniemi, P., Ianevski, A., Klievink, J., Leitner, J., Pölönen, P., Hohtari, H., Saeed, K., Hannunen, T., et al. (2020). Integrated drug profiling and CRISPR screening identify essential pathways for CAR T-cell cytotoxicity. Blood *135*, 597–609. https://doi.org/10.1182/blood.2019002121.

48. Mollaoglu, G., Tepper, A., Falcomatà, C., Potak, H.T., Pia, L., Amabile, A., Mateus-Tique, J., Rabinovich, N., Park, M.D., LaMarche, N.M., et al. (2024). Ovarian cancer-derived IL-4 promotes immunotherapy resistance. Cell *187*, 7492–7510. https://doi.org/10.1016/j.cell.2024.10.006.

49. Park, J.H., Palomba, M.L., Perica, K., Devlin, S.M., Shah, G., Dahi, P.B., Lin, R.J., Salles, G., Scordo, M., Nath, K., et al. (2025). Results From First-in-Human Phase I Study of a Novel CD19-1XX Chimeric Antigen Receptor With Calibrated Signaling in Large B-Cell Lymphoma. J. Clin. Oncol. *43*, 2418–2428. https://doi.org/10.1200/JCO-24-02424.

50. Feucht, J., Sun, J., Eyquem, J., Ho, Y.J., Zhao, Z., Leibold, J., Dobrin, A., Cabriolu, A., Hamieh, M., and Sadelain, M. (2019). Calibration of CAR activation potential directs alternative T cell fates and therapeutic potency. Nat. Med. *25*, 82–88. https://doi.org/10.1038/s41591-018-0290-5.

51. Kandalaft, L.E., Dangaj Laniti, D., and Coukos, G. (2022). Immunobiology of high-grade serous ovarian cancer: lessons for clinical translation. Nat. Rev. Cancer *22*, 640–656. https://doi.org/10.1038/s41568-022-00503-z.

52. Tuna, M., Ju, Z., Yoshihara, K., Amos, C.I., Tanyi, J.L., and Mills, G.B. (2020). Clinical relevance of TP53 hotspot mutations in high-grade serous ovarian cancers. Br. J. Cancer *122*, 405–412. https://doi.org/10.1038/s41416-019-0654-8.

53. Nguyen, B., Fong, C., Luthra, A., Smith, S.A., DiNatale, R.G., Nandakumar, S., Walch, H., Chatila, W.K., Madupuri, R., Kundra, R., et al. (2022). Genomic characterization of metastatic patterns from prospective clinical sequencing of 25,000 patients. Cell *185*, 563–575. https://doi.org/10.1016/j.cell.2022.01.003.

54. Bayraktar, E., Chen, S., Corvigno, S., Liu, J., and Sood, A.K. (2024). Ovarian cancer metastasis: Looking beyond the surface. Cancer Cell *42*, 1631–1636. https://doi.org/10.1016/j.ccell.2024.08.016.

55. Rasmussen, L.J.H., Petersen, J.E.V., and Eugen-Olsen, J. (2021). Soluble Urokinase Plasminogen Activator Receptor (suPAR) as a Biomarker of Systemic Chronic Inflammation. Front. Immunol. *12*, 780641. https://doi.org/10.3389/fimmu.2021.780641.

56. Hayek, S.S., Leaf, D.E., Samman Tahhan, A., Raad, M., Sharma, S., Waikar, S.S., Sever, S., Camacho, A., Wang, X., Dande, R.R., et al. (2020). Soluble Urokinase Receptor and Acute Kidney Injury. N. Engl. J. Med. *382*, 416–426. https://doi.org/10.1056/NEJMoa1911481.

57. Dang Cao, T.L., Kawanishi, K., Hashimoto, S., Hengphasatporn, K., Nagai-Okatani, C., Kimura, T., Abdelaziz, M., Shiratani, R., Poullikkas, T., Azmi, N.U., et al. (2025). Tumor-expressed GPNMB orchestrates Siglec-9+ TAM polarization and EMT to promote metastasis in triple-negative breast cancer. Proc. Natl. Acad. Sci. USA *122*, e2503081122. https://doi.org/10.1073/pnas.2503081122.

58. Paffenholz, S.V., Salvagno, C., Ho, Y.J., Limjoco, M., Baslan, T., Tian, S., Kulick, A., de Stanchina, E., Wilkinson, J.E., Barriga, F.M., et al. (2022). Senescence induction dictates response to chemo- and immunotherapy in preclinical models of ovarian cancer. Proc. Natl. Acad. Sci. USA *119*, e2117754119. https://doi.org/10.1073/pnas.2117754119.

59. Haubner, S., Mansilla-Soto, J., Nataraj, S., Kogel, F., Chang, Q., de Stanchina, E., Lopez, M., Ng, M.R., Fraser, K., Subklewe, M., et al. (2023). Cooperative CAR targeting to selectively eliminate AML and minimize escape. Cancer Cell *41*, 1871–1891. https://doi.org/10.1016/j.ccell.2023.09.010.

60. Eyquem, J., Mansilla-Soto, J., Giavridis, T., van der Stegen, S.J.C., Hamieh, M., Cunanan, K.M., Odak, A., Gönen, M., and Sadelain, M. (2017). Targeting a CAR to the TRAC locus with CRISPR/Cas9 enhances tumour rejection. Nature *543*, 113–117. https://doi.org/10.1038/nature21405.

61. Javellana, M., Eckert, M.A., Heide, J., Zawieracz, K., Weigert, M., Ashley, S., Stock, E., Chapel, D., Huang, L., Yamada, S.D., et al. (2022). Neoadjuvant Chemotherapy Induces Genomic and Transcriptomic Changes in Ovarian Cancer. Cancer Res. *82*, 169–176. https://doi.org/10.1158/0008-5472.CAN-21-1467.

62. Dasari, S., and Tchounwou, P.B. (2014). Cisplatin in cancer therapy: molecular mechanisms of action. Eur. J. Pharmacol. *740*, 364–378. https://doi.org/10.1016/j.ejphar.2014.07.025.

63. Chan, J.E., Pan, C.H., Rub, J., Guzman, G., Krause, K., Brown, E., Zhang, Z., Styers, H., Hartmann, G., Li, Z., et al. (2026). Functional interrogation uncovers a critical role for a high-plasticity cell state in lung adenocarcinoma. Nature *651*, 231–241. Preprint at bioRxiv 2025. https://doi.org/10.1038/s41586-025-09985-x.

64. O'Reilly, S., Tsou, P.S., and Varga, J. (2024). Senescence and tissue fibrosis: opportunities for therapeutic targeting. Trends Mol. Med. *30*, 1113–1125. https://doi.org/10.1016/j.molmed.2024.05.012.

65. Ye, J., Baer, J.M., Faget, D.V., Morikis, V.A., Ren, Q., Melam, A., Delgado, A.P., Luo, X., Bagchi, S.M., Belle, J.I., et al. (2024). Senescent CAFs Mediate Immunosuppression and Drive Breast Cancer Progression. Cancer Discov. *14*, 1302–1323. https://doi.org/10.1158/2159-8290.CD-23-0426.

66. Belle, J.I., Sen, D., Baer, J.M., Liu, X., Lander, V.E., Ye, J., Sells, B.E., Knolhoff, B.L., Faiz, A., Kang, L.I., et al. (2024). Senescence Defines a Distinct Subset of Myofibroblasts That Orchestrates Immunosuppression in Pancreatic Cancer. Cancer Discov. *14*, 1324–1355. https://doi.org/10.1158/2159-8290.CD-23-0428.

67. Liu, Y., Xun, Z., Ma, K., Liang, S., Li, X., Zhou, S., Sun, L., Liu, Y., Du, Y., Guo, X., et al. (2023). Identification of a tumour immune barrier in the HCC microenvironment that determines the efficacy of immunotherapy. J. Hepatol. *78*, 770–782. https://doi.org/10.1016/j.jhep.2023.01.011.

68. Qi, J., Sun, H., Zhang, Y., Wang, Z., Xun, Z., Li, Z., Ding, X., Bao, R., Hong, L., Jia, W., et al. (2022). Single-cell and spatial analysis reveal interaction of FAP+ fibroblasts and SPP1+ macrophages in colorectal cancer. Nat. Commun. *13*, 1742. https://doi.org/10.1038/s41467-022-29366-6.

69. Kozyrska, K., Pilia, G., Vishwakarma, M., Wagstaff, L., Goschorska, M., Cirillo, S., Mohamad, S., Gallacher, K., Carazo Salas, R.E., and Piddini, E. (2022). p53 directs leader cell behavior, migration, and clearance during epithelial repair. Science *375*, eabl8876. https://doi.org/10.1126/science.abl8876.

70. Antoniades, H.N., Galanopoulos, T., Neville-Golden, J., Kiritsy, C.P., and Lynch, S.E. (1994). p53 expression during normal tissue regeneration in response to acute cutaneous injury in swine. J. Clin. Investig. *93*, 2206–2214. https://doi.org/10.1172/JCI117217.

71. Kastenhuber, E.R., and Lowe, S.W. (2017). Putting p53 in context. Cell *170*, 1062–1078. https://doi.org/10.1016/j.cell.2017.08.028.

72. Wang, L., Lankhorst, L., and Bernards, R. (2022). Exploiting senescence for the treatment of cancer. Nat. Rev. Cancer *22*, 340–355. https://doi.org/10.1038/s41568-022-00450-9.

73. Prasanna, P.G., Citrin, D.E., Hildesheim, J., Ahmed, M.M., Venkatachalam, S., Riscuta, G., Xi, D., Zheng, G., Deursen, J.V., Goronzy, J., et al. (2021). Therapy-Induced Senescence: Opportunities to Improve Anticancer Therapy. J. Natl. Cancer Inst. *113*, 1285–1298. https://doi.org/10.1093/jnci/djab064.

74. Ruscetti, M., Leibold, J., Bott, M.J., Fennell, M., Kulick, A., Salgado, N.R., Chen, C.C., Ho, Y.J., Sanchez-Rivera, F.J., Feucht, J., et al. (2018). NK cell-mediated cytotoxicity contributes to tumor control by a cytostatic drug combination. Science *362*, 1416–1422. https://doi.org/10.1126/science.aas9090.

75. Schmitt, C.A., Fridman, J.S., Yang, M., Lee, S., Baranov, E., Hoffman, R.M., and Lowe, S.W. (2002). A senescence program controlled by p53 and p16INK4a contributes to the outcome of cancer therapy. Cell *109*, 335–346. https://doi.org/10.1016/s0092-8674(02)00734-1.

76. Swann, J.W., Olson, O.C., and Passegué, E. (2024). Made to order: emergency myelopoiesis and demand-adapted innate immune cell production. Nat. Rev. Immunol. *24*, 596–613. https://doi.org/10.1038/s41577-024-00998-7.

77. Moorman, A., Benitez, E.K., Cambulli, F., Jiang, Q., Mahmoud, A., Lumish, M., Hartner, S., Balkaran, S., Bermeo, J., Asawa, S., et al. (2025). Progressive plasticity during colorectal cancer metastasis. Nature *637*, 947–954. https://doi.org/10.1038/s41586-024-08150-0.

78. Maynard, A., McCoach, C.E., Rotow, J.K., Harris, L., Haderk, F., Kerr, D.L., Yu, E.A., Schenk, E.L., Tan, W., Zee, A., et al. (2020). Therapy-Induced Evolution of Human Lung Cancer Revealed by Single-Cell RNA Sequencing. Cell *182*, 1232–1251. https://doi.org/10.1016/j.cell.2020.07.017.

79. Love, M.I., Huber, W., and Anders, S. (2014). Moderated estimation of fold change and dispersion for RNA-seq data with DESeq2. Genome Biol. *15*, 550. https://doi.org/10.1186/s13059-014-0550-8.

80. Hao, Y., Stuart, T., Kowalski, M.H., Choudhary, S., Hoffman, P., Hartman, A., Srivastava, A., Molla, G., Madad, S., Fernandez-Granda, C., et al. (2024). Dictionary learning for integrative, multimodal and scalable single-cell analysis. Nat. Biotechnol. *42*, 293–304. https://doi.org/10.1038/s41587-023-01767-y.

81. McGinnis, C.S., Murrow, L.M., and Gartner, Z.J. (2019). DoubletFinder: Doublet Detection in Single-Cell RNA Sequencing Data Using Artificial Nearest Neighbors. Cell Syst. *8*, 329–337.e324. https://doi.org/10.1016/j.cels.2019.03.003.

82. Dobin, A., Davis, C.A., Schlesinger, F., Drenkow, J., Zaleski, C., Jha, S., Batut, P., Chaisson, M., and Gingeras, T.R. (2013). STAR: ultrafast universal RNA-seq aligner. Bioinformatics *29*, 15–21. https://doi.org/10.1093/bioinformatics/bts635.

83. Liao, Y., Smyth, G.K., and Shi, W. (2014). featureCounts: an efficient general purpose program for assigning sequence reads to genomic features. Bioinformatics *30*, 923–930. https://doi.org/10.1093/bioinformatics/btt656.

84. Wickham, H., François, R., Henry, L., Müller, K., and Vaughan, D. (2026). dplyr: A Grammar of Data Manipulation. R package version 1.2.0. https://dplyr.tidyverse.org.

85. Subramanian, A., Tamayo, P., Mootha, V.K., Mukherjee, S., Ebert, B.L., Gillette, M.A., Paulovich, A., Pomeroy, S.L., Golub, T.R., Lander, E.S., and Mesirov, J.P. (2005). Gene set enrichment analysis: a knowledge-based approach for interpreting genome-wide expression profiles. Proc. Natl. Acad. Sci. USA *102*, 15545–15550. https://doi.org/10.1073/pnas.0506580102.

86. Pratt, E.C., Mezzadra, R., Kulick, A., Kaminsky, S., Samuels, Z.V., Loor, A., de Stanchina, E., Lowe, S.W., and Lewis, J.S. (2024). uPAR Immuno-PET in Pancreatic Cancer, Aging, and Chemotherapy-Induced Senescence. J. Nucl. Med. *65*, 1718–1723. https://doi.org/10.2967/jnumed.124.268278.

87. Sharma, S.K., Lyashchenko, S.K., Park, H.A., Pillarsetty, N., Roux, Y., Wu, J., Poty, S., Tully, K.M., Poirier, J.T., and Lewis, J.S. (2019). A rapid bead-based radioligand binding assay for the determination of target-binding fraction and quality control of radiopharmaceuticals. Nucl. Med. Biol. *71*, 32–38. https://doi.org/10.1016/j.nucmedbio.2019.04.005.

88. Kuhn, N.F., Purdon, T.J., van Leeuwen, D.G., Lopez, A.V., Curran, K.J., Daniyan, A.F., and Brentjens, R.J. (2019). CD40 Ligand-Modified Chimeric Antigen Receptor T Cells Enhance Antitumor Function by Eliciting an Endogenous Antitumor Response. Cancer Cell *35*, 473–488. https://doi.org/10.1016/j.ccell.2019.02.006.

89. Brentjens, R.J., Latouche, J.B., Santos, E., Marti, F., Gong, M.C., Lyddane, C., King, P.D., Larson, S., Weiss, M., Rivière, I., et al. (2003). Eradication of systemic B-cell tumors by genetically targeted human T lymphocytes co-stimulated by CD80 and interleukin-15. Nat. Med. *9*, 279–286. https://doi.org/10.1038/nm827.

90. Davila, M.L., Kloss, C.C., Gunset, G., and Sadelain, M. (2013). CD19 CAR-targeted T cells induce long-term remission and B Cell Aplasia in an immunocompetent mouse model of B cell acute lymphoblastic leukemia. PLoS One *8*, e61338. https://doi.org/10.1371/journal.pone.0061338.

91. Zhang, Z., Karthaus, W.R., Lee, Y.S., Gao, V.R., Wu, C., Russo, J.W., Liu, M., Mota, J.M., Abida, W., Linton, E., et al. (2020). Tumor Microenvironment-Derived NRG1 Promotes Antiandrogen Resistance in Prostate Cancer. Cancer Cell *38*, 279–296. https://doi.org/10.1016/j.ccell.2020.06.005.

92. Cerami, E., Gao, J., Dogrusoz, U., Gross, B.E., Sumer, S.O., Aksoy, B.A., Jacobsen, A., Byrne, C.J., Heuer, M.L., Larsson, E., et al. (2012). The cBio cancer genomics portal: an open platform for exploring multidimensional cancer genomics data. Cancer Discov. *2*, 401–404. https://doi.org/10.1158/2159-8290.CD-12-0095.

93. Gao, J., Aksoy, B.A., Dogrusoz, U., Dresdner, G., Gross, B., Sumer, S.O., Sun, Y., Jacobsen, A., Sinha, R., Larsson, E., et al. (2013). Integrative analysis of complex cancer genomics and clinical profiles using the cBioPortal. Sci. Signal. *6*, pl1. https://doi.org/10.1126/scisignal.2004088.

94. de Bruijn, I., Kundra, R., Mastrogiacomo, B., Tran, T.N., Sikina, L., Mazor, T., Li, X., Ochoa, A., Zhao, G., Lai, B., et al. (2023). Analysis and Visualization of Longitudinal Genomic and Clinical Data from the AACR Project GENIE Biopharma Collaborative in cBioPortal. Cancer Res. *83*, 3861–3867. https://doi.org/10.1158/0008-5472.CAN-23-0816.

95. Andreatta, M., and Carmona, S.J. (2021). UCell: Robust and scalable single-cell gene signature scoring. Comput. Struct. Biotechnol. J. *19*, 3796–3798. https://doi.org/10.1016/j.csbj.2021.06.043.

96. Wickham, H. (2016). ggplot2: Elegant Graphics for Data Analysis (Springer-Verlag New York).

STAR★METHODS

KEY RESOURCES TABLE

REAGENT OR RESOURCE	SOURCE	IDENTIFIER
Antibodies		
Rabbit monoclonal MSLN Alexa Fluor® 594 (SP74)	Abcam	Cat# ab311842; RRID: AB_2923526
Rabbit monoclonal αSMA Alexa Fluor® 488 (D4K9N)	Cell Signaling CST	Cat #34105; RRID: AB_2734735
Rabbit monoclonal CC3 Alexa Fluor® 750 (D3E9)	Cell Signaling CST	Cat# 97774; RRID: AB_3720264
Rabbit monoclonal CD11B Alexa Fluor® 647 (D6X1N)	Cell Signaling CST	Cat# 79750; RRID: AB_3720244
Rabbit monoclonal CD11C Alexa Fluor® 555 (D3V1E)	Cell Signaling CST	Cat# 77882; RRID: AB_3331656
Rabbit monoclonal CD163 Alexa Fluor® 488 (D6U1J)	Cell Signaling CST	Cat# 71411; RRID: AB_3720265
Rabbit monoclonal CD163 Alexa Fluor® 647 (D6U1J)	Cell Signaling CST	Cat# 39093; RRID: AB_3720266
Rabbit monoclonal CD20 Alexa Fluor® 555 (E7B7T)	Cell Signaling CST	Cat# 81546; RRID: AB_3720267
Mouse monoclonal CD31 Alexa Fluor® 488 (89C2)	Cell Signaling CST	Cat# 42777; RRID: AB_3720268
Mouse monoclonal CD31 Alexa Fluor® 555 (89C2)	Cell Signaling CST	Cat# 61255; RRID: AB_3662787
Rabbit monoclonal CD3Ɛ Alexa Fluor® 555 (D7A6E)	Cell Signaling CST	Cat# 57869; RRID: AB_3668891
Rabbit monoclonal CD4 Alexa Fluor® 647 (EPR6855)	Abcam	Cat# ab196147; RRID: AB_2923526
Rabbit monoclonal CD45 Alexa Fluor® 647(D9M8I)	Cell Signaling CST	Cat# #19744; RRID: AB_3720269
Rabbit monoclonal CD68 Alexa Fluor® 555 (D4B9C)	Cell Signaling CST	Cat# 23308; RRID: AB_2922446
Rabbit monoclonal CD8A Alexa Fluor® 555 (D8A8Y)	Cell Signaling CST	Cat# 77909; RRID: AB_3720270
Rabbit monoclonal FAP Unconjugated (EPR20021)	Abcam	Cat# ab271976; RRID: AB_3676372
Mouse monoclonal FOXP3 Unconjugated (236A/E7)	Invitrogen	Cat# 14-4777-82; RRID: AB_467556
Rabbit monoclonal GZMB Alexa Fluor® 555 (D6E9W)	Cell Signaling CST	Cat# 29268; RRID: AB_3720271
Mouse monoclonal HLA-DR (MHCII) Alexa Fluor® 488 (TAL 1B5)	Abcam	Cat# ab309369; RRID: AB_3720257
Rabbit monoclonal Ki67 Alexa Fluor® 555 (B56)	BD Pharmingen	Cat# 558617; RRID: AB_647108
Mouse monoclonal PanCK Alexa Fluor® 488 (ae1/ae3)	Thermofisher	Cat# 53-9003-80; RRID: AB_1834351
Mouse monoclonal PanCK Alexa Fluor® 750 (ae1/ae3)	Novus Biologicals	Cat# NBP2-3320AF750; RRID: AB_2868569
Goat polyclonal Human uPAR Unconjugated	R&D Systems	Cat# AF807; RRID: AB_355618
Rat monoclonal Vimentin Alexa Fluor® 750 (280618)	R&D Systems	Cat# IC2105S; RRID: AB_3654986
Goat polyclonal Mouse uPAR Unconjugated	R&D Systems	Cat# AF534; RRID: AB_2165351

(*Continued on next page*)

Continued

REAGENT OR RESOURCE	SOURCE	IDENTIFIER
Rabbit monoclonal Myc-Tag (71D10)	Cell Signaling CST	Cat# #2278; RRID: AB_490778
Rabbit monoclonal GZMB, Unconjugated (D6E9W)	Cell Signaling CST	Cat# #46890; RRID: AB_2799313
Rabbit monoclonal CD45, Unconjugated (2B11+PD7/26)	Agilent Technologies	Cat# M0701; RRID: AB_2314143
Rabbit monoclonal CD3, Unconjugated (MRQ-39)	LSBio	Cat# C202826; RRID: AB_3720273
Rabbit monoclonal αSMA, Unconjugated (D4K9N)	Cell Signaling CST	Cat# #19245; RRID: AB_2734735
Mouse monoclonal P53 Alexa Fluor® 594 (DO-1)	Novus Biologicals	Cat# NBP2-50538AF594; RRID: AB_3328659
Mouse monoclonal P53 Alexa Fluor® 647 (DO-7)	SantaCruz	Cat# sc-47698 AF647; RRID: AB_3106885
Rabbit monoclonal ARG1 Alexa Fluor® 555 (D4E3M)	Cell Signaling CST	Cat# 35298; RRID: AB_3720274
Rabbit monoclonal CDKN2A/P16INK4a Alexa Fluor® 647 (EPR1473)	Abcam	Cat# ab192054; RRID: AB_2889194
Rabbit monoclonal Cytokeratin 17 Alexa Fluor® 488 (EP1623)	Abcam	Cat# ab185032; RRID: AB_2889195
Rabbit monoclonal MPO Alexa Fluor® 488 (E1E7I)	Cell Signaling CST	Cat# 49422; RRID: AB_3720281
Donkey anti-Rabbit IgG (H+L) Highly Cross-Adsorbed Secondary Antibody, Alexa Fluor™ 488	Invitrogen	Cat# A21206; RRID: AB_2535792
Donkey anti-Mouse IgG (H+L) Highly Cross-Adsorbed Secondary Antibody, Alexa Fluor™ 488	Invitrogen	Cat# A21202; RRID: AB_141607
Donkey anti-Rabbit IgG (H+L) Highly Cross-Adsorbed Secondary Antibody, Alexa Fluor™ 594	Invitrogen	Cat# A21207; RRID: AB_141637
Donkey anti-Mouse IgG (H+L) Highly Cross-Adsorbed Secondary Antibody, Alexa Fluor™ 594	Invitrogen	Cat# A21203; RRID: AB_2535789
Donkey anti-Goat IgG (H+L) Cross-Adsorbed Secondary Antibody, Alexa Fluor™ 594	Invitrogen	Cat# A11058; RRID: AB_2534105
Goat anti-Rat IgG (H+L) Cross-Adsorbed Secondary Antibody, Alexa Fluor™ 594	Invitrogen	Cat# A11007; RRID: AB_10561522
Donkey anti-Goat IgG (H+L) Cross-Adsorbed Secondary Antibody, Alexa Fluor™ 555	Invitrogen	Cat# A21432; RRID: AB_2535853
Donkey anti-Rabbit IgG (H+L) Highly Cross-Adsorbed Secondary Antibody, Alexa Fluor™ Plus 647	Invitrogen	Cat# A32795; RRID: AB_2866496
Donkey anti-mouse Alexa Fluor® 750	Abcam	Cat# ab175738; RRID: AB_3720223
Mouse monoclonal Hu HLA-DR BUV395 (L203)	BD Biosciences	Cat# 752492; RRID: AB_2917485
Mouse monoclonal anti-human CD4 BUV395 (SK3)	BD Biosciences	Cat# 563552; RRID: AB_2738275
Mouse monoclonal Hu CD45RO BUV496 (UCHL1)	BD Biosciences	Cat# 749888; RRID: AB_2874128
Mouse monoclonal Hu CD19 BUV563 (SJ25C1)	BD Biosciences	Cat# 612916; RRID: AB_2870201
Mouse monoclonal Hu CD44 BUV563 (G44-26)	BD Biosciences	Cat# 741373; RRID: AB_2870872
Mouse monoclonal Hu CD3 BUV615 (UCHT1)	BD Biosciences	Cat# 612992; RRID: AB_2870263
Mouse monoclonal Hu CD4 BUV737 (L200)	BD Biosciences	Cat# 749213; RRID: AB_2873591
Mouse monoclonal Hu CD279 BUV737 (EH12.1)	BD Biosciences	Cat# 612791; RRID: AB_2870118

(*Continued on next page*)

Continued

REAGENT OR RESOURCE	SOURCE	IDENTIFIER
Mouse monoclonal Hu CD69 BUV805 (FN50)	BD Biosciences	Cat# 748763; RRID: AB_2857327
Mouse monoclonal Hu CD110 BV421 (S16017A)	Biolegend	Cat# 393812; RRID: AB_2750511
Mouse monoclonal Hu CD62L BV421 (DREG-56)	BD Biosciences	Cat# 563862; RRID: AB_2738455
Mouse monoclonal Hu CD8 Pacific Blue (SK1)	Biolegend	Cat# 344718; RRID: AB_10551438
Mouse monoclonal Hu CD45RA BV480 (HI100)	BD Biosciences	Cat# 566114; RRID: AB_2739516
Mouse monoclonal Hu hCD45 PacO (HI30)	Invitrogen	Cat# MHCD4530; RRID: AB_10376143
Mouse monoclonal Hu CD16 SuperBright 600 (CB16)	Invitrogen	Cat# 63-0168-42; RRID: AB_2662479
Mouse monoclonal Hu CD366 (TIM3) BV605 (F38-E2E)	Biolegend	Cat# 345017; RRID: AB_2562194
Mouse monoclonal Hu CD38 BV650 (HB-7)	Biolegend	Cat# 356620; RRID: AB_2566233
Mouse monoclonal Hu CD71 BV711 (M-A712)	BD Biosciences	Cat# 5633767; RRID: AB_2738413
Mouse monoclonal Hu CD3 BV750 (SK7)	BD Bioscience	Cat# 747058; RRID: AB_2871816
Mouse monoclonal Hu CD123 BV785 (6H6)	Biolegend	Cat# 306032; RRID: AB_2566448
Mouse monoclonal Hu CCR7 BV785 (G043H7)	Biolegend	Cat# 353229; RRID: AB_2561371
Mouse monoclonal Hu uPAR PE (VIM5)	Biolegend	Cat# 336906; RRID: AB_2165468
Mouse monoclonal Hu LNGFR PE (C40-1457)	BD Biosciences	Cat# 557196; RRID: AB_3396599
Mouse monoclonal Hu CD90 PE/Dazzle 594 (5E10)	Biolegend	Cat# 328134; RRID: AB_2566343
Mouse monoclonal Hu CD41a PE-Cy5 (HIP8)	Biolegend	Cat# 303708; RRID: AB_314378
Mouse monoclonal Hu CD33 PE-Cy7 (P67.6)	Biolegend	Cat# 366618; RRID: AB_2566420
Mouse monoclonal Hu CD45RA FITC (HI100)	eBiosciences	Cat# 11-0458-42; RRID: AB_11219672
Mouse monoclonal Hu CD14 SparkBlue 550 (63D3)	Biolegend	Cat# 367148; RRID: AB_2832724
Mouse monoclonal Hu CD3 PerCP (UCHT1)	Agilent Technologies	Cat# PR70201-1; RRID: AB_3722754
Mouse monoclonal Hu CD11c PerCP-Cy5.5 (Bu15)	Biolegend	Cat# 337210; RRID: AB_1279069
Mouse monoclonal Hu CD223(LAG3) PerCP-eFluor710 (3DS223H)	Invitrogen	Cat# 46-2239-42; RRID: AB_2573732
Mose monoclonal Hu LNGFR APC (ME20.4)	Biolegend	Cat# 345108; RRID: AB_10645515
Mouse monoclonal Hu CD25 APC (BC96)	Invitrogen	Cat# 17-0259-42; RRID: AB_1582219
Mouse monoclonal Hu CD45 APC (2D1)	Invitrogen	Cat# 17-9459-42; RRID: AB_10718532
Mouse monoclonal Hu CD34 R718 (581)	BD Biosciences	Cat# 566973; RRID: AB_2869980
Rat monoclonal Ms CD45 APC-F750 (30-F11)	Biolegend	Cat# 103154; RRID: AB_2572116
Mouse monoclonal Hu CD8 APC-Cy7 (SK1)	BD Biosciences	Cat# 557834; RRID: AB_396892
Mouse monoclonal Hu CD14 APC/Cy7 (63D3)	Biolegend	Cat# 367107; RRID: AB_2566709
Mouse monoclonal Hu CD206 BV711 (15-2)	Biolegend	Cat# 321136; RRID: AB_2687200
Mouse monoclonal Hu CD31 BV785 (WM59)	Biolegend	Cat# 303148; RRID: AB_2860782
Mouse monoclonal Hu CD14 V450 (MφP9)	BD Biosciences	Cat# 560349; RRID: AB_1645559
Mouse monoclonal Hu CD3 BV510 (OKT3)	Biolegend	Cat# 317332; RRID: AB_2561943
Mouse monoclonal Hu CD19 BV510 (SJ25C1)	BD Biosciences	Cat# 562953; RRID: AB_2737914
Mouse monoclonal Hu CD56 BV510 (NCAM16.2)	BD Biosciences	Cat# 563041; RRID: AB_2732786
Mouse monoclonal Hu CD15 BV510 (W6D3)	Biolegend	Cat# 323028; RRID: AB_2563400
Rat monoclonal Ms Ter119 PE/Cy5 (TER-119)	Biolegend	Cat# 116209; RRID: AB_313710
anti-mouse CD45R/B220 PE/Cy5 (RA3-6B2)	Biolegend	Cat# 103210; RRID: AB_312995
Mouse monoclonal Ms NK1.1 PE/Cy5 (PK136)	Biolegend	Cat# 108716; RRID: AB_493590

(*Continued on next page*)

Continued

REAGENT OR RESOURCE	SOURCE	IDENTIFIER
Armenian hamster monoclonal Ms CD3 PE/Cy5 (145-2C11)	Biolegend	Cat# 100309; RRID: AB_312674
Rat monoclonal Ms CD8 Pacific Blue (53-6.7)	Biolegend	Cat# 100725; RRID: AB_493425
Rat monoclonal Ms CD3 BV650 (17A2)	Biolegend	Cat# 100229; RRID: AB_11204249
Mouse monoclonal Ms CD45.1 APC/Cy7 (A20)	Biolegend	Cat# 110716; RRID: AB_313505
Rat monoclonal Ms Ly6G BV605 (1A8)	BD Biosciences	Cat# 563005; RRID: AB_2737946
Rat monoclonal Ms Ly6C BV711 (HK1.4)	Biolegend	Cat# 128037; RRID: AB_2562630
Mouse monoclonal Hu EPCAM APC (9C4)	Biolegend	Cat# 324207; RRID: AB_756081
Rat monoclonal Hu CD11b BV785 (M1/70)	Biolegend	Cat# 101243; RRID: AB_2561373
Armenian hamster monoclonal Ms CD11c PE/Cy5 (N418)	Invitrogen	Cat# 35-0114-82; RRID: AB_469709
Rat monoclonal Ms c-Kit BV605 (ACK2)	Biolegend	Cat# 135125; RRID: AB_2562446
Rat monoclonal Ms CD16/32 BV510 (93)	Biolegend	Cat# 101333; RRID: AB_2563692
Rat monoclonal Ms CD34 FITC (RAM34)	BD Biosciences	Cat# 560238; RRID: AB_1645242
Rat monoclonal Ms Ly-6A/E (Sca1) PE/Cy7 (D7)	Biolegend	Cat# 108114; RRID: AB_493596
Rat monoclonal Ms CD3 BV496 (17A2)	BD Biosciences	Cat# 741117; RRID: AB_2870707
Rat monoclonal Ms CD45 BUV563 (30-F11)	BD Biosciences	Cat# 612924; RRID: AB_2870209
Rat monoclonal Ms Ly6G PerCP/Cy5.5 (1A8)	Tonbo Bioscience	Cat# 65-1276-U100; RRID: AB_2621899
Mouse monoclonal Hu CD19 BUV805 (HIB19)	BD Biosciences	Cat# 568331; RRID: AB_3684187
Mouse monoclonal Hs CD15 BUV496 (7C3.rMAb)	BD Biosciences	Cat# 568916; RRID: AB_3684631
Rat monoclonal MsCD115 (CSF-1R) PE (AFS98)	Biolegend	Cat# 135506; RRID: AB_1937253
Mouse monoclonal Hu HLA-DR PE/Cy7 (G46-6)	BD Biosciences	Cat# 560651; RRID: AB_1727528
Rat monoclonal Ms/Hu CD11b AF700 (M1/70)	Biolegend	Cat# 101222; RRID: AB_493705
Human monoclonal uPAR antibody	Genescript	Produced from GeneScript
Human monoclonal human GPNMB AF350	MedChemExpress	Cat# HY-P99205; RRID: AB_3695023
Rat monoclonal Ms CD184 (CXCR4) APC (2B11)	Invitrogen	Cat# 17-9991-80; RRID: AB_10670877
Rat monoclonal Hu PDPN FITC (NC-08)	Biolegend	Cat# 337026; RRID: AB_2750286
Mouse monoclonal Hu CD140α (PDGFRα) BV605 (16A1)	BD Biosciences	Cat# 752899; RRID: AB_2917854
anti-human PDGFRb AF750	R&D Systems	Cat# FAB1236S; RRID: AB_3646214
Rat monoclonal Ms uPAR AF700 (109801)	R&D Systems	Cat# FAB531N; RRID: AB_3650910
Goat polyclonal Ms uPAR PE	Novus	Cat# AF534P RRID: AB_2165351
Mouse monoclonal Ms uPAR PE (109801)	R&D Systems	Cat# FAB531P; RRID: AB_10640498
Bacterial and virus strains		
NEB stable competent cells	New England BioLabs	Cat# C3040I
Biological samples		
Human colorectal cancer TMA	TissueArray	CO2001a
Human Breast cancer TMA	TissueArray	BR931
Human multi organ cancer TMA	TissueArray	BC000119b
Human prostate cancer TMA	TissueArray	PR633a
Human brain tumor TMA	TissueArray	GL803d
Others human cancer TMA	Memorial Sloan Kettering Cancer Center	N/A
Chemicals, peptides, and recombinant proteins		
Annexin V Binding Buffer 5X Concentrate	Invitrogen	Cat# V13246

(*Continued on next page*)

Continued

REAGENT OR RESOURCE	SOURCE	IDENTIFIER
7-AAD Viability Staining Solution	Biolegend	Cat# 420404
CountBright Absolute Counting Beads	Invitrogen	Cat# C36950
UltraComp Beads Plus Compensation Beads	Invitrogen	Cat# 01-3333-42
Brilliant Stain Buffer	BD Biosciences	Cat# 566349
Human BD Fc Block	BD Biosciences	Cat# 564220
Mouse BD Fc Block	BD Biosciences	Cat# 553142
QuantiBRITE PE Phycoerythrin Fluorescence Quantification Kit	BD Biosciences	Cat# 340495
Vector TrueVIEW Autofluorescence Quenching Kit	Vector Laboratories	Cat# SP-8400-15
One Shot™ Stbl3™ Chemically Competent E. coli	New England BioLabs	Cat# C737303
S.O.C Media	Invitrogen	Cat# 46-0821
ProLong Gold antifade reagent	Invitrogen	Cat# P36930
TheraPEAK® X-VIVO® 15 Serum-free Hematopoietic Cell Medium	Lonza	Cat# BEBP02-061Q
Normal Human Serum	GeminiBio	Cat# 100-110-100
Neon Transfection System 10 μL Kit	Thermo Fisher Scientific	Cat# N1096
Neon NxT Electroporation System	Thermo Fisher Scientific	Cat# NEON18S
Alt-R™ Cas9 Electroporation Enhancer, 2 nmol	Integrated DNA Technologies	Cat# 1075915
Hydrogen peroxide solution 30% (w/w) in H_2O	Sigma-Aldrich	Cat# H1009
Ethanol absolute	Fisher Scientific	Cat# 04-355-223
Antigen Unmasking Solution, Tris-Based	Vector Laboratories	Cat# H3301-250
Antigen Unmasking Solution, Citric Acid Based	Vector Laboratories	Cat# H-3300-250
Glycerol	Thermo Fisher Scientific	Cat# AC327255000
Bovine Serum Albumin	GeminiBio	Cat# 700-100P
Alexa Fluor™ 750 NHS Ester (Succinimidyl Ester)	Thermo Fisher Scientific	Cat# A20111
LIVE/DEAD™ Fixable Aqua Dead Cell Stain Kit, for 405 nm excitation	Thermo Fisher Scientific	Cat# L34957
Collagenase Type 1	Worthington Biochemical Corporation	Cat# LS004197
TaqMan Reverse Transcription Reagents	Applied Biosystems	Cat# N8080234
SYBR Green Universal Master Mix	Applied Biosystems	Cat# 4309155
Permount Mounting Media	Fisher Scientific	Cat# SP15-100
Picric acid	Sigma-Aldrich	Cat# 197378-100G
Fast Green FCF	Sigma-Aldrich	Cat# F7252-5G
Direct Red 80	Sigma-Aldrich	Cat# 365548-5G
Critical commercial assays		
DuoSet ELISA Ancillary Reagent Kit 2	R&D Systems	Cat# DY008B
Human uPAR DuoSet ELISA	R&D Systems	Cat# DY807
EasySep™ Release Human CD3 Positive Selection Kit	Stemcell Technologies	Cat# 17751
CTS™ (Cell Therapy Systems) Dynabeads™ CD3/CD28	Gibco	Cat# 40203D
Pan T Cell Isolation Kit II, mouse	Miltenyi Biotec	Cat# 130-096-130
Pan T Cell Isolation Kit, human	Miltenyi Biotec	Cat# 130-095-535
Dynabeads™ Mouse T-Activator CD3/CD28 for T-Cell Expansion and Activation	Gibco	Cat# 11452D
EasySep Human Monocyte Enrichment Kit without CD16 Depletion	StemCell Technologies	Cat# 19058
EasySep Human Monocyte Isolation Kit	StemCell Technologies	Cat# 19359

(*Continued on next page*)

Continued

REAGENT OR RESOURCE	SOURCE	IDENTIFIER
CliniMACS CD34 GMP Microbeads	Miltenyi Biotec	Cat# 170-076-711
STEMSpan SFEM II	Stem Cell Technologies	Cat# 9605
RNeasy Mini Kit	Qiagen	Cat# 74104
Remove-iT PNGase F	New England BioLabs	Cat# P0706S
Chitin Magnetic Beads	New England BioLabs	Cat# E8036
Cytofix/Cytoperm Fixation/Permeabilization Solution Kit	BD Bioscience	Cat# 554714
Intracellular Fixation and Permeabilization Buffer Set Kit	eBioscience	Cat# 88-8824-00
Deposited data		
10x Xenium dataset	This study	GEO: GSE293800, token number: gherqoqaljifnox
TCGA RNA-seq, clinical, and mutational data	The Cancer Genome Atlas (TCGA)	https://portal.gdc.cancer.gov/
RNAseq of matched pre and post chemotherapy HGSOC	Javellana et al.[61]	N/A
RNA-seq data of etoposide- and alisertib-induced senescent cells	Jochems et al.[26]	https://www.ebi.ac.uk/arrayexpress%20 Accession: %20E-MTAB-9970
RNAseq of cisplatin treated MPB1 ovarian cancer cell	Paffenholz et al.[58]	GEO: GSE317451
scRNAseq HGSOC (MSK SPECTRUM cohort)	Vázquez-García et al.[37]	GEO: GSE180661
scRNAseq CRC (HTAN MSK cohort)	Moorman et al.[77]	dbGaP Study Accession: phs002371.v6.p1
scRNAseq of NSCLC pre and post therapy	Maynard et al.[78]	PRJNA591860
scRNAseq of LUAD	Xiang et al.[35]	GSE253013
scRNAseq of PDAC	Steele et al.[38]	GSE155698
scRNAseq of liver cancer	Xue et al.[36]	PRJCA007744
Experimental models: Cell lines		
Human: U87-MG	ATCC	Cat# HTB-14; RRID:CVCL_0022
Human: SW480	ATCC	Cat# CCL-228; RRID:CVCL_0546
Human: SW620	ATCC	Cat# CCL-22; RRID:CVCL_0547
Human: CaCo2	Karuna Ganesh (MSKCC)	N/A
Human: HCT116	Karuna Ganesh (MSKCC)	N/A
Human: LoVo	ATCC	Cat# CCL-229; RRID:CVCL_0399
Human: DLD1	ATCC	Cat# CCL-221; RRID:CVCL_0248
Human: PC3	Charles Sawyers (MSKCC)	N/A
Human: DU145	Charles Sawyers (MSKCC)	N/A
Human: VCaP	Charles Sawyers (MSKCC)	N/A
Human: 22Rv1	Charles Sawyers (MSKCC)	N/A
Human: CWR22PC	Ayush Dagvadorji (Kimmel Cancer Center)	N/A
Human: LNCaP	Charles Sawyers (MSKCC)	N/A
Human: MCF-7	Sarat Chandarlapaty (MSKCC)	N/A
Human: MDA-MB-231	ATCC	Cat# HTB-26; RRID: CVCL_0062
Human: MDA-MB-468	Sarat Chandarlapaty (MSKCC)	Cat# HTB-132; RRID: CVCL_0419
Human: MDA-MB-453	Sarat Chandarlapaty (MSKCC)	Cat# HTB-131; RRID: CVCL_0418
Human: MDA-MB-436	Sarat Chandarlapaty (MSKCC)	Cat# HTB-130; RRID: CVCL_0623
Human: CAMA1	Sarat Chandarlapaty (MSKCC)	Cat# HTB-21; RRID: CVCL_1115
Human: 769-P	A. Ari Hakimi (MSKCC)	N/A
Human: 786-O	A. Ari Hakimi (MSKCC)	N/A
Human: A498	A. Ari Hakimi (MSKCC)	N/A
Human: Hela	Xuejun Jiang (MSKCC)	N/A

(*Continued on next page*)

Continued

REAGENT OR RESOURCE	SOURCE	IDENTIFIER
Human: JHRCC62A	A. Ari Hakimi (MSKCC)	N/A
Human: JHRCC228	A. Ari Hakimi (MSKCC)	N/A
Human: JHRCC611m1	A. Ari Hakimi (MSKCC)	N/A
Human: JHRCC12	A. Ari Hakimi (MSKCC)	N/A
Human: U2OS	Xuejun Jiang (MSKCC)	N/A
Human: BT474	Sarat Chandarlapaty (MSKCC)	N/A
Human: SKBR3	Sarat Chandarlapaty (MSKCC)	N/A
Human: BT549	Sarat Chandarlapaty (MSKCC)	N/A
Human: T47D	Sarat Chandarlapaty (MSKCC)	N/A
Human: PANC1	ATCC	Cat# CRL-1469; RRID: CVCL_0480
Human: MIAPACA2	ATCC	Cat# CRL-1420; RRID: CVCL_ 0428
Human: AsPC1	ATCC	Cat# CRL-1682; RRID: CVCL_0152
Human: HPAC	ATCC	Cat# CRL-2119; RRID: CVCL_3517
Human: BxPC3	ATCC	Cat# CRL-1687; RRID: CVCL_0186
Human: HPAF-II	ATCC	Cat# CRL-1997; RRID: CVCL_0313
Human: SU86.86	ATCC	Cat# CRL-1827; RRID: CVCL_1555
Human: NCI-H28	Charles Rudin (MSKCC)	N/A
Human: NCI-H2452	Charles Rudin (MSKCC)	N/A
Human: MSTO-211H	ATCC	Cat# CRL-2081; RRID: CVCL_1430
Human: NCI-H526	Charles Sawyers (MSKCC)	N/A
Human: NCI-H1650	Maria Skamagki (MSKCC)	N/A
Human: NCI-H460	Maria Skamagki (MSKCC)	N/A
Human: NCI-H1703	Maria Skamagki (MSKCC)	N/A
Human: NCI-H2030	Maria Skamagki (MSKCC)	N/A
Human: NCI-H2286	ATCC	Cat# CRL-5938; RRID: CVCL_1545
Human: A549	ATCC	Cat# CCL-185; RRID: CVCL_0023
Human: PC9	Junhong Choi (MSKCC)	N/A
Human: Tyk-nu	Juan R. Cubillos-Ruiz (Cornell)	N/A
Human: PA-1	ATCC	Cat# CRL-1572; RRID: CVCL_0479
Human: ES-2	ATCC	Cat# CRL-1978; RRID: CVCL_3509
Human: COV644	Sigma-Aldrich	Cat# 07071908; RRID: CVCL_2425
Human: OVCAR4	Jason Lewis (MSKCC)	N/A
Human: OVCAR5	Jason Lewis (MSKCC)	N/A
Human: OVCAR8	Jason Lewis (MSKCC)	N/A
Human: OV90	ATCC	Cat# CRL-3585; RRID: CVCL_3768
Human: Caov-4	ATCC	Cat# HTB-76; RRID: CVCL_0202
Human: HEY-T30	ATCC	Cat# CRL-3252; RRID: CVCL_2Z96
Human: MES-OV	ATCC	Cat# CRL-3272; RRID: CVCL_CZ92
Human: UWB1.289	ATCC	Cat# CRL-2945; RRID: CVCL_B078
Human: SKOV3	ATCC	Cat# HTB-77; RRID: CVCL_1345
Human: Kuramochi	Juan R. Cubillos-Ruiz (Cornell)	N/A
Human: 8000S	George Li (MSKCC)	N/A
Human: 4746	George Li (MSKCC)	N/A
Human: DDLS8817	George Li (MSKCC)	N/A
Human: VOA6406	Mark Carey (UBC)	N/A
Human: VOA4627	Mark Carey (UBC)	N/A
Human: VOA7681	Mark Carey (UBC)	N/A
Human: BEAS-2B	ATCC	Cat# CRL-3588; RRID: CVCL_0168
Human: MCF-10A	ATCC	Cat# CRL-10317; RRID: CVCL_0598

(*Continued on next page*)

Continued

REAGENT OR RESOURCE	SOURCE	IDENTIFIER
Human: HEK293T	ATCC	Cat# CRL-3216; RRID: CVCL_0063
Mouse: Kras$^{G12D/+}$;Trp53$^{R172H/+}$ (KP)	Tyler Jacks (MIT)	N/A
Mouse: MYC;Trp53$^{-/-}$;Brca1$^{-/-}$ (MPB1)	Stella Paffenholz (MSKCC)	N/A
Mouse: MYC;Trp53$^{-/-}$ (MP)	Stella Paffenholz (MSKCC)	N/A
Experimental models: Organoids		
Human CRC Organoid 136p	Karuna Ganesh (MSKCC)	N/A
Human MOC Organoid (ChanSMOV)	Elisa de Stanchina (MSKCC)	N/A
Experimental models: Organisms/strains		
Mouse: C57BL/6N	Charles River Laboratories	Stock# 027
Mouse: NOD.Cg-KitW-41JTyr+ Prkdcscid Il2rgtm1Wjl/ThomJ (NBSGW)	Jackson Laboratories	Stock# 026622
Mouse: Crl:NU(NCr)-Foxn1nu	Charles River Laboratories	Stock# 490
Mouse: NOD-scid IL2Rgnull (NSG)	Jackson Laboratories	Stock# 005557
Oligonucleotides		
Mm.Cas9.PLAUR.1.AA (mouse)	IDT	ACACTCGAGGTAACGGCCCT
Mm.Cas9.PLAUR.1.AB (mouse)	IDT	AGGACCATGAGTTACCGCAT
Hs.Cas9.PLAUR.1.AA (human)	IDT	GACCACGATCGTGCGCTTGT
Hs.Cas9.PLAUR.1.AB (human)	IDT	GCATTCGAGGTAACGGCTTC
sgTRAC (human)	Eyquem et al.[60]	CAGGGTTCTGGATATCTGT
Rplp0_Fwd (mouse)	PrimerBank (MGH)	GGTGGAACGTCGTCTTCGT
Rplp0_Rev (mouse)	PrimerBank (MGH)	TCGTGGTGATACCCAAAACCT
Cdkn1a(p21)_Fwd (mouse)	PrimerBank (MGH)	CCTGGTGATGTCCGACCTG
Cdkn1a(p21)_Rev (mouse)	PrimerBank (MGH)	CCATGAGCGCATCGCAATC
Plaur_Fwd (mouse)	PrimerBank (MGH)	CAGAGCTTTCCACCGAATGG
Plaur_Rev (mouse)	PrimerBank (MGH)	GTCCCCGGCAGTTGATGAG
RPLP0_Fwd (human)	PrimerBank (MGH)	AGCCCAGAACACTGGTCTC
RPLP0_Rev (human)	PrimerBank (MGH)	ACTCAGGATTTCAATGGTGCC
PLAUR_Fwd (human)	PrimerBank (MGH)	TGTAAGACCAACGGGGATTGC
PLAUR_Rev (human)	PrimerBank (MGH)	AGCCAGTCCGATAGCTCAGG
CDKN1A(p21) Fwd (human)	PrimerBank (MGH)	TGTCCGTCAGAACCCATGC
CDKN1A(p21) Rev (human)	PrimerBank (MGH)	AAAGTCGAAGTTCCATCGCTC
CDKN2A(p16) Fwd (human)	PrimerBank (MGH)	ATGGAGCCTTCGGCTGACT
CDKN2A(p16) Rev (human)	PrimerBank (MGH)	GTAACTATTCGGTGCGTTGGG
IL1B_Fwd (human)	PrimerBank (MGH)	CCACAGACCTTCCAGGAGAATG
IL1B_Rev (human)	PrimerBank (MGH)	GTGCAGTTCAGTGATCGTACAGG
IL6_Fwd (human)	PrimerBank (MGH)	AGACAGCCACTCACCTCTTCAG
IL6_Rev (human)	PrimerBank (MGH)	TTCTGCCAGTGCCTCTTTGCTG
Recombinant DNA		
pSFG-uPAR(A1)-h.28z-P2A-LNGFR	This paper	N/A
pSFG-uPAR(T1)-h.28z-P2A-LNGFR	This paper	N/A
pSFG-CD19-h.28z-P2A-LNGFR	Haubner et al.[59]	N/A
pSFG-uPAR(A1)-h.28z.1xx-P2A-LNGFR	This paper	N/A
pSFG-uPAR(T1)-h.28z.1xx-P2A-LNGFR	This paper	N/A
pSFG-CD19-h.28z.1xx-P2A-LNGFR	Feucht et al.[50]	N/A
pSFG-uPAR-m.28z-MycTag	Amor, Feucht, Leiboldet al.[25]	N/A
Software and algorithms		
Adobe Illustrator	Adobe	https://www.adobe.com/

(*Continued on next page*)

Continued

REAGENT OR RESOURCE	SOURCE	IDENTIFIER
GraphPad Prism v10	GraphPad Software	https://www.graphpad.com/
CaseViewer	3dHistech	https://www.3dhistech.com/news/caseviewer-becomes-slideviewer/
Flow Jo	BD Life Sciences	https://www.flowjo.com/
Mx Workflow	Leica Microsystems	https://www.leica-microsystems.com/products/light-microscopes/p/cell-dive/
Cell Dive Acquisition	Leica Microsystems	https://www.leica-microsystems.com/products/light-microscopes/p/cell-dive/
HALO	Indica labs	https://indicalab.com/halo/
DESeq2	Love et al.[79]	https://bioconductor.org/packages/release/bioc/html/DESeq2.html
Seurat	Hao et al.[80]	https://github.com/satijalab/seurat
DoubletFinder	McGinnis et al.[81]	https://github.com/chris-mcginnis-ucsf/DoubletFinder
STAR	Dobin et al.[82]	https://github.com/alexdobin/STAR
featureCounts	Liao et al.[83]	https://subread.sourceforge.net/
dplyr	Wickham et al.[84]	https://dplyr.tidyverse.org/
Enrichr	Chen et al.	https://maayanlab.cloud/Enrichr/
GSEA	Subramanian et al.[85]	https://www.gsea-msigdb.org/gsea/index.jsp
Xenium	10X Genomics	https://www.10xgenomics.com
Xenogen	Now Revvity (IVIS Imaging)	https://www.revvity.com/
ImageJ/FIJI	ImageJ	https://imagej.net

EXPERIMENTAL MODEL AND STUDY PARTICIPANT DETAILS

Cell lines and organoids

Cell lines were maintained in a humidified incubator at 37°C with 5% CO_2. Human ovarian cancer Tyk-nu cell line (gift from Dr. Camilla Salvagno), human lung cancer cell lines NCI-H1703, NCI-H2030 (gifts from Dr. Maria Skamagki), and NCI-H2286 (ATCC, Cat# CRL-5938), and human pancreatic cancer cell lines AsPC1 (gift from Dr. Jason Lewis) and NALM6 (gift from Dr. Michel Sadelain) were cultured with RPMI-1640 with fetal bovine serum (FBS) (10%), PenStrep (1%), L-glutamine (1%), sodium pyruvate (1%) and HEPES pH=7.6 (1%). Human ovarian epithelial-mucinous carcinoma cell line COV644 (Sigma-Aldrich Cat# 07071908), human pancreatic cancer cell line MiaPaCa2 (ATCC, Cat# CRL-1420), mouse $Kras^{G12D/+}$;$Trp53^{-/-}$ (KP) lung cancer cells (provided by Dr. T. Jacks and expressing firefly luciferase-GFP [FFluc-GFP] as described[25]) and mouse MYC^{OE};$Trp53^{-/-}$;$Brca1^{-/-}$ (MPB1) ovarian cancer cells (generated by Dr. Stella Paffenholz[58]) were cultured in DME-high glucose with the same supplements. MPB1 cells were cultured on collagen I–coated plates (Fisher Scientific, Cat# 356450). Tyk-nu^{CD19}, cells were generated by lentiviral Human ovarian cancer and CRC organoid were gifts from Dr. Elisa de Stanchina and Dr. Karuna Ganesh, respectively. All FBS was obtained from GeminiBio (Foundation FBS, Cat# 900-108, lot#A122063). All cell lines and organoids (see key reagents table) were periodically tested for mycoplasma (Lonza #LT07-318). All cells and organoids used in vivo experiments were engineered to express FFLuc-GFP, allowing in vivo tracking of tumor burden via luciferase imaging (IVIS).

Mice

General description and housing

All mouse experiments were performed in accordance with protocol 11-06-018 and 04-03-009 approved by MSK's Institutional Animal Care and Use Committee. All relevant animal use guidelines and ethical regulations were followed. Mice were maintained in group housing under specific pathogen-free conditions, and food and water were provided ad libitum. Animals were housed on a 12 hr–12 hr light–dark cycle under standard temperature (around 18–24 °C) and humidity (around 40–60%). The following mice were purchased from The Jackson Laboratory: NOD-scid IL2Rgnull (NSG), and NOD.Cg-KitW-41JTyr+ Prkdcscid Il2rgtm1Wjl/ThomJ (NBSGW, strain# 026622). C57BL/6N mice and athymic nude Crl:NU(NCr)-$Foxn1^{nu}$ mice were purchased from Charles River Laboratories. For ovarian cancer experiments, female mice (8-12 weeks old) were used. For other cancer models, mice of both sexes were used. Mice were 8–12 weeks of age at the time of experimentation, except for xenograft experiments (8–10 weeks) and T cell isolation (6–10). Mice were randomly assigned to experimental groups after baseline tumor burden was quantified.

Xenograft tumor models

NOD/SCID/IL-2Rγ-null (NSG) mice were used at 8-12 weeks of age. In ovarian cancer models, FFLuc-GFP-expressing Tyk-nu cells were injected: $5x10^5$ cells per mouse were injected into the ovarian bursa for orthotopic models and $2x10^6$ cells per mouse injected intraperitoneally for metastatic models. In orthotopic lung cancer models, FFLuc-GFP-expressing cells (NCI-H1703, NCI-H2030, or NCI-H2286; $2x10^5$ cells per mouse) were administered via tail vein injection. In pancreatic cancer models, FFLuc-GFP-expressing AsPC1 cells were injected: $2x10^5$ cells per mouse into the pancreas for orthotopic models and $2x10^6$ per mouse into the subcutaneous space for subcutaneous models. Patient-derived Xenografts (PDX) were maintained and passaged in NSG mice. Patient-derived Organoids (PDO) were maintained in 3D Matrigel as previously described[77] and transplanted to NSG mice for anti-tumor studies. For all solid tumor models, $1\text{-}2x10^6$ untransduced T cells or an equivalent number of CAR-transduced T cells were administrated via intraperitoneal injection 2 weeks after tumor cells injection.

Syngeneic tumor models

C57BL/6N mice (Charles River) were used at 8-12 weeks of age. In orthotopic ovarian cancer models, $5x10^5$ FFLuc-GFP-expressing MPB1 cells per mouse were injected into the ovarian bursa. In metastatic ovarian cancer models, $2x10^6$ FFLuc-GFP-expressing cells per mouse were injected intraperitoneally. In orthotopic lung cancer models, $2x10^5$ FFLuc-GFP-expressing KP cells per mouse were administered via tail vein injection. One week later, $1x10^6$ UTD or CAR-transduced T cells were administrated via intravenous injection.

Monitoring of tumor burden and survival

Tumor burden was measured by bioluminescence imaging using the Xenogen IVIS Imaging System (Xenogen). Living Image software (Xenogen) was used to analyze acquired bioluminescence data. Survival was monitored for a minimum of 150 days post T cell injection. Mice were euthanized when they showed clear clinical signs of distress or when reaching maximum tumor burden as defined by hindlimb paralysis. There were no instances at which this maximum was exceeded. Subcutaneous tumors were monitored through weekly caliper measurements.

Humanized HGSOC xenograft model

Humanized HGSOC-engrafted mice were used under a protocol (11-06-018) approved by the MSK Institutional Animal Care and Use Committee, to evaluate the impact of in vivo activated CAR T cells on normal human hematopoietic cells. CAR T cells were generated from cryopreserved T cells from the same donor where the hematopoietic stem and progenitor cells (HSPCs) were isolated in an autologous setting, using the γ-retroviral T cell transduction protocol as described above. Five days after HSPC thawing (day -63), *in vitro* expanded HSPCs ($5x10^5$ per mouse) were injected via tail vein into female 4-week-old NBSGW mice. Seven weeks after HSPC injection (day -14), FFLuc-GFP and ectopic h.CD19 expressing Tyk-nu^{CD19} HGSOC cells ($1x10^6$ per mouse) were injected intraperitoneally. Nine weeks after HSPC injection (day 0), CAR T cells (h19-h.28z.1XX or h.uPAR-h.28z.1XX, $1x10^6$ per mouse) were injected via tail vein. Antitumor efficacy was monitored via bioluminescence imaging. On day 7, bone marrow aspirates from untreated, h19-h.28z.1XX-treated, or h.uPAR-h.28z.1XX-treated mice were collected and analyzed via flow cytometry. Normal human hematopoietic cell populations were defined as follows: HSPCs (hCD45+CD3-CD19-CD14-CD16-CD34+); B cells (hCD45+CD33-CD19+); granulocytes (hCD45+CD14-CD16+); monocytes (hCD45+CD14+CD16-), CAR T cells (hCD45+CD3+).

Patient samples

Human FFPE TMAs were obtained from TissueArray (#CO2001a, #BR931, #BC000119b, #PR633a, #GL803d) and from tissues samples from patients who were enrolled at Memorial Sloan Kettering (MSK). For all MSK specimens used in this study, all enrolled patients gave consent to an institutional biospecimen banking protocol, and all analyses were performed according to a biospecimen research protocol. All protocols were approved by the MSK institutional review board (IRB: #12-245. 14-091). Patients were asked for consent following the IRB-approved standard operating procedures for informed consent. Written informed consent was obtained from all patients before conducting any study-related procedures. Age and gender information are summarized in Tables S1A and S1B. Tissue samples used for immunofluorescence analysis are summarized in Table S1A.

METHOD DETAILS

CRISPR-Cas9 Gene Targeting

For ribonucleoprotein (RNP)-mediated CRISPR genome editing, Cas9 was incubated with sgRNA (IDT, see sequences below) for 20 min to form the RNP complex before nucleofection. The following components were used per reaction to generate an RNP complex (sgRNA: 200 pmol, rCas9: 61 pmol, Enhancer: 100 pmol). Nucleofection was performed using a Neon Transfection System 10 μL Kit (Thermo Fisher Scientific, Cat# N1096). Tumor cells ($1x10^6$) were washed with phosphate-buffered saline (PBS) and resuspended in nucleofection buffer with RNP complexes and electroporation enhancer (IDT, Cat# 1075915, 1:1 molar ratio to cRNP) in a total volume of 10 μL. The cell suspension was transferred to a nucleofection cuvette and nucleofected using Neon NxT Electroporation System (Thermo Fisher Scientific, Cat# NEON18S). Immediately after nucleofection, cells were directly seeded into culture with complete growth media. Editing outcome was analyzed by flow cytometry within a week.

For off-target hematotoxicity experiments, the TCRα subunit constant gene (*TRAC*) was disrupted in human T cells using RNP-mediated CRISPR genome editing. 48h after initiating T cell activation (see generation of murine uPAR CAR T cells section, below),

the CD3/CD28 beads were magnetically removed, and T cells were transfected by electrotransfer of TRAC RNP using a Lonza Amaxa Nucleofector II. Then, $10x10^6$ cells were resuspended in P3 buffer (Lonza) and mixed with 300 pmol TRAC in a total volume of 100 μl, respectively. Following electroporation and assuming 66.7% recovery rate, cells were diluted and incubated in culture medium at $1x10^6$ cells/ml. At 12 to 24h post electroporation, T cells were transduced via CAR-expressing SFG-γ-retroviral vector following the transduction protocol as described for non-edited T cells. Subsequently, TRAC-edited and SFG γ-retrovirally-transduced T cells were cultured using T cell growth medium, replenished at least every two days and as needed to maintain a density of 1–$1.5x10^6$ cells/ml.

sgRNA sequences against h.uPAR or m.uPAR were selected from IDT pre-designed tool and sequence was provided in the key resources table. The sgRNA sequence against *TRAC* has been described and was provided in the key resources table.[60] *TRAC* gRNAs were ordered from Synthego with 2′-O-methyl 3′-phosphorothioate modifications in the first and last three nucleotides.[59] Guide RNA was resuspended with TE buffer at 40 μM. Cas9 protein (40 μM) was obtained from QB3-Berkeley Macrolab core facility. *TRAC* RNP was prepared by mixing Cas9 protein and *TRAC* gRNA at 1:1 molar ratio, incubating at 37°C for 15 min, and immediately using it for T cell editing experiments.

Normal HSPC collection and in vitro culture

Leukapheresis material from G-CSF-mobilized adult healthy donors (n=2; STEMCELL Technologies) was used to isolate $CD34^{pos}$ cells via CliniMACS CD34 GMP MicroBeads (Miltenyi Biotec) and a CliniMACS device (Miltenyi Biotec). T cells from the $CD34^{neg}$ fraction were isolated using a Pan T Cell Isolation Kit (STEMCELL Technologies). Matched donor $CD34^{pos}$ HSPCs and $CD34^{neg}$ pan T cells were separately cryopreserved in CryoStor CS10 freezing medium (Stemcell Technologies). HSPCs were thawed using thawing buffer (X-vivo 15, 1% human serum albumin, 10 U/ml heparin) and subsequently cultured in HSPC cytokine-rich medium (StemSpan SFEM II (Stemcell Technologies), SCF 100 ng/ml (R&D Systems), thrombopoietin 100 ng/ml (Stemcell Technologies), FLT3L 100 ng/ml (R&D Systems), IL6 100 ng/ml (Peprotech), UM729 0.5 μM (Stemcell Technologies), SR1 0.75 μM (Cellagen Technology), streptomycin 20 mg/ml, penicillin 20 U/ml) under hypoxic conditions (2% O_2), at 37°C and 5% CO_2, maintaining a cell concentration of $0.5x10^6$/ml.[59] In vitro expanded human HSPCs were used to generate humanized HGSOC xenograft model (see above).

Antibody Conjugation for PET-imaging

Murine-specific uPAR antibody (R&D Systems, Cat# MAB531) was radiolabeled with zirconium-89 as described previously.[86] Human-specific uPAR clones were developed as deferoxamine (DFO) containing immunoPET agents with zirconium-89 using SCN-Bz-DFO (Macrocyclics, Cat# B705) as described previously[87] targeting a 6:1 molar ratio (DFO:antibody). MALDI-TOF showed that the degree of labeling for T1, A1, and A3 clones was 0.5, 0.2 and 1.1 DFO chelates per antibody, respectively. Radiolabeling of clones was successful at an apparent specific activity of 0.55 MBq/μg antibody with a radiochemical purity exceeding 99%. Stability studies in human serum confirmed radioimmunoconjugates to be stable through 144-hours with >96% zirconium-89 bound, with clones T1 and A1 >99% zirconium-89 bound. To limit nonspecific uptake of the human clones in NSG mice, human uPAR antibodies were co-injected with 250 μg isotype IgG_1 (BioXCell, Cat# BE0297) for initial clone imaging in Tyk-nu orthotopically implanted mice. Subsequent studies in NSG mice were injected with a deglycosylated human uPAR clone T1 or A1 without any IgG_1 supplementation. Deglycosylation was achieved using the Remove-iT PNGaseF (New England Bio, Cat# P0706S) as recommended by the manufacturer with 1-5 μL per 10-20 μg antibody overnight at 37° C, with subsequent removal of enzyme via chitin magnetic beads (New England Bio, Cat# E8036). Deglycosylation was confirmed by native SDS-PAGE gel shift for each DFO-conjugated uPAR clone.

ImmunoPET imaging

To monitor tumor progression, two implantation models were used: orthotopic tumors established via ovary bursa injection, and metastatic tumors established via intraperitoneal injection. Tumor-bearing mice were injected with 20 μg uPAR antibody radiolabeled with zirconium-89 (^{89}Zr) to an apparent specific activity of 0.55 MBq/μg antibody with radiochemical conversion exceeding 99%. Imaging was performed at 24, 72, and 144 hours post-injection on a Siemens Inveon PET/CT with a custom printed 4 position mouse hotel capturing 40 million coincidences per mouse per timepoint. Images were cropped and calibrated to represent percent injected activity per cubic centimeter (%IA/CC). After 144 hours, tissues were collected for 20-μm sectioning and autoradiography with a Bea-Quant.[86,87] To monitor treatment response and tumor remission following CAR T cell therapy, mice were orthotopically implanted with Tyk-nu tumors and, upon tumor establishment, treated with 1 $x10^6$ h.uPAR CAR T cells (T1 or A1) via intraperitoneal injection. Radiotracer and CAR binders were cross-paired to limit epitope competition during therapy monitoring. Three doses of copper-64 (^{64}Cu) were given a week apart at 0 week (baseline), 1 week and 2 weeks post CAR T cell administration. For antibody labeling, Sar-Tz was first radiolabeled with ^{64}Cu in 0.25 M ammonium acetate pH 5.5 for 30 min at 37C, targeting 11.1 MBq/nmol with >99% radiochemical conversion. Pre-targeting was achieved injecting 1 nmol [^{64}Cu]Cu-Sar-Tz at 24 hours after first injection of TCO-A only. PET imaging was done 24hr after [^{64}Cu]Cu-Sar-Tz administration.

Affinity measurement and uPAR domain binding studies

Affinity measurement of h.uPAR scFv T1 and A1 was conducted by Abzena using Biacore T200 (serial no. 1909913). Both T1 and A1 were cloned into human IgGk backbone and full-length antibodies were purified by affinity chromatography. Recombinant h.uPAR protein was immobilized and antibodies was diluted to 1μg/mL in running buffer, captured to ~170 RU at 10 μl/min, followed by a

2-fold dilution series from 0.39 nM to 200 nM. Regeneration was done in 10 mM Glycine-HL, pH1.5. A 1:1 fitting model with double reference subtraction was used for the analysis. Sensorgrams were generated using Biacore T200 Evaluation Software.

Domain binding studies of T1 and A1 human uPAR binders were performed based on the previously optimized method for radioligand binding with histidine tag–functionalized magnetic beads,[87] human uPAR (residues 23-303, UPR-H5226) and domain fragments consisting of domains 2-3 (residues 112-303, UPR-H52H4) and domain 3 (residues 209-303, UPR-H52H6) were added to beads in excess. Next, 1 ng of each radiolabeled clone was added to test domain-binding specificity with a 5-μg block with N=4 technical replicates per condition. All four radiolabeled uPAR clones were prepared as described in ImmunoPET imaging, and beads were incubated with radioimmunoconjugate for 30 min before washing and gamma counting to determine percent activity bound.

Quantitative PCR with reverse transcription

Total RNA was isolated using the RNeasy Mini Kit (Qiagen), and cDNA was obtained using TaqMan reverse-transcription reagents (Applied Biosystems). Quantitative PCR (qPCR) was performed in triplicate using SYBR green PCR master mix (Applied Biosystems) on the QuantStudio 6 Real-Time PCR System (Thermo Fisher Scientific). Ribosomal Protein Lateral Stalk Subunit P0 (*RPLPO*) served as an endogenous normalization control for mouse and human samples.

Histological analysis, immunohistochemistry, and immunofluorescence

Throughout, we use "multi-IF" for small-panel IF (4–6 markers) and "hyperplex IF" for large-panel IF (≥20 markers). Pan-cancer analysis of human tissues (Figures 1A and 1B) was performed by IF on FFPE TMAs of lung cancer (including LUAD, LUSC, and LCNEC), PDAC, bladder cancer, and sarcomas (including undifferentiated pleomorphic sarcoma [UPS] and myxofibrosarcoma [MFS]), generated with 2 to 3 cores[72] per patients at the MSK Pathology Core Lab, Precision Pathology Biobanking Center (PPBC). Staining and analysis were conducted on these TMAs, whereas staining of human HGSOC, CCA, and mesothelioma was performed on whole tissue sections from patient samples collected at MSK. Additional FFPE TMAs including tumor types and patients cases of brain, colorectal, breast, prostate, lung and pancreatic tumors, as well as normal tissues were obtained from TissueArray. Mouse tissues were fixed overnight in 10% formalin and embedded in paraffin, and FFPE blocks were cut into 5-μm sections. Sections were subjected to hematoxylin and eosin (H&E) staining and/or immunohistochemical (IHC) and/or immunofluorescence (IF) staining. IHC and IF were performed following standard protocols: tissues sections were deparaffinized and rehydrated, followed by antigen retrieval using either a double pH protocol (pH 6 and pH 9) or a single pH 6 retrieval. Next, slides were blocked with PBS containing 3% bovine serum albumin (BSA) and incubated with primary antibodies followed when necessary, with appropriate secondary antibodies.

Whole human and mouse tissues sections as well as human prostate (TissueArray, Cat# PR633a) and breast (TissueArray, Cat# BR931) cancer TMAs were scanned on a Pannoramic Scanner (3DHistech, Budapest, Hungary) using a 20x/0.8NA objective at MSK's Molecular Cytology Core. Other TMAs were imaged using the CellDive (Leica), for which background autofluorescence was acquired before staining and removed prior to analysis (see below). uPAR quantification in tumor cells and stromal cells in Figures 1A and S2B was performed as followed: regions of interest around the tissues were then drawn and exported as.tif files from these scans using Case Viewer (3DHistech, Hungary.) These images were then analyzed using ImageJ/FIJI (NIH, USA.) Thresholding was used to determine the area of the tissue in DAPI and each marker. Then the DAPI was segmented by creating a mask and watershedding the nuclei. An ROI was created to approximate each cell and the percent area of each marker was used to determine positivity. Tumor cells were defined as PanCK+ (carcinomas), MSLN+ (mesothelioma), CD45−αSMA− (sarcomas), or CD45−αSMA−CD31− (brain tumors), with stroma as the complementary gate. Figure 1A shows, for each cancer type, the percentage of patients stratified by the fraction of uPAR+ tumor cells among all tumor cells: High (>50%), Intermediate (30–50%), Low (5–30%), Negative (<5%); Figure S2A plots, the percentage of tumor cells that are uPAR+ per patient or per tumor sample as indicated.

The Double Immunohistochemistry staining of CD3 and GFP is done using Ventana-Roche's Ultra platform. After 48 min of heat and CC1 (Cell Conditioning 1) (Ventana, Cat# 950-500) retrieval, a rabbit polyclonal CD3 antibody, (DAKO, Cat# A0452) was used in 1.2 ug/mL concentration. The incubation with the primary antibody was done for 4 h followed by 20 min of Omni Map anti-Rb HRP (Ventana, Cat# 760-4311) followed by Red HRP kit (Ventana, Cat# 760-260) were used for 12 min. A rabbit monoclonal anti-GFP antibody (Cell Signaling, Cat# 2956) was used in 0.035 ug/mL concentration. The incubation with the primary antibody was done for 4 hours followed by 20 minutes Omni Map anti-Rb HRP followed by Green HRP kit (Ventana, Cat#760-271) were used for 16 minutes. The slides were counterstained with hematoxylin and coverslipped with Permount (Fisher Scientific).

Hyperplex IF imaging and analysis

Hyperplex-IF experiments were performed on 5-μm FFPE sections using the CellDive instrument (Leica), an iterative staining platform that employs an imaging and dye inactivation workflow, following the manufacturer's protocol. Briefly, after a 2-step antigen retrieval process, slides were blocked with 3% BSA, stained with DAPI, and imaged unstained to acquire background autofluorescence. Samples were then sequentially stained with antibodies and imaged using DAPI, Cy3, Cy5, and FITC channels on the CellDive instrument with CellDive image acquisition and processing software. Each field of view (FOV) was imaged in each staining round, followed by autofluorescence removal, registration with baseline DAPI, and stitching. Unconjugated primary antibodies were used in the first round of staining, followed by secondary antibody staining. After imaging, dye inactivation was performed using 0.1 M Na_2CO_3 3% H_2O_2 solution for 15 minutes at RT before starting the next round of autofluorescence imaging and staining, for a total of 24 markers (see Table S3A for antibodies stained). BSA Azide free FAP antibody was conjugated in house according to the manufacturer's

protocol, using Alexa Fluor 750 NHS Ester (succinimidyl ester) (Invitrogen, Cat# A20111) and Zeba Spin Desalting Columns 7K MWCO, 0.5mL (ThermoFisher, Cat# 89882). All rounds of imaging and slide storage were done in a solution of PBS with 50% glycerol. Staining quality and fluorescence removal were verified after each round. The fully stitched images were imported into HALO image analysis software (Indica Labs) for analysis. Cell segmentation was performed using the ''traditional'' nuclear segmentation option, with analysis settings optimized for each staining category. Phenotypic classifications were created to define cell populations (see Table S3B for details). A limited number of cores or areas were excluded from the analysis due to poor tissue quality, antibody aggregates, tissue folds or absence of tissue. Each patient's data represents the average cell count across single, duplicate or triplicate tissue cores. After image processing, data were analyzed and visualized using GraphPad Prism.

Sirius Red staining

Fibrosis analysis on mouse tissue was performed using Sirius red staining to detect collagen fibers. Sirius red staining was performed on 5um-thickness FFPE sections following Dr. Xin Chen's protocol (UCSF, https://pharm.ucsf.edu/xinchen/protocols/picrosirius-red). Tissue sections were heated for 45 mins at 60°C followed by deparaffinization and hydration. Picro-sirius red solution as made from 0.1% Direct Red 80 (Sigma-Aldrich, Cat# 365548), 0.1% Fast Green (Sigma-Aldrich, Cat# F7252), and 1.2% Picric acid FCF (Sigma-Aldrich, Cat# 197378) dissolved in ddH20. Tissues were incubated with picro-sirius red solution for 60 minutes at room temperature before rehydration and mounting. Slides were scanned with Pannoramic P250 Flash scanner (3DHistech, Hungary) using 20x/0.8NA objective lens, and the percent of Sirius red staining area was quantified by Fiji.

Flow cytometry

For analysis of uPAR expression in cell lines after induction of senescence, KP cells were treated with trametinib (25 nM) and palbociclib (500 nM) or with vehicle (DMSO), and human primary melanocytes were continuously passaged for 15 passages and then trypsinized, resuspended in PBS supplemented with 2% FBS and stained with the following antibodies for 30 min on ice. Detailed antibody information can be found in key resource table. For cell counting, CountBright Absolute Counting Beads were added (Invitrogen) according to the manufacturer's instructions. For in vivo experiments, Fc receptors were blocked using FcR blocking reagent, mouse (Miltenyi Biotec). For intracellular cytokine staining assay, cells were fixed and permeabilized using the Cytofix/Cytoperm Fixation/Permeabilization Solution Kit (BD Biosciences, Cat# 554714) or Intracellular Fixation & Permeabilization Buffer Set Kit (eBioscience, Cat# 88-8824-00) according to the manufacturer's instructions. Flow cytometry was performed on a LSRFortessa instrument (BD Biosciences) or Cytek Aurora (CYTEK) and data were analyzed using FlowJo (TreeStar).

Antigen density quantification

In order to determine the number of uPAR molecules per cells, individual cancer cell lines ($1 – 2 \times 10^6$) were dissociated with EDTA (2mM) containing PBS, stained with anti-h.uPAR (T1) antibody (this paper, 1:200), followed by phycoerythrin (PE)-anti-human Fc secondary antibody (Invitrogen, Cat #12-4998-82, 1:1000) in MACS buffer for 30 min at 4°C, washed and analyzed by FACS. Phycoerythrin Fluorescence Quantitation Kit (BD Biosciences, Cat# 340495) was used according to the manufacturer's protocol.

Generation of murine uPAR CAR T cells

Mouse SFG γ-retroviral m.uPAR plasmids were previously described[25] m.uPAR-targeting CAR T cells were generated by γ-retroviral transduction of anti-uPAR scFv linked to CD28 costimulatory and CD3ζ signaling domains (m.uPAR-m.28z). In this construct, a mouse CD8a signal peptide is followed by the anti-mouse uPAR scFv, then by the MYC-tag sequence, a mouse CD28 transmembrane domain, and a mouse CD3z intracellular domain[88] (Kuhn et al.). Plasmids encoding the SFG γ-retroviral vectors were used to transfect gpg29 fibroblasts (H29) to generate VSV-G pseudotyped retroviral supernatants, which were used to construct stable retrovirus-producing cell lines as previously described.[88,89] To isolate mouse T cells from peripheral blood, C57BL/6 mice were euthanized and spleens were collected. After tissue dissection and red blood cell lysis, primary mouse T cells were purified using the mouse Pan T cell Isolation Kit (Miltenyi Biotec Cat# 130-095-130). Purified T cells were cultured in RPMI-1640 (Fisher Scientific, Cat# 11-875-119) supplemented with 10% FBS (GeminiBio, Cat# 900-108), 10 mM HEPES (Fisher Scientific, Cat# 15-630-080), 2 mM l-glutamine (Thermo Scientific, Cat# A2916801), MEM non-essential amino acids (Thermo Fisher Scientific, Cat# 11140050), 55 μM β-mercaptoethanol (Thermo Scientific, Cat# A2916801), 1 mM sodium pyruvate (Thermo Scientific, Cat# 11360070), 100 IU/ml recombinant human IL-2 (Proleukin; Novartis), and mouse anti-CD3/28 Dynabeads (Gibco, Cat# 11453D) at a bead:cell ratio of 1:2. T cells were spinoculated with retroviral supernatant collected from Phoenix-ECO cells 24 h after initial T cell activation as described[88,90] and used for functional analysis 3–4 days later.

Generation of human uPAR CAR T cells

Human SFG γ-retroviral m.uPAR-h.28z plasmids were previously described.[25] h.uPAR-h.28z plasmids were generated in this manuscript. In the human uPAR-h.28z CAR, the anti-human uPAR scFv is preceded by a signal peptide sequence that was optimized for each scFv based on its antibody Ig class. The scFv is followed by a CD28 hinge-transmembrane-intracellular domain and a CD3z intracellular signaling domain, and the coding sequence is linked via a P2A sequence to a truncated LNGFR to allow it to be simultaneously expressed. The 1.XX CAR was generated as previously described.[50] Plasmids encoding the SFG γ-retroviral vectors were used to transfect gpg29 fibroblasts (H29) to generate VSV-G pseudotyped retroviral supernatants, which were used to construct

stable retrovirus-producing cell lines as previously described.[88,89] To isolate human T cells from peripheral blood, buffy coats from anonymous healthy donors were purchased from the New York Blood Center. Peripheral blood mononuclear cells were isolated by Ficoll-based density gradient centrifugation. T cells were purified using the human Pan T cell isolation kit (Miltenyi Biotec, Cat# 130-096-535), stimulated with CD3/CD28 T cell activator Dynabeads (Invitrogen, Cat# 11131D) as described,[50] and cultured in X-VIVO 15 (Lonza, Cat# 02-053Q) supplemented with 5% human serum (Gemini Bio-Products, Cat# 100-110-100), 5 ng/ml interleukin-7 (PeproTech, Cat# 200-07-10UG) and 5 ng/ml interleukin-15 (PeproTech, Cat# 200-15-10UG). T cells were counted using an automated cell counter Vi-CELL BLU (Beckman). Forty-eight hours after initiating T cell activation, T cells were transduced with retroviral supernatants by centrifugation on RetroNectin-coated plates (Takara, Cat# T110A). Transduction efficiencies were determined four days later by flow cytometry, and CAR T cells were adoptively transferred into mice or used for in vitro experiments. All in vitro experiments were repeated with at least 3 independent donors. All in vivo experiments were repeated with at least 2 independent donors. All blood samples were handled following the required ethical and safety procedures.

Luciferase-based in vitro cytotoxicity and viability assays

The cytotoxicity of CAR T cells was determined by standard luciferase-based assays. Specifically, target cells expressing firefly luciferase (FFLuc-GFP) were co-cultured with T cells in triplicate at the indicated effector:target ratios using white-walled 96-well plates with 5,000 target cells in a total volume of 100 μl per well in RPMI (human tumor cells) or DMEM (murine tumor cells) medium, respectively. Target cells alone were plated at the same cell density to determine the maximum luciferase expression (relative light units [RLU]), and maximum release was determined by addition of 0.2% Triton-X100 (Sigma). Eighteen hours later, 100 μl luciferase substrate (Bright-Glo, Promega) was directly added to each well. Emitted light was detected in a luminescence plate reader. Lysis was determined as $(1-(\text{RLUsample})/(\text{RLUmax})) \times 100$. Cisplatin was used at 1μM. Irinotecan was used at 1μM. Irradiation was performed at 16-18Gy, depending on cell lines. Cells were analyzed 7 days post senescence induction treatment. For *ex vivo* experiments, two patient-derived organoid lines were cultured in HISC media and treated with irinotecan (250 nM) for 7 days. In cytotoxicity assays with MPB1 cells that required longer incubation (>24 hr), the IncuCyte Live-Cell Analysis System (Sartorius) was used. 50,000 MPB1-GFP cells were seeded into each well of collagen I coated 6-well plate a night before cisplatin (1μM) or vehicle treatment. At 72h after cisplatin treatment, the number of tumor cells was determined by hand-counting in a duplicate plate, and control or CAR T cells were added to each condition at 1:1 ratio. A set of 24 images at randomly selected areas within each well were taken every 2 hours for 72h. Baseline images were taken right before adding T cells. Tumor cell number was quantified by GFP+ area in each well.

Flow Cytometry–Based In Vitro Cytotoxicity and Viability Assays

Cancer-Associated Fibroblast (CAF) Killing Assay

Primary CAFs were isolated from HGSOC (n=4) and CRC (n=2) patients. Isolation of CAFs from patient samples was performed as described before.[91] For patient-derived CAFs, human tissue acquisition and usage was conducted under approved IRB protocol numbers: 12-245 and 14-091. Specifically, tumors are minced and dissociated in RPMI-1640 with FBS (10%), PenStrep (1%), L-glutamine (1%), sodium pyruvate (1%) and HEPES pH=7.6 (1%) plus 0.5% collagenase Type I, 305U/mg (Worthington, Cat# LS004197) for 1 h at 37 C in a thermo-shaker. The digested tumor-cell mixture was filtered through a 100 mm filter (Corning, Cat# 352360) and then spun down at 400g for 1.5 min. Depending on the pellet size, the pellet containing mixture of cells were plated on either a 6-well plate or a 10-cm dish that allows fibroblasts to attach and grow. After 2-3 passages, a limited dilution protocol was performed and cells were plated in a high dilution in a 96-well plate, single clones were expanded later. Validation of fibroblast identity was performed at the protein level by flow cytometry analysis for fibroblast surface markers. CAF killing was assessed by co-culturing target cells with CAR T cells at the indicated effector-to-target (E:T) ratios. Briefly, $0.5–1 \times 10^6$ target cells were plated per well in 6-well plates in 1.5 mL XVIVO-15 medium (Lonza). Target-only control wells were included at matched densities to establish baseline marker expression. After overnight co-culture, cells were harvested using 2 mM EDTA in PBS, washed, and analyzed by flow cytometry to quantify residual viable CAF populations.

M2 Macrophage Killing Assay

Monocyte Isolation: Human monocytes were isolated from healthy donor (n=2)-derived PBMCs using the EasySep™ Human Monocyte Enrichment Kit without CD16 Depletion (StemCell Technologies) following the manufacturer's instructions. Monocyte purity was assessed by flow cytometry before and after isolation. Differentiation of Monocytes into M2a Macrophages: Isolated monocytes were plated at 1×10^6 cells/mL in 10-cm dishes and cultured at 37°C in IMDM supplemented with 20% FBS and 1% penicillin–streptomycin. M2a differentiation was performed according to the manufacturer's protocol (StemCell Technologies). Cultures were supplemented with M-CSF (50 ng/mL; PeproTech) on day 0. On day 3, an additional half-volume of the original medium was added. IL-4 (10 ng/mL; PeproTech) was added on day 4 to induce M2 polarization, and cells were incubated for an additional 48 hr. Co-culture With CAR T Cells. On day 6, differentiated M2a macrophages were harvested by incubation with 2.5 mM EDTA in PBS. Macrophages were co-cultured with CAR T cells in 6-well plates at the indicated E:T ratios, using 1×10^6 target cells per well in 1.5 mL X-Vivo medium. Target-only controls were included to quantify baseline marker expression. After overnight incubation, co-cultures were harvested and analyzed by flow cytometry.

Patient Tumor Cell Killing Assay

Preparation of Single-Cell Suspensions. Fresh human tumor specimens were dissociated using the Tumor Dissociation Kit, Human (Miltenyi Biotec, Cat# 130-095-929) following the manufacturer's recommendations with additional optimization steps described

below. Briefly, tumor samples were first washed twice with cold PBS containing penicillin–streptomycin (PBS/P+S), and necrotic or non-tumor tissue was carefully removed using sterile scissors. Remaining viable tissue was minced with a sterile scalpel into 1–2 mm^3 fragments and transferred into the provided C Tubes containing 7 mL serum-free RPMI. Enzyme Mix components H, R, and A (from the Miltenyi kit) were added at the recommended volumes, and samples were dissociated using the gentleMACS™ or Octo Dissociator with heating (37 °C) for 15–60 min, depending on tissue density and sample size. After enzymatic digestion, samples were diluted with cold FACS buffer to terminate the reaction, passed through a 40–70 μm cell strainer, and centrifuged at 350 × g for 5 min at 4 °C. Cell pellets were washed once with cold PBS; RBC lysis (BioLegend) was performed when necessary. Final cell suspensions were resuspended in cold PBS with 2% FBS, and viable single-cell numbers were quantified using trypan blue exclusion or a Vi-CELL analyzer. The resulting single-cell suspensions were used immediately for co-culture assays or flow cytometry. Co-culture with CAR T Cells: Dissociated patient tumor cells were plated at 0.5–1 × 10^6 cells per well in 6-well plates and co-cultured with CAR T cells at the indicated E:T ratios in 1.5 mL X-Vivo medium. Target-only wells were included as baseline controls. After overnight incubation, co-cultures were collected using 2 mM EDTA in PBS and analyzed by multiparameter flow cytometry to quantify viable tumor and stromal subsets. Surgically removed tumor tissues were obtained from HGSOC (n=4) and LUAD (n=1) patients.

Cytokine and suPAR measurements

Serum cytokines were measured using cytometric bead arrays (BD) as per the manufacturer's instructions. suPAR levels from cell culture supernatant, mouse plasma or human serum and ascites were evaluated by enzyme-linked immunosorbent assay (ELISA) according to the manufacturer's protocol (R&D systems, Cat# DY531 [mouse] or Cat# DY807 [human]).

EPO-GEMMs

Our autochthonous EPO-GEMM was previously published.[58] In short, 8- to 12-week-old female mice were anesthetized with isoflurane. After aseptic skin preparation with povidone-iodine scrub (Betadine) and 70% alcohol, the left oviduct was exteriorized. A mixture of MYC transposon plasmids, SB13 transposase, and sgRNA Trp53 with or without sgRNA Brca1 was injected using a 30-gauge syringe under the ovarian bursa leading to the formation of a round, liquid-containing bubble. Tweezer electrodes were positioned around this bubble and electroporation was performed using NEPAGENE NEPA21 type II electroporator: 2 poring pulses of electrical current (50 V, 30-ms lengths at 450-ms intervals), followed by five transfer pulses (60 V, 50-ms lengths at 450-ms intervals). After electroporation, the peritoneal cavity was rinsed with prewarmed saline solution, and the peritoneum was sutured. The skin was closed with staples and mice were maintained at 37°C until fully awake. Buprenorphine was administrated for 3 days for postoperative analgesia. Tumor formation was assessed by abdominal palpation and ultrasound imaging. Mice were euthanized at the humane endpoint and tumors were harvested. Additional histopathological, genomics and transcriptomics analysis of this model was previously published.[58]

Associations of *PLAUR* expression with oncogenic genetic alterations

To expand the dataset for analyzing associations of genetic alterations with *PLAUR* expression, we downloaded SNP, copy number alteration (CNA), and normalized TPM count data from cBioPortal.[92–94] Patients were classified into five CNA groups based on predefined thresholds: Deep Deletion (<-1), Heterozygous Deletion (<-0.1), Normal (-0.1 to 0.1), Gain (>0.1), and Amplification (>0.9). To simplify the summary plot, tumor suppressor genes were grouped as "Mut + DEL," while oncogenes were categorized as "Mut + AMP." Statistical significance of differences in *PLAUR* expression between altered and wild-type (WT) groups was evaluated using the Wilcoxon test. Results were visualized in a dot plot, where dot size represents the p-value and color represents the log2 fold change.

Associations of *PLAUR* expression with transcriptional signatures

Differential PLAUR expression between tumor and normal

Differential expression analysis was conducted to compare tumor (TCGA) and normal tissue (GTEx) across multiple cancer types using data retrieved from the GEPIA2 web platform. Boxplots were generated to visualize expression differences for PLAUR and selected surface markers, where each point represents a cancer type, and the mean log_2 fold change is highlighted in bold black for comparative analysis.

Gene set enrichment analysis (GSEA)

GSEA (version 2.07) was performed across 19 cancer types using the GSEA Preranked tool to assess signature enrichment between patients with *PLAUR* high and *PLAUR* low tumors using the TCGA database (Figure 1C). *PLAUR* expression tertiles were used to define patient groups, comparing the highest tertile (*PLAUR* high) against the lowest tertile (*PLAUR* low). Analyses were conducted against signatures in the MSigDB database (https://www.gsea-msigdb.org/gsea/index.jsp), signatures derived from previously published expression signatures in mouse GEMM models[58] and human samples (see Table S4 for signature and publication reference). The rank metric scores were calculated using the sign of the fold change multiplied by the inverse of the p-value (http://software.broadinstitute.org/gsea/msigdb).

Signature score analysis

In order to evaluate the signature score for each tumor type in Figure S1D, we used TCGA gene expression data (RNA-seq RSEM TPM) and clinical annotations obtained from the UCSC Xena platform. Samples were filtered to include only primary tumors across

multiple cancer types. For gene expression stratification, samples were ranked by *PLAUR* expression levels and divided into three equal-sized groups using quantile partitioning (Low, Medium, High). Single-sample gene set enrichment analysis was performed using the singscore method to calculate pathway activity scores for each sample. Custom gene sets were curated including msigDB HALLMARK pathways, KEGG biological processes, Biocarta pathways, and literature-derived signatures for processes such as epithelial-mesenchymal transition (EMT), progenitor, fibrosis, angiogenesis, inflammatory response, and wound healing (see Table S4 for signature and publication reference). Pathway activity differences between expression groups were calculated as the mean difference between high and low expression groups (TotalScoreDif) for each cancer type. Wilcoxon rank-sum tests were used to compare pathway scores between groups, with statistical significance assessed at $p < 0.05$. Results were visualized using dot plots showing pathway activity differences across cancer types, with point size representing absolute difference magnitude and color indicating direction of change.

High-grade serous ovarian cancer (HGSOC) primary tumor samples (n=417) with matched RNA-seq (UCSC Xena Toil-recomputed $\log_2$(TPM+0.001)) and CCNE1 copy-number status (cBioPortal, GISTIC2 thresholded) were selected for analysis. TGF-β pathway activity was quantified for each sample using the rank-based single-sample scoring method in the singscore R package, utilizing a custom TGF-β/SMAD gene set. Samples were stratified into TGF-β-high (top quartile of pathway scores) versus the remainder and combined with binary CCNE1 amplification status to define four biological subgroups. PLAUR (uPAR) expression levels were compared across these groups using Wilcoxon rank-sum tests and visualized with R package ggpubr.

Associations of *PLAUR* expression with clinical outcomes

To evaluate whether high *PLAUR* expression is associated with metastatic disease (Figure S1F), normalized TPM and clinical TCGA data were obtained from the Xena Data Portal. Primary tumor samples were filtered, and metastatic cases were identified using the new_tumor_event_type column. Samples were split into high and low *PLAUR* expression groups based on the median expression level. A contingency table was generated, and Fisher's Exact Test was applied to assess the significance of high uPAR expression in relation to metastasis, yielding a p-value, odds ratio, and 95% confidence interval. Survival data, including overall survival (OS), disease-free survival (DFS), and progression-free survival (PFS), along with TPM-normalized gene expression data, were obtained from the UCSC Xena data portal (https://xenabrowser.net/datapages/?cohort=TCGA%20Pan-Cancer%20(PANCAN)&removeHub=https://xena.treehouse.gi.ucsc.edu:443) to generate Figure S1G. TPM values below -1 were excluded from downstream analysis. To evaluate the prognostic significance of *PLAUR*, Kaplan-Meier survival curves were generated using the *survminer* R package, comparing survival outcomes between high and low expression groups stratified by median *PLAUR* expression levels. Statistical significance was assessed using the log-rank test, with p-values < 0.05 considered significant. The coxph function was used to fit the Cox proportional hazards model, with gene expression as the primary variable and race and age included as covariates to account for potential confounders. Hazard ratios (HR) and 95% confidence intervals (CI) were calculated and visualized to determine the association between *PLAUR* expression and survival outcomes.

Generation of Senescence-Cancer Overlap Gene Signature (SenCan)

Senescence Gene Expression Dataset Compilation

To identify genes consistently upregulated during cellular senescence, we compiled transcriptomic data from eight independent senescence induction experiments. Datasets were generated in-house using cell lines subjected to different senescence triggers: (1) oncogene-induced senescence, (2) p53 pathway restoration, and (3) pharmacological treatment-induced senescence. Differential gene expression analysis was performed using DESeq2. In total, 896 genes were identified as significantly upregulated using adjusted p-value < 0.05 and minimum log2FoldChange > log2(1.5) (equivalent to 1.5-fold upregulation).

Cancer Gene Expression

Analysis. Cancer-associated gene expression data were obtained from the UCSC Xena platform, incorporating TCGA (The Cancer Genome Atlas) tumor samples compared against corresponding normal tissue controls from GTEx (Genotype-Tissue Expression) database. This analysis encompassed 16 distinct cancer types, enabling comprehensive pan-cancer gene expression profiling. Differential gene expression analysis between cancer and normal tissues was downloaded directly from GEPIA2 website using ANOVA methods and significantly upregulated genes were identified using statistical criteria: adjusted p-value < 0.05 and minimum log2 fold change > log2(1.5) (equivalent to 1.5-fold upregulation).

Gene Signature Generation

The final SeneUP_ovlp_TCGAvsGTExUP.minpct0.4 signature (SenCan, Table S4A) comprising 85 genes was generated by identifying the intersection of genes that were (1) consistently upregulated across senescence conditions: identified in more than 40% of the senescent data and (2) broadly upregulated across multiple cancer types: identified in more than 40% of all 16 cancer types.

Spatial transcriptomics

Spatial transcriptomics was performed via *in situ* hybridization targeting 477 genes was performed using the Xenium platform (10x Genomics) (Figures 2A–2F and S2A–S2E). FFPE tissue sections from treatment-naïve human pancreas were cut at 5 μm thickness and mounted onto Xenium slides. After deparaffinization and decrosslinking, we performed probe hybridization, ligation, and amplification according to the 10x Genomics Xenium FFPE Tissue Preparation Guide. No sequencing library was constructed. Probes consisted of a pre-designed Xenium probe panel targeting 377 genes (human multi-tissue), along with an additional 100 custom

target genes (Table S2A). Probes were hybridized to RNA in situ, followed by fluorescent labeling, imaging, and decoding using the Xenium Analyzer (v1.7.6.0). Data were processed using the Xenium analysis pipeline (version Xenium-1.7.1.0), which included signal segmentation, transcript decoding, quality score assignment, and spatial mapping of transcripts to x/y coordinates. After Xenium, the same tissue slide was incubated with blocking buffer and used for IF on the CellDive instrument (as described) above. Note that for better staining quality, we also performed hyperplex IF on a serial section of the same sample.

Downstream analysis was performed using Seurat (v5.0.1)[80] throughout the analysis to assess cell types and perform graph-based clustering. Data from Xenium was loaded to a Seurat object using the ''*LoadXenium*'' function. We used the ''Transcripts.csv'' file generated by the Xenium instrument to select transcripts that were in the nucleus, as flagged in the Xenium output, and calculated mean q-value (qv) per cell. We generated the count matrix using nuclear transcripts, and all the downstream analysis were done using those data. Cells with mean qv higher than 25 that had more than 10 transcripts in the nucleus and more than 3 features in total were selected in the quality check process. Gene expression counts were normalized using total count scaling to account for variability in sequencing depth across nuclei. Each cell's counts were scaled by the mean total counts across all cells, ensuring comparability while preserving relative expression levels. After normalization, we followed the Seurat pipeline for finding variable features, scaling, and PCA calculation (https://satijalab.org/seurat/articles/spatial_vignette). Uniform Manifold Approximation and Projection (UMAP) was performed using 30 principal components (PCs) for neighbor identification and clustering. Clusters were identified using a resolution of 0.3, and UMAP embedding was generated using 30 dimensions with default Seurat parameters. The ''*FindAllMarkers*'' function was used to identify different clusters with min.pct= 0.1 and logfc.threshold = 0.25, and then significant results were selected using adjusted p-value < 0.05 (Table S2B). Figures 2A–2D and S2A–S2E were generated using plotting functions DimPlot, DotPlot, ImageDimPlot (from Seurat), and dittoBarPlot (Bioconductor - dittoSeq). The main object was subdivided into fibroblast, PDAC, and immune cell subsets, which were each normalized, scaled, and reclustered to enable more detailed annotation. The refined labels from these subclusters were then projected back onto the main UMAP (Figure S2C).

To determine the senescence score spatially and within specific cell types (Figures 2D and 2E), we filtered the SeneUP_ovlp_TCGAvsGTExUP.minpct0.4 SenCan signature (85 genes), generated as described above, to retain only genes present in the Xenium panel (see the 'SenCan(Xenium)' 11 gene signature in Table S4A) The score was computed using UCell (R package)[95] with maxRank=50, corresponding to the mean number of detected genes per cell in the dataset.

To investigate the spatial relationships between different cell types, each cell was assigned a local neighborhood defined as a 500 $\times$ 500 μm window centered around the cell. Within each neighborhood, the composition of cell types was quantified by calculating the proportion of each cell type: ''(# of cells of a given type) / (total number of cells in the neighborhood)''. This yielded a matrix where each row represented a cell and each column corresponded to the percentage of a specific cell type within that cell's neighborhood. The resulting matrix was used to compute pairwise correlations between cell types using the ''cor'' function from the stats package in R (version 4.3.2; R Core Team, 2023), employing Pearson correlation as the method. Correlations were calculated for all cell types (Figure S3A), and selected subsets of cell types were chosen for visualization in the main figure (Figure 2E). The heatmap was generated using the ggplot2 package.[96] To assess the dominant neighboring cell types around specific PDAC subtypes, we performed permutation analysis using the same neighborhood data generated for the correlation heatmap. For each subtype (basal PDAC and classical PDAC), the following procedure was repeated 10,000 times: In each iteration, 10 random cells of the target subtype were sampled. For each sampled cell, the neighborhood cell type composition was extracted, excluding the celltype itself and unwanted metadata columns. The average percentage of each neighboring cell type was calculated across the 10 cells. The most frequent cell type was recorded for each iteration. Code to reproduce spatial transcriptomic analyses is available at https://github.com/ozcelikelif/uPAR_paper.

Analysis of Bulk RNA-seq datasets

Matched pre/post HGSOC: Bulk RNA-seq data in RPKM (Reads Per Kilobase of transcript per Million mapped reads) format from pre- and post-treatment patient samples were retrieved from a recent neoadjuvant study.[61] Gene signature scores for wound healing, senescence, and fibrosis pathways were calculated using the singscore method, which generates single-sample gene set enrichment scores by ranking genes based on their expression levels and computing signature scores from predefined gene sets. For visualization, signature scores were displayed using boxplots with paired lines connecting pre- and post-treatment samples from the same patients to illustrate individual patient trajectories (Figures 7C, 7D, S12C, and S12D). Statistical significance between pre- and post-treatment groups was assessed using paired-sample Wilcoxon signed-rank tests.

MPB1 cisplatin vs control in mouse: Data was from a previous publication.[58] Bulk RNA-seq data were analyzed by removing adaptor sequences using Trimmomatic. RNA-seq reads were then aligned to GRCm38.91 (mm10) with STAR, and transcript count was quantified using featureCounts to generate raw count matrix. Differential gene expression analysis between cisplatin treated and control mouse samples was performed using the DESeq2 package implemented in R (http://cran.r-project.org/). Gene set enrichment analysis (GSEA) was performed using the GSEAPreranked tool for conducting gene set enrichment analysis against signatures in the MSigDB database and customized signatures. The metric scores were calculated using the sign of the fold change multiplied by the inverse of the p-value.

SENESCopedia: LogCPM (log counts per million) data were downloaded directly from the original Senecopedia paper.[26] Log fold change (logFC) values were calculated by comparing cell lines treated with Alisertib or Etoposide against their respective control samples. Data was visualized using dot plots displaying treatment responses across 9 different cell lines.

Analysis of single cell RNA sequencing data from public datasets

scRNA-seq analysis in NSCLC patients

Processed Seurat objects were obtained from the GitHub repository associated with the original study[78] (https://github.com/czbiohub-sf/scell_lung_adenocarcinoma). Patient metadata for treatment-naïve individuals and those with on-therapy progressive disease (PD) were extracted from the dataset. *PLAUR* expression and uPA/uPAR activity signature scores were computed as the mean expression across single cells. Statistical significance between the two patient groups (n=13 for treatment naïve patients and n=11 for progressive disease from TKI treatment) was assessed using the Wilcoxon rank-sum test.

scRNA-seq analysis in HCC patients

We analyzed scRNA-seq data from 79 HCC patient samples that included treatment-naive hepatocellular carcinoma specimens.[36] From this dataset, we filtered to retain only tumor-derived hepatocyte cells. Data processing included standard Seurat normalization, cell cycle scoring and regression of cell cycle effects and mitochondrial gene percentages. Integration across samples was performed using Harmony through Seurat's IntegrateLayers function. Module scores were calculated using Seurat's "AddModuleScore" function for senescence-associated and progenitor signatures. Analysis was restricted to cells with detectable *PLAUR* expression (PLAUR > 0). Within this population, *PLAUR* levels were classified into tertiles to define high and low expression groups. Statistical significance was assessed using Wilcoxon rank-sum tests, with results visualized through violin and box plots

scRNA-seq analysis in LUAD patients

We analyzed scRNA-seq data from 9 LUAD patient samples that included treatment-naive LUAD specimens.[35] From this dataset, we filtered to retain only the tumor cells. Data processing included standard Seurat normalization, cell cycle scoring and regression of cell cycle effects and mitochondrial gene percentages. Integration across samples was performed using Harmony through Seurat's IntegrateLayers function. Module scores were calculated using Seurat's "AddModuleScore" function for senescence-associated and progenitor signatures. Analysis was restricted to cells with detectable *PLAUR* expression (PLAUR > 0). Within this population, *PLAUR* levels were classified into tertiles to define high and low expression groups. Statistical significance was assessed using Wilcoxon rank-sum tests, with results visualized through violin and box plots.

scRNA-seq analysis in HGSOC patients

Using scRNA-seq of CD45+/- sorted cells from the MSK SPECTRUM cohort, we assigned the main cell types by supervised clustering using CellAssign, as described in the original study.[37] The dataset included 156 untreated HGSOC samples from 41 patients encompassing solid primary and metastatic tumors, and malignant ascites. Data were processed as previously published.[37] Briefly, malignant cell states were identified using Louvain clustering in Seurat. Differential expression was assessed with Seurat's Wilcoxon rank-sum test, filtering for logFC > 0.25 and Benjamini-Hochberg–adjusted $P < 0.05$. Relative enrichment of cell groups in UMAP space (Figure S6G and S6H) was visualized using two-dimensional kernel density estimates with the MASS::kde2d function (grid size=200, bandwidth=0.2). Density maps for two groups were contrasted by subtraction, rescaled, and overlaid on the UMAP to highlight regions of relative enrichment. Module scores were calculated on single cell expression profiles for uPAR-associated gene signatures using Seurat's "*AddModuleScore*" function, including signatures such as uPA/uPAR and plasminogen (Figure S7A). Analysis was restricted to cells with detectable *PLAUR* expression (PLAUR > 0). Within this population, *PLAUR* levels were classified into tertiles to define high and low expression groups. Statistical significance was assessed using Wilcoxon rank-sum tests, with results visualized through violin and box plots

scRNA-seq analysis in PDAC patients

We analyzed scRNA-seq data from 16 PDA samples obtained from treatment-naive patients, including surgical specimens (n=6) and fine-needle biopsy specimens (n=10).[38] From this dataset, we filtered to retain only tumor-derived ductal epithelial cells. Data processing included standard Seurat normalization, cell cycle scoring and regression of cell cycle effects and mitochondrial gene percentages. Integration across samples was performed using Harmony through Seurat's *IntegrateLayers* function. Module scores were calculated using Seurat's "*AddModuleScore*" function for senescence-associated and progenitor signatures. Analysis was restricted to cells with detectable *PLAUR* expression (PLAUR > 0). Within this population, *PLAUR* levels were classified into tertiles to define high and low expression groups. Statistical significance was assessed using Wilcoxon rank-sum tests, with results visualized through violin and box plots.

scRNA-seq analysis in CRC patients and CRC patient-derived organoids

The dataset included 16 untreated colorectal cancer (CRC) tumor samples from 8 patients (8 primary and 8 metastatic) and 43 treated samples from 20 patients (20 primary and 23 metastatic).[77] Detailed data processing is as previously published.[77] Briefly, raw data were processed using the SEQC (v2.7.0) pipeline for alignment and UMI correction, followed by ambient RNA removal with CellBender (v0.1.0). Low-quality cells were filtered using probabilistic thresholds and iterative clustering. Normalized counts were log-transformed, and highly variable genes were selected for PCA. Gene expression was denoised and imputed using MAGIC (v3.0.0) with conservative parameters. All visualizations, including box plots, were generated using the imputed expression layer.

QUANTIFICATION AND STATISTICAL ANALYSIS

Statistical analyses were performed using Prism 10 software (GraphPad Software) as described in the figure legends. p values < 0.05 were considered statistically significant. p values are indicated in some graphs by asterisks: *$p < 0.05$; **$p < 0.01$; ***$p < 0.001$; ****$p < 0.0001$. Statistical significance was determined by Student's t test, one-way ANOVA, log-rank test, Spearman and Pearson's correlation, or Wilcoxon signed-rank test, as indicated in the figure legend. Survival was measured using the Kaplan–Meier method. Error bars indicate SD or SEM as indicated in the figure legend. Unless otherwise stated, the indicated sample size (n) represents biological replicates. All samples that met proper experimental conditions were included in the analysis.

CellPress
OPEN ACCESS

Supplemental figures

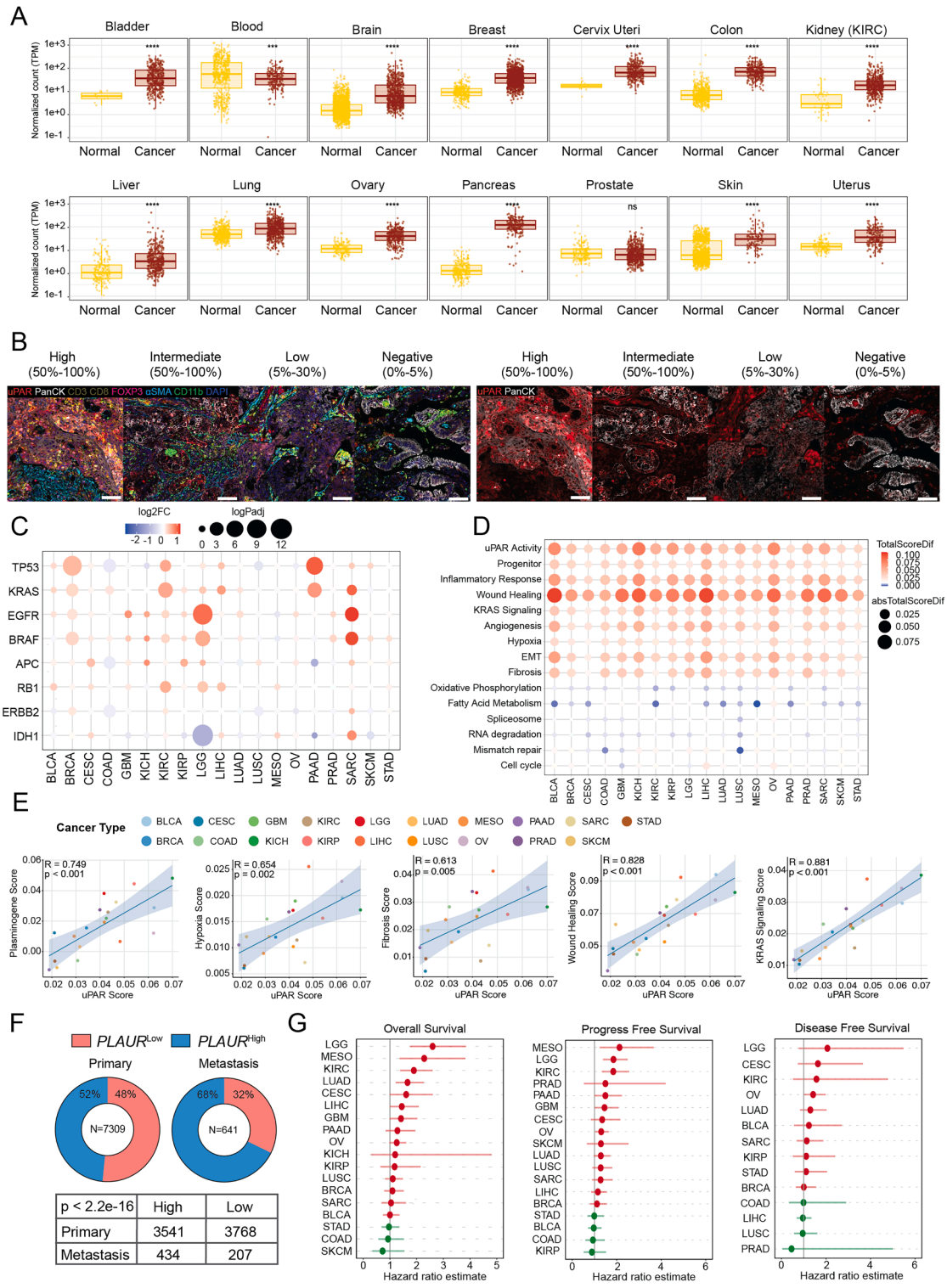

(legend on next page)

Figure S1. Integrated analysis of uPAR-high cancer, related to Figure 1

(A) Boxplots showing uPAR (*PLAUR*) expression in normal and tissues across different cancer types using TCGA and GTEx datasets, and each dot represents one individual.

(B) Representative multi-IF images of NSCLC samples with the indicated uPAR expression levels, showing tumor (PanCK) and microenvironmental markers (CD3/CD8 for T cells, FOXP3 for Treg, CD11b for myeloid cells, and αSMA for fibroblasts) (left), and uPAR co-localization with tumor cells (right); scale bars, 100 μm.

(C) Association of *PLAUR* expression with TP53 and MAPK-pathway alterations. The bubble heatmap shows the extent of *PLAUR* upregulation in cancer types with oncogenic mutations or copy number alterations in the indicated genes.

(D) Bubble heatmap of pathway activity differences between *PLAUR*-high versus *PLAUR*-low tumors within each cancer type. Single-sample signature scores were computed with singscore (see STAR Methods).

(E) Pearson correlation plots showing the relationship between the indicated gene signatures and uPAR activity.

(F) Pie chart and contingency table from TCGA analysis showing the percentage (top) and number of patients (bottom) with high (>66th percentile) or low (<33rd percentile) *PLAUR* expression in primary versus metastatic cancer.

(G) Forest plots showing hazard ratio estimates for overall survival (left), disease-free survival (middle), and progression-free survival (right) between *PLAUR* high (>66th percentile) versus *PLAUR* low (<33rd percentile) tumors. Horizontal lines indicate 95% confidence intervals. Green indicates hazard ratios (HR) > 1, and red indicates HR < 1.

LUAD, lung adenocarcinoma; LUSC, lung squamous cell carcinoma; HGSOC, high-grade serous ovarian cancer; PDAC or PAAD, pancreatic adenocarcinoma; CCA, cholangiocarcinoma; MESO, mesothelioma; CAC, colorectal adenocarcinoma; MAC, mucinous colorectal adenocarcinoma; SAR, sarcoma encompassing UPS and myxofibrosarcomas; BLCA, bladder urothelial carcinoma; BRCA, breast invasive carcinoma; CESC, cervical squamous cell carcinoma and endocervical adenocarcinoma; COAD, colon adenocarcinoma; GBM, glioblastoma multiforme.

Statistical significance was determined using the Wilcoxon test (A) and Student's *t* test (E).

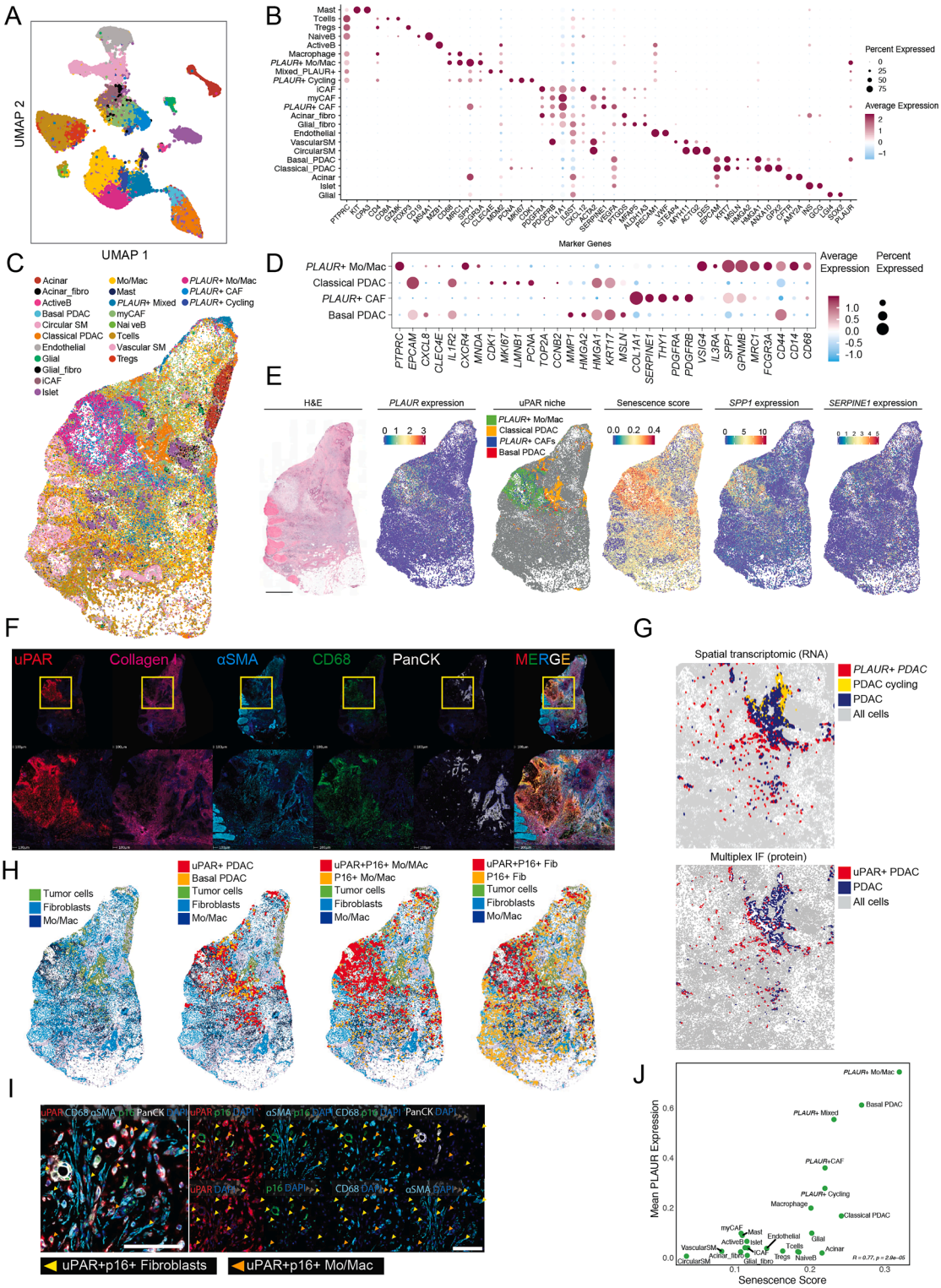

Figure S2. Transcriptomic and spatial molecular characterization of uPAR+ cell populations reveals uPAR+ tumor, myeloid, and CAF co-localization, related to Figure 2

(A) UMAP clustering matching the spatial plot in Data S1.3C, showing distribution of identified cell types. Each dot represents one cell. See panel C for the key to the cell types.

(B) Bubble heatmap showing selected cell type markers for identifying each cell population. Mo/Mac, monocytes and macrophages.

(legend continued on next page)

(C) Spatial plot showing individual cell types.
(D) Bubble heatmap showing genes expressed in selected *PLAUR*+ cell populations (basal and classical PDAC, CAFs, and Mo/Mac).
(E) H&E and spatial plots of the entire tissue matching Figure 2B, showing signature score or single-gene expression.
(F) Multiplex IF (multi-IF) showing the uPAR+ niche at the protein level in the fibrotic region (collagen type 1), enriched in fibroblasts (αSMA), monocytes, or macrophages (CD68). The section analyzed was adjacent to the section used for spatial transcriptomics. PanCK was used to localize tumor cells.
(G) Spatial plots showing similar patterns of uPAR-expressing tumor (PDAC) cells detected as *PLAUR*+ tumor cells using spatial transcriptomics (top) or as uPAR+ tumor cells (PanCK+) using multiplex IF (bottom).
(H) Spatial plots from multi-IF of the entire tissue, matching Figure 2C. Cell types were defined as follows: tumor cells, PanCK+; fibroblasts, αSMA+; monocytes and macrophages (Mo/Mac), CD68+; and basal PDAC cells, KRT17+PanCK+.
(I) Multi-IF showing co-localization of uPAR and p16 in fibroblasts (αSMA+, yellow arrows) and Mo/Mac (CD68+, orange arrows) near tumor cells (PanCK+).
(J) Correlation of *PLAUR* expression and senescence score in individual cell types.

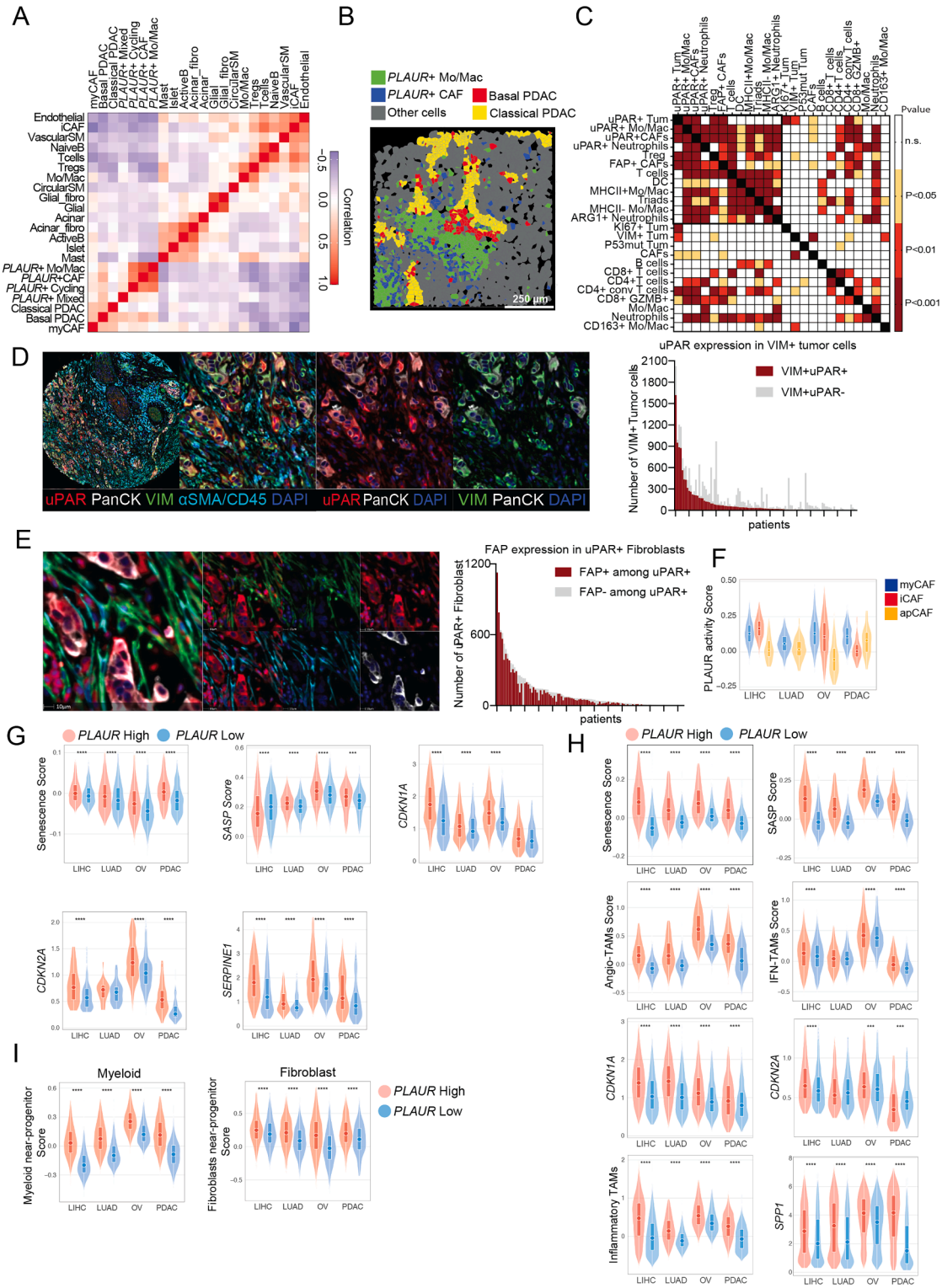

Figure S3. uPAR+ tumor, myeloid, and CAF co-localization in CRC, along with senescence-related programs in *PLAUR*-high cells across cancer types, related to Figure 2

(A) Co-occurrence heatmap showing spatial correlation between cell types.

(B) Spatial cell-type segmentation map, based on spatial transcriptomics (10× xenium), displaying *PLAUR*+ Mo/Mac cells, *PLAUR*+ CAFs, basal and classical PDAC, and other cells.

(legend continued on next page)

(C) Heatmap showing *p* values matching the correlation matrix in Figure 2H.
(D) Representative image showing VIM+uPAR+PanCK+ cells surrounded by non-cancer cells (expressing αSMA or CD45 in cyan) (left) and histogram (right) showing the number of VIM+ tumor cells (see Table S3B for cell phenotyping) expressing or lacking uPAR in PDAC patients.
(E) Representative image showing uPAR+/FAP+/αSMA+ fibroblasts (left) and histogram (right) showing the number of uPAR+ fibroblasts co-expressing FAP in PDAC patients (see Table S3B for cell phenotyping).
(F) Violin plot showing uPAR activity score in myCAF, iCAF, and apCAF in public scRNA-seq datasets of hepatocellular carcinoma (LIHC), lung adenocarcinoma (LUAD), ovarian cancer (OV), and pancreatic cancer (PDAC).[35–38]
(G and H) Violin plots showing the indicated signature scores and single-gene expression in *PLAUR*-high versus *PLAUR*-low myeloid (G) and fibroblast (H) populations in the same scRNA-seq dataset as in (B). SASP (senescence-associated secretory phenotype).
(I) Violin plots comparing *PLAUR*-high versus *PLAUR*-low myeloid (left) and fibroblast (right) populations in terms of signature scores of progenitor-cell-proximal myeloid cells (left) and progenitor-cell-proximal fibroblasts (right), using signatures from Reyes et al.[39] Data on the indicated tumor types were obtained from public scRNA-seq datasets.
Statistics: Spearman correlation (A and C) and Wilcoxon test (F–I).

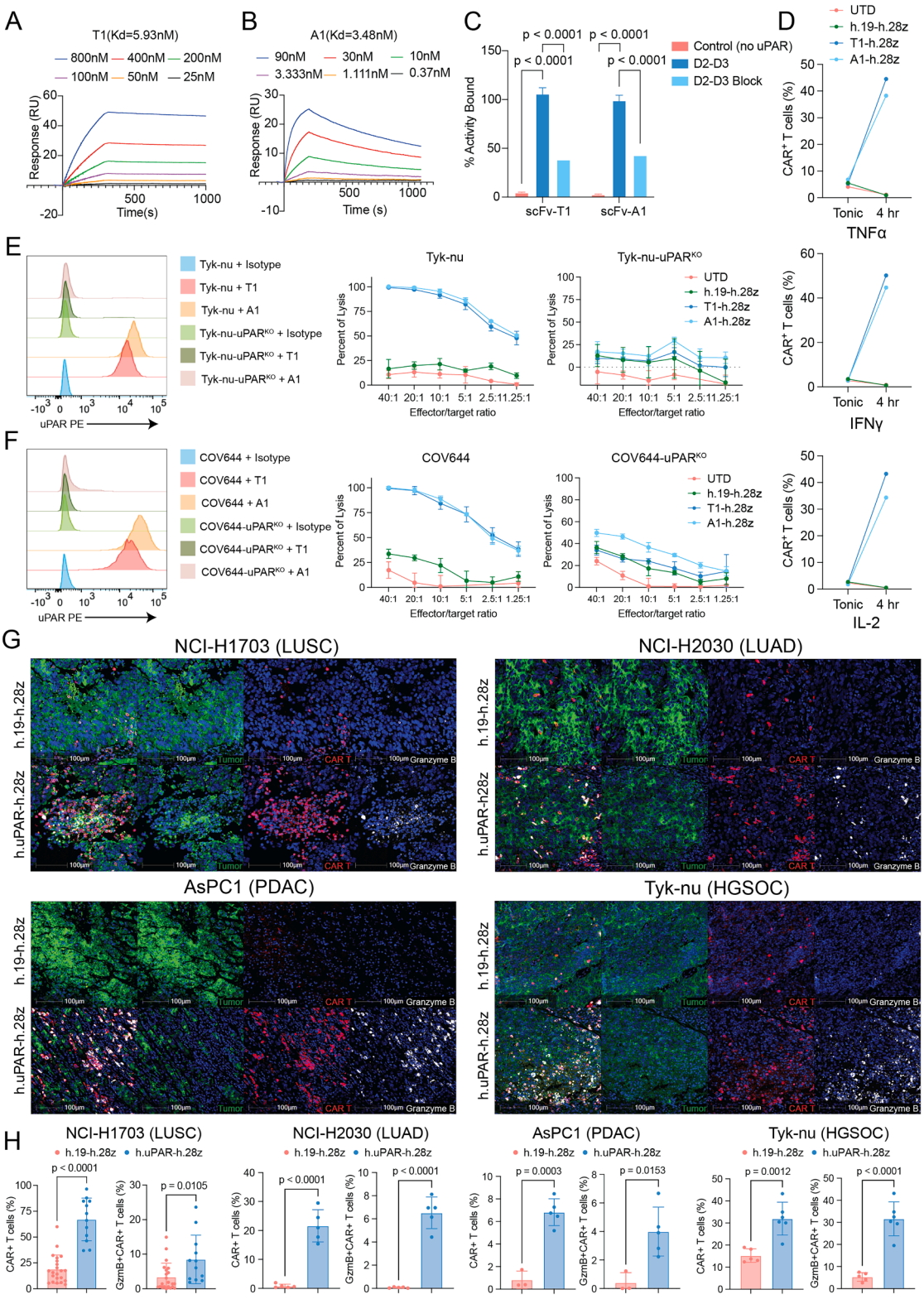

Figure S4. *In vitro* and *in vivo* characterization of uPAR CAR T cells, related to Figure 3

(A and B) Surface plasmon resonance (SPR) analysis of uPAR binding of T1 (A) or A1 (B) human uPAR single-chain fragment variants (scFvs).

(C) Bead binding assay of both A1 and T1 scFvs showing specific binding to the D2-D3 uPAR domain, which was blocked by the D2-D3 recombinant peptide.

(legend continued on next page)

(D) Flow cytometry plots showing percentage of CAR T cells expressing TNF-α (top), IFN-γ (middle), and IL-2 (bottom) in tonic and antigen-stimulated (4 h) conditions.
(E and F) Flow cytometry analysis of uPAR in Tyk-nu (E) or COV644 (F) and their uPAR KO derivatives using anti-uPAR T1 and A1 antibodies compared with isotype control (left) and cytotoxic activity of h.uPAR-CART cells were compared with untransduced T cells (UTD) or CD19 control CAR T cells using an 18 h bioluminescence assay with luciferase-expressing Tyk-nu, Tyk-nu-uPAR^{KO} (E) or COV644, COV644-uPAR^{KO} cells (F) (middle and right panels).
(G and H) Representative IF images of uPAR showing tumor cells (green), CAR T cells (CD3 staining, red), and granzyme B (white) (G), and quantification of CAR T cell infiltration (H) in four tumor xenograft models.
Statistical significance was determined using Student's *t* test (C and H). Error bars indicate SD (C and H) or SEM (E and F).

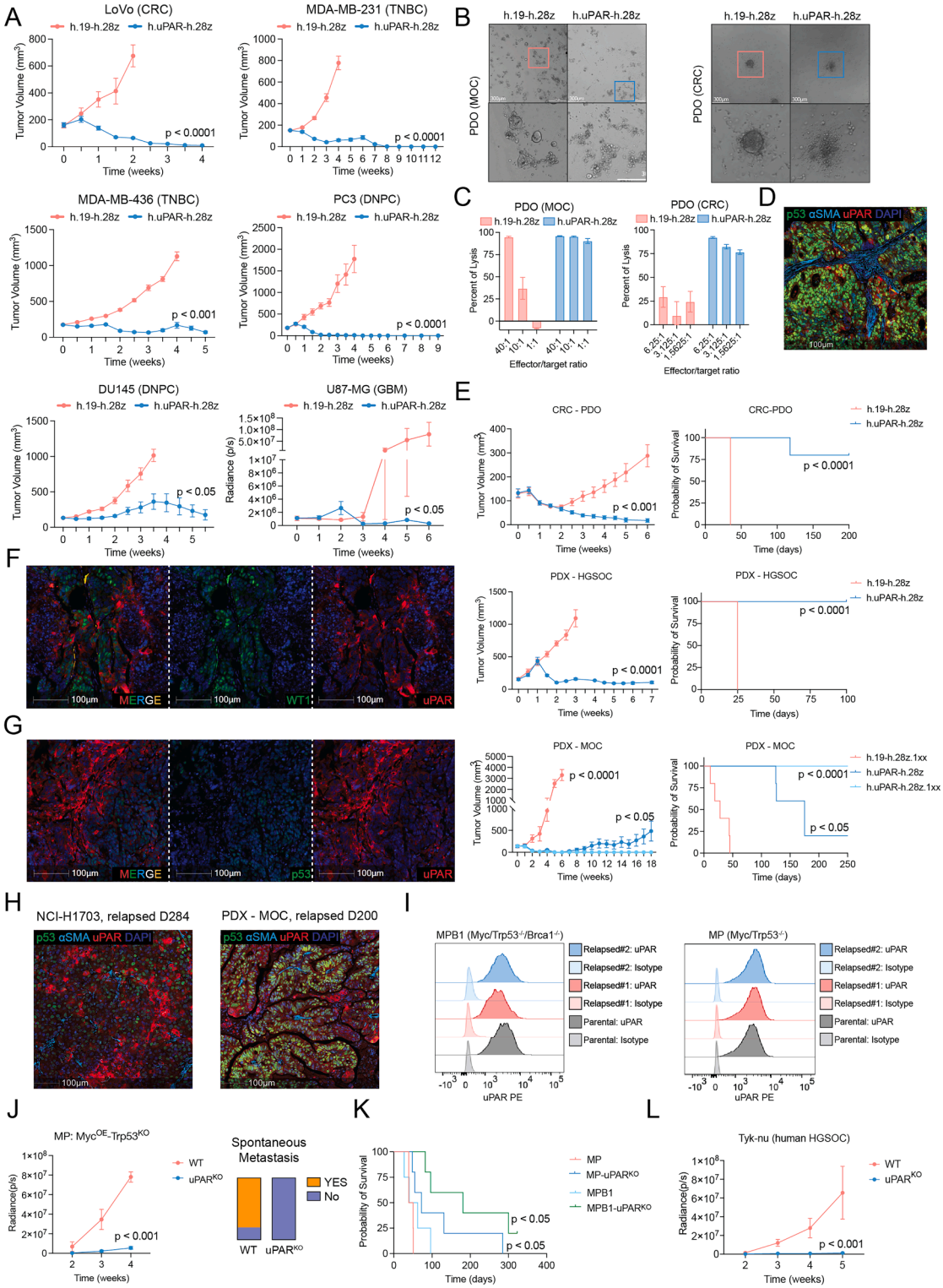

Figure S5. *In vitro* and *in vivo* characterization of uPAR CAR T cells, related to Figure 3

(A) Tumor growth curves of human cancer xenograft models treated with control h.19-h.28z CAR T cells or h.uPAR-h.28z CAR T cells. Shown are LoVo (CRC), MDA-MB-231 (triple-negative breast cancer [TNBC]), PC3 (double-negative prostate cancer [DNPC]), MDA-MB-436 (TNBC), DU145 (DNPC), and U87-MG (GBM) xenografts. Tumor volumes were measured over the indicated time courses.

(legend continued on next page)

(B) Bright-field images of patient-derived organoids (PDOs) from mucinous ovarian cancer (MOC, left) and colorectal cancer (CRC, right) after co-culture with h.19-h.28z or h.uPAR-h.28z CAR T cells. Boxes highlight representative regions of organoid disruption, shown at higher magnification below. Scale bars, 500 μm.
(C) Quantification of PDO cell lysis from MOC and CRC organoids after co-culture with h.19-h.28z or h.uPAR-h.28z CAR T cells at the indicated effector-to-target ratios.
(D) Representative IF staining of CRC tissue sections showing expression of uPAR (red), αSMA (cyan), and p53 (green). Scale bar, 100 μm.
(E) Tumor growth curves (left) and Kaplan-Meier survival analysis (right) for CRC PDO xenografts treated with h.19-h.28z or h.uPAR-h.28z CAR T cells.
(F) Immunofluorescence staining of HGSOC PDX tumors showing merged channels (left), WT1 (green, middle), and uPAR (red, right). Scale bars, 100 μm. The graphs show tumor growth curves and Kaplan-Meier survival analysis for the HGSOC PDX xenografts treated with h.19-h.28z or h.uPAR-h.28z CAR T cells.
(G) Immunofluorescence staining of MOC PDX tumors showing merged channels (left), p53 (green, middle), and uPAR (red, right). Scale bars, 100 μm. The graphs show tumor growth curves and Kaplan-Meier survival analysis for the MOC PDX xenografts treated with h.19-h.28z, h.uPAR-h.28z, or h.uPAR-h.28z 1XX CAR T cells.
(H) Representative IF staining of relapsed tumor samples from NCI-H1703 (relapse at day 284) and PDX-MOC (relapse at day 200), showing uPAR (red), αSMA (cyan), and p53 (green). Scale bars, 100 μm.
(I) Flow cytometry histograms showing uPAR surface expression in parental and relapsed tumor cells from MPB1 (Myc^{OE};$Trp53^{-/-}$;$Brca1^{-/-}$) and MP (Myc^{OE};$Trp53^{-/-}$) models. Overlays compare parental isotype, parental uPAR, relapsed isotype, and relapsed uPAR signals.
(J) Tumor growth curves (left) of MP (Myc^{OE};$Trp53^{KO}$) mouse ovarian tumors, either WT or $uPAR^{KO}$. Bar plot (right) shows the distribution of metastatic and non-metastatic disease for mice with WT versus $uPAR^{KO}$ tumors.
(K) Kaplan-Meier analysis shows survival of mice bearing MP or MPB1 tumors with and without uPAR KO. *p* values compare $uPAR^{KO}$ to uPAR WT.
(L) Tumor growth curve of Tyk-nu human HGSOC xenografts comparing WT versus $uPAR^{KO}$ tumors.
Statistical significance was determined using multiple *t* test (A; E, left; F, middle; G, middle; and J) and log-rank (Mantel-Cox) test (E, right; F, right; G, right; and K). Error bars indicate SEM.

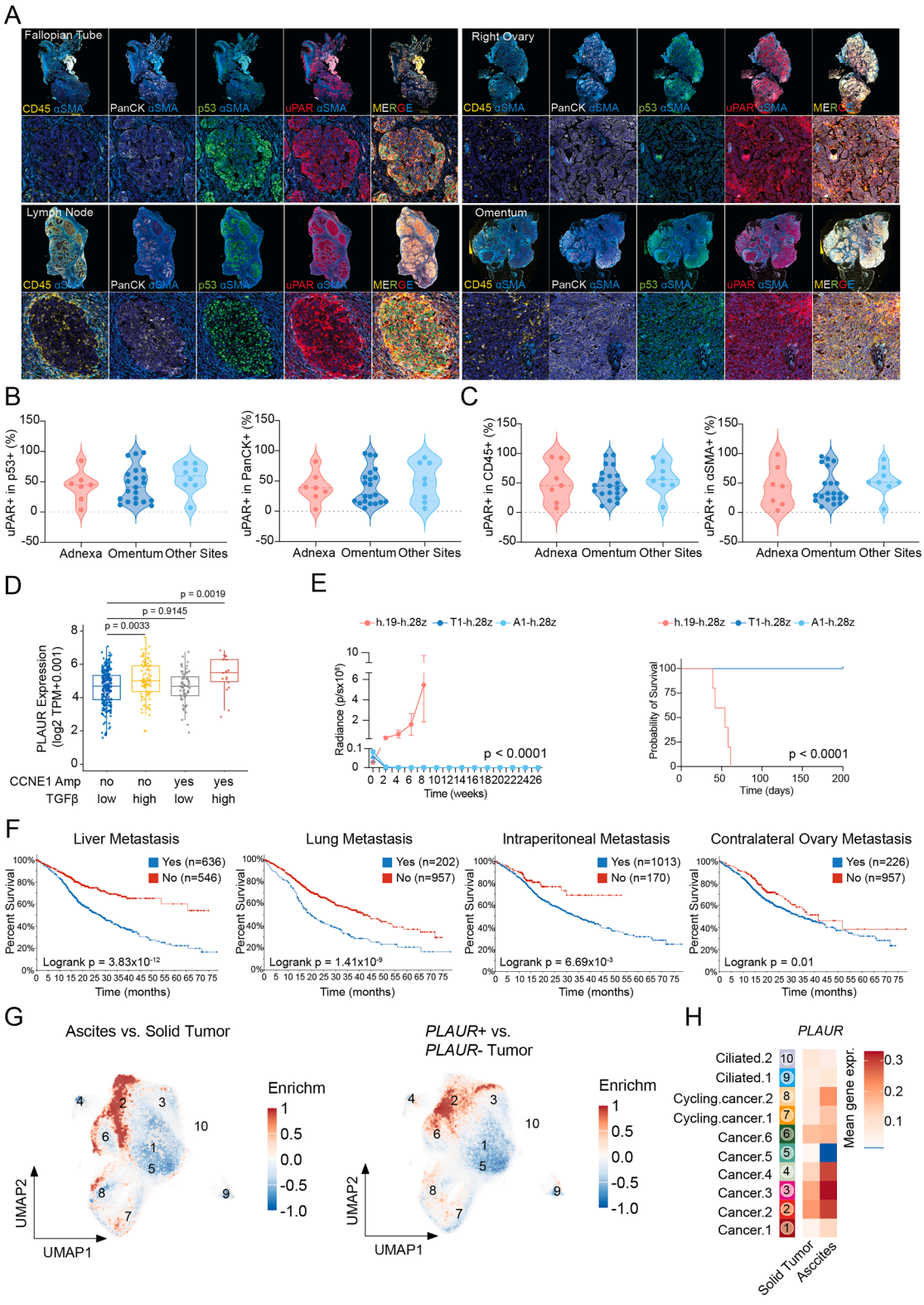

Figure S6. Efficacy of uPAR CAR T cells in ovarian cancer xenografts, related to Figure 4

(A) Representative multi-IF images of whole tissue sections of human HGSOC tumors (first and third rows) and zoomed-in views (second and fourth rows) from the primary tumor or the indicated metastatic sites.

(legend continued on next page)

(B and C) Violin plots of uPAR+ cells among p53+ cells (B, left), PanCK+ cells (B, right), $CD45^+$ cells (C, left), and αSMA+ cells (C, right). Adnexa (n = 7), omentum (n = 21), and other sites (n = 8).

(D) Box-and-whisker plots showing PLAUR transcript expression (log_2 TPM+0.001) in human ovarian tumors of the indicated genotypes.

(E) Radiance (bioluminescence) measurements (left) and Kaplan-Meier survival analysis (right) of mice bearing human ovarian xenografts ($COV644^{luc}$) treated with either control CAR T cells (UTD) or uPAR CAR T cells (T1-h.28z and A1-h.28z).

(F) Kaplan-Meier analysis of overall survival of HGSOC patients with versus without metastases at the indicated sites. Data are from the MSK pan-cancer metastasis cohort.[53]

(G) Enrichment of ascites versus primary and metastatic solid tumors. Left, Uniform Manifold Approximation and Projection (UMAP) shows kernel density estimates of cancer cells in ascites, highlighting the enrichment of specific cell states in ascites versus solid tumor sites. Right, UMAP shows *PLAUR* expression across malignant and non-malignant epithelial cells in the SPECTRUM cohort.

(H) Heatmap of average *PLAUR* gene expression per site in samples from the SPECTRUM cohort (n = 160 tumor sites from 42 patients).

Statistical significance was determined using the Wilcoxon pairwise comparison (D), multiple t test (E, left), and log-rank tests (E, right, and F). Error bars indicate SEM (E).

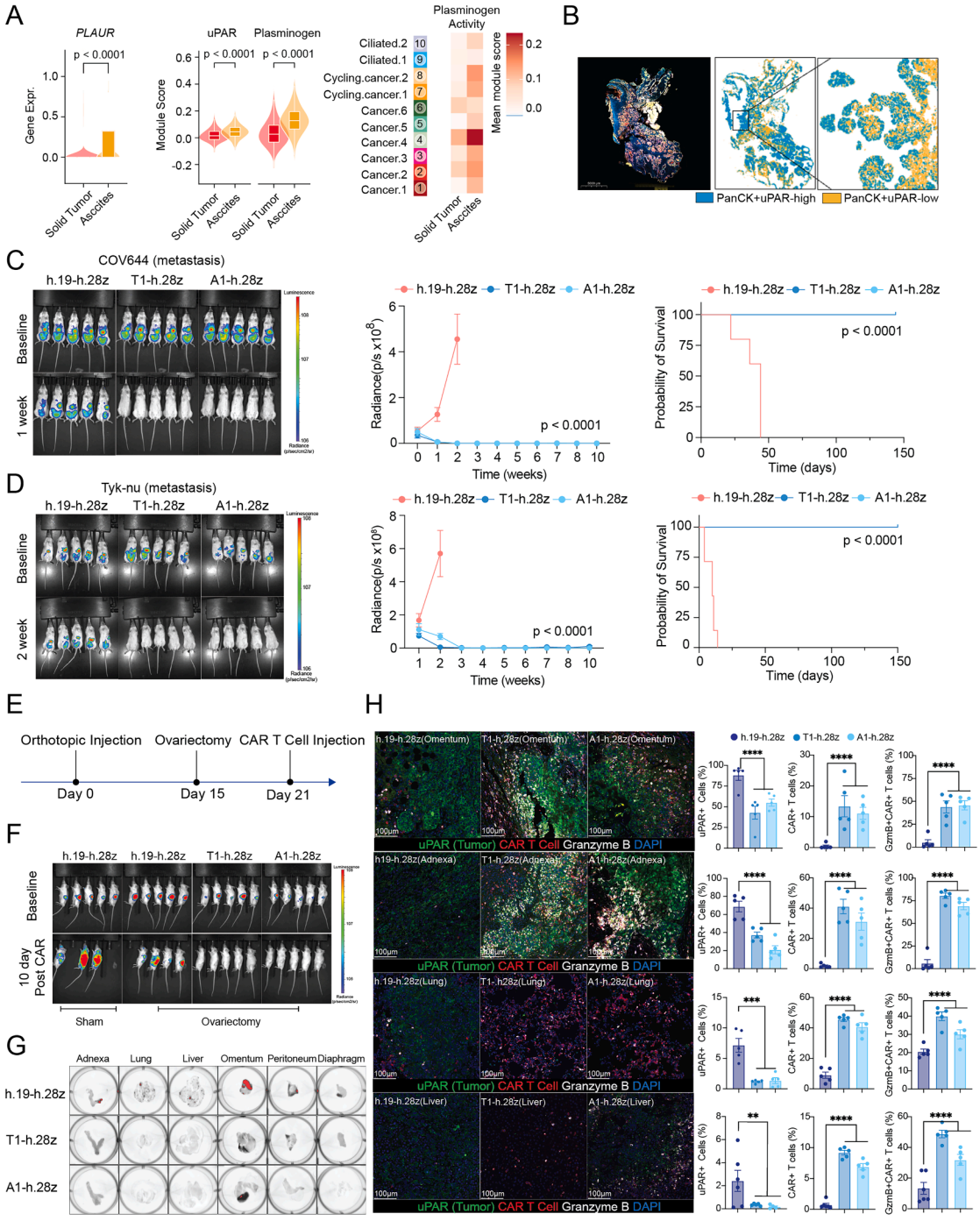

Figure S7. Efficacy of uPAR CAR T cells in ovarian cancer xenografts, related to Figure 4

(A) Violin plots with integrated boxplots showing median *PLAUR* expression (left panel), median module scores for uPAR activity and plasminogen signatures (middle panel), and a heatmap showing average signaling pathway activity scores per site calculated across cancer cells per sample in the SPECTRUM cohort.

(B) Multi-IF (left), spatial plot (middle), and zoomed-in spatial plot (right) showing the location of uPAR+ tumor cells in human HGSOC tumors, including in detached clusters.

(C) Bioluminescence images reflecting tumor burden (left), tumor volume (middle), and Kaplan-Meier survival analysis (right) of metastatic human ovarian xenografts (COV644^{luc}) treated with either 2 × 10^6 control CAR T cells (h.19-h.28z) or the same number of uPAR CAR T cells (T1-h.28z and A1-h.28z).

(D) Bioluminescence images reflecting tumor burden (left), time course of tumor volume (middle), and Kaplan-Meier survival analysis (right) of mice bearing metastatic human ovarian xenografts (Tyk-nu^{luc}) treated with either 2 × 10^6 control CAR T cells (h.19-h.28z) or the same number of uPAR CAR T cells (T1-h.28z or A1-h.28z).

(legend continued on next page)

(E) Experimental design for adjuvant CAR T cell therapy after oophorectomy.
(F) Bioluminescence images of mice before and after receiving CAR T cell treatment with or without prior oophorectomy.
(G) *Ex vivo* fluorescence imaging of adnexa, lung, liver, omentum, peritoneum, and diaphragm from tumor-bearing mice treated with control (h.19-h.28z) or h.uPAR CAR T cells (T1 and A1).
(H) Representative multi-IF images showing uPAR (tumor cells, green), CD3 (CAR T cells, red), and granzyme B (white) (left) and quantification (right) of metastatic tumors in lung, liver, adnexa, and omentum 1 week after treatment with h.uPAR CAR T (T1 and A1) or control CAR T cells (h.19-h.28z).
Statistical significance was determined using the log-rank test (C, right; D, right), the Wilcoxon pairwise comparison (A), the multiple *t* test (C, middle; D, middle), and the one-way ANOVA test (H). Error bars indicate SEM (C, D, and H).

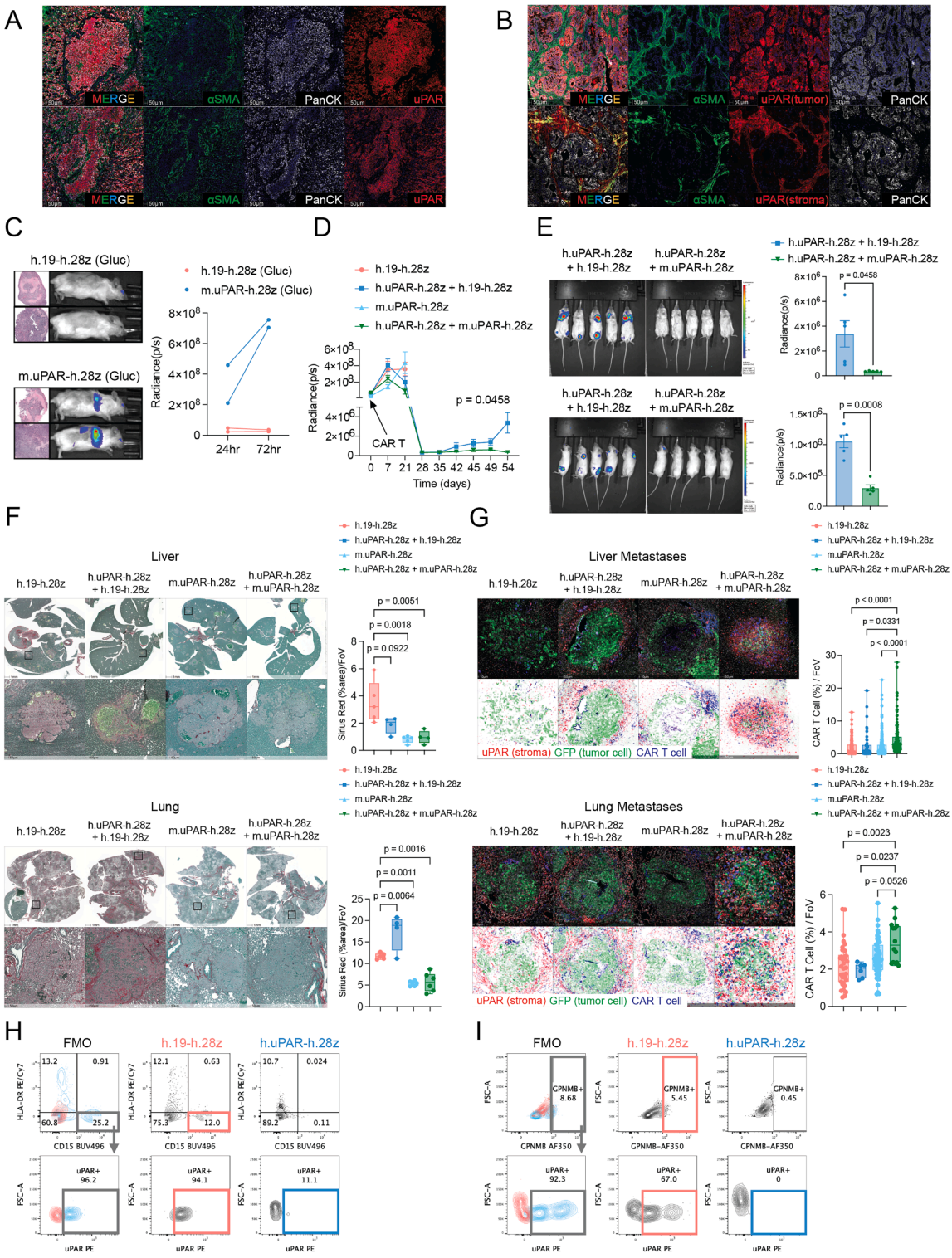

Figure S8. uPAR CAR T cells eliminate immunosuppressive stromal cells, related to Figure 5

(A) Multi-IF images of Tyk-nu tumors showing αSMA+ stromal regions (green), PanCK+ tumor epithelium (white), uPAR expression (red), and DAPI (blue). Merged and individual channels are shown (scale bar, 50 μm).

(B) Multi-IF images highlighting uPAR expression in COV644 tumor cells (uPAR+/PanCK+) and stromal cells (uPAR+/αSMA+) within fibrotic regions (scale bar, 50 μm). A human-specific uPAR antibody was used to detect tumor cells, and murine-specific uPAR antibody was used to detect stromal cells.

(legend continued on next page)

(C) Representative H&E and bioluminescence images of mice bearing subcutaneous head & neck PDX tumors treated with Gluc-labeled h.19-h.28z or m.uPAR-h.28z CAR T cells at 24 h post CAR T cell administration. Quantification of radiance at 24 and 72 h is shown.
(D) Longitudinal tumor radiance measurements following treatment with the indicated human or murine uPAR CAR combinations. The CAR T infusion time point is indicated. *n* = 2 mice per group.
(E) *In vivo* bioluminescence images of mice bearing Tyk-nu orthotopic (top) and metastatic (bottom) tumors treated with single or dual human/murine uPAR CAR T combinations at day 54. Quantification of radiance for each treatment group is shown on the right. *n* = 5 mice per group.
(F) Representative Sirius red-stained sections of liver and adnexa from mice treated with h.19-h.28z, h.uPAR-h.28z, m.uPAR-h.28z, or combined human + murine uPAR CARs. Box-and-whisker plots (right) show fibrosis area (%) for each tissue and treatment condition. *n* = 5 mice per group.
(G) Multiplex IF images of liver metastases (top) and adnexa (bottom) showing uPAR$^+$ stromal cells (red), GFP$^+$ tumor cells (green), and CAR T cells. Corresponding quantification (right) shows CAR T cell density per field for each treatment group. *n* = 5 mice per group.
(H and I) Flow cytometry analysis of (H) uPAR+ polymorphonuclear myeloid-derived suppressor cells (PMN-MDSCs) and (I) uPAR+GPNMP+ myeloid cells following 16 h co-culture of dissociated human lung tumor tissue with control CAR T cells (h.19-h.28z) or uPAR CAR T cells (h.uPAR-h.28z). PMN-MDSCs were defined as CD45$^+$Lin−CD11b+CD14−HLA−DR−CD15+, where Lin− excludes CD3+CD19+CD56$^+$ cells. Myeloid cells were gated from CD45+Lin−CD11b+ populations. Positive gates were determined using FMO controls. *n* = 1 human lung tumor.
Statistical significance was determined using Student's *t* test (E), multiple *t* test (D), and one-way ANOVA (F and G). Error bars indicate SEM (D) or SD (E).

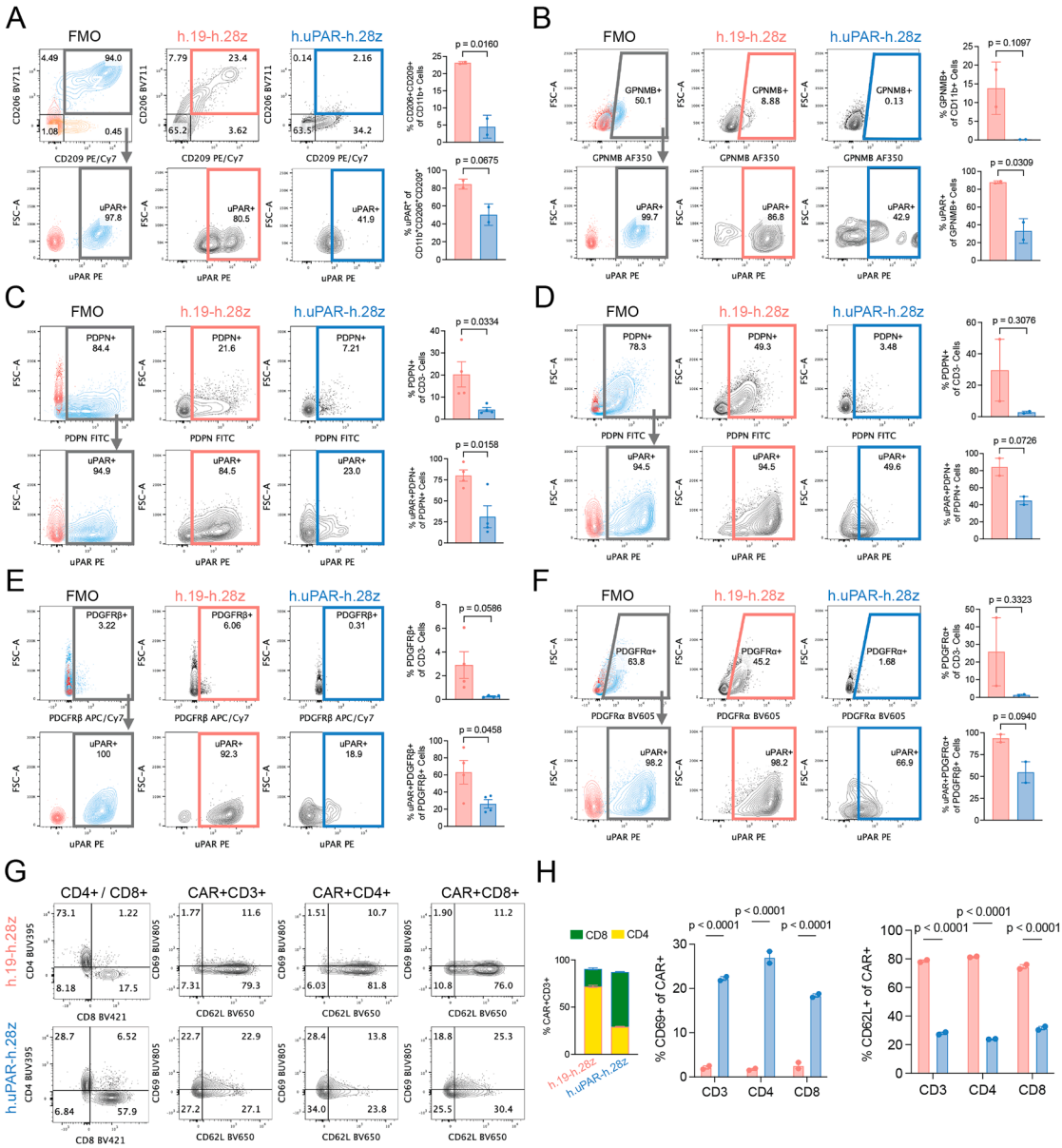

Figure S9. uPAR CAR T cells eliminate immunosuppressive stromal cells, related to Figure 5

(A and B) Flow cytometry of *in vitro*-differentiated human M2-like macrophages following 16 h co-culture with the indicated CAR T cells. The plots show (A) representative gating and quantification of CD206+/CD209+ cells among CD11b+ macrophages and uPAR+ cells within the CD206+/CD209+ subset, as well as (B) GPNMB+ cells among CD11b+ macrophages and uPAR+ cells within the GPNMB+ subset. Positive gates were determined using FMO controls. $n = 2$ donors.

(C and D) Flow cytometry of PDPN+ primary CAFs from HGSOC ($n = 4$; C) and CRC ($n = 2$; D) patients following 16 h *in vitro* co-culture with the indicated CAR T cells. The plots show representative gating and quantification of PDPN+ cells among CD3- stromal cells and uPAR+ cells within the PDPN+ compartment. Positive gates were determined using FMO controls.

(E and F) Flow cytometry of PDGFRβ+ primary CAFs from HGSOC ($n = 4$; E) and PDGFRα+ CAFs from CRC ($n = 2$; F) patients following 16 h *in vitro* co-culture with the indicated CAR T cells. Representative gating plots are shown, with quantification of PDGFRβ+ or PDGFRα+ cells among CD3− stromal populations and uPAR+ fractions within each CAF subset. Positive gates were determined using FMO controls.

(G and H) Flow cytometry analysis of CAR-T cells following co-culture with primary CRC CAFs ($n = 2$).

(G) Representative flow cytometry plots showing the percentages of CD4+ and CD8+ CAR T cells, as well as CD69+/CD62L+ cells within the CD4+ or CD8+ CAR T populations.

(H) Quantification of the data shown in (G). CAR expression was assessed by LNGFR staining.

Statistical significance was determined using Student's *t* test (A–F) and one-way ANOVA (H). Error bars indicate SD.

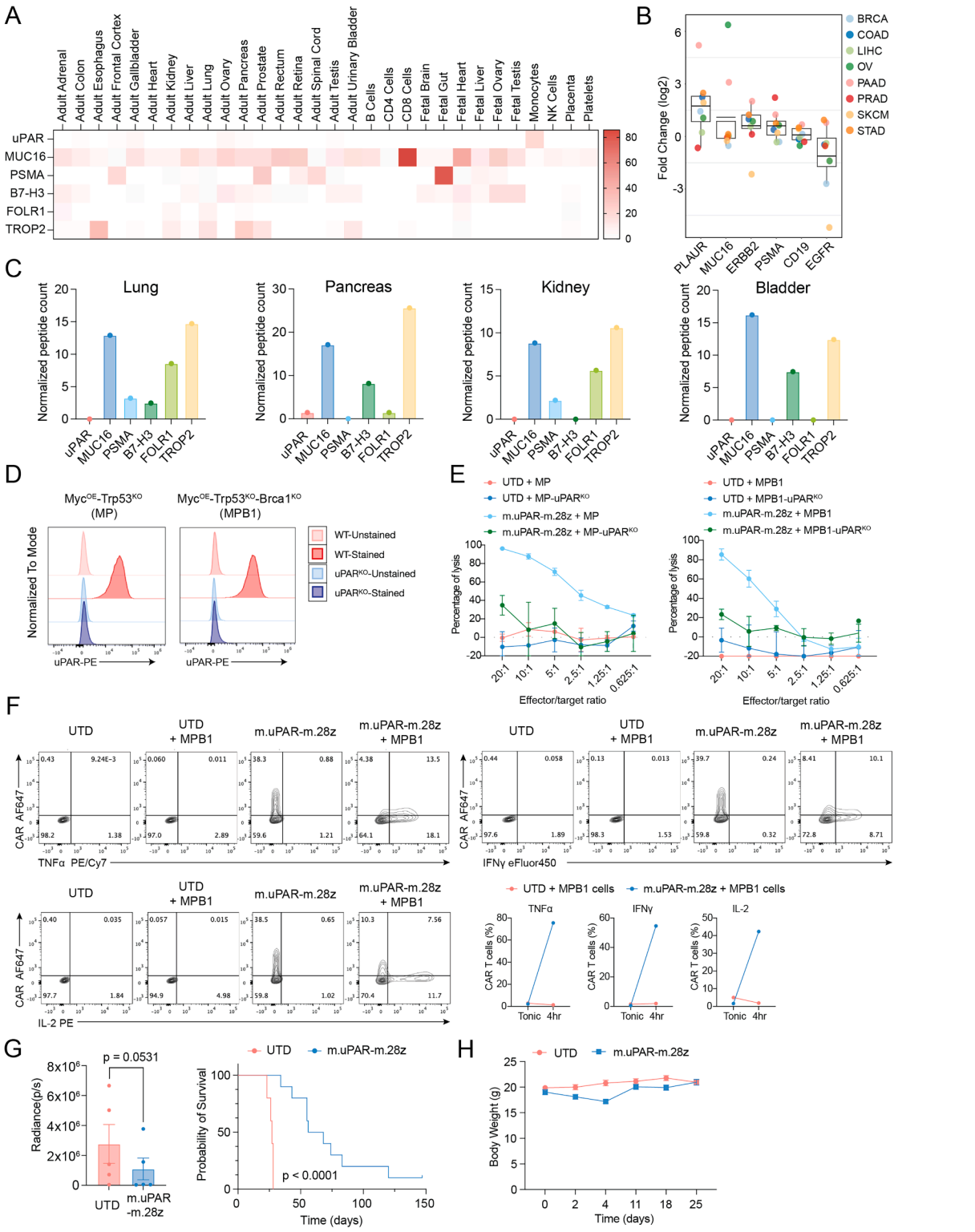

Figure S10. uPAR CAR T cells exhibit a favorable safety profile, related to Figure 6

(A) Heatmap showing uPAR and other clinically targeted surface protein expression in healthy tissues (data from Human Protein Atlas, normalized peptide counts in Table S1H).

(legend continued on next page)

(B) Boxplot showing upregulation of *PLAUR* (from TCGA) across different cancers compared with their matched normal tissue (using the GTEx dataset), in comparison with other surface proteins. Each colored dot represents an individual cancer type.
(C) Normalized peptide count of data from (B) in healthy human lung, pancreas, kidney, and bladder. BRCA, breast invasive carcinoma; COAD, colon adenocarcinoma; LIHC, liver hepatocellular carcinoma; OV, ovarian serous cystadenocarcinoma; PAAD, pancreatic adenocarcinoma; PRAD, prostate adenocarcinoma; SKCM, skin cutaneous melanoma; STAD, stomach adenocarcinoma.
(D) Flow cytometry analysis of uPAR expression in *MYC*^{OE};*Trp53*^{KO} (MP) and *MYC*^{OE};*Trp53*^{KO}-*Brca1*^{KO} (MPB1) cells, along with their uPAR-KO derivates as negative controls.
(E) Cytotoxic activity of control T cells (UTD) or murine uPAR CAR T cells on luciferase-expressing MP, MP-uPAR^{KO} (left) and MPB1, MPB1-uPAR^{KO} (right) cells, assessed using an 18 h bioluminescence assay.
(F) Flow cytometry plot (left) and quantification (right) of TNF-α, IFNγ, and IL-2 in murine uPAR CAR T cells with or without stimulation with MPB1 tumor cells.
(G) Radiance measurements (left) and Kaplan-Meier survival curves (right) of mice bearing ovarian MPB1 intraperitoneal metastatic tumors treated with 2 million control (UTD) or m.uPAR-m.28z CAR T cells.
(H) Body weight analysis of the mice in (G).
Statistical significance was determined using Student's *t* test (G, left) and the log-rank test (G, right). Error bars indicate SEM (H) or SD (other panels).

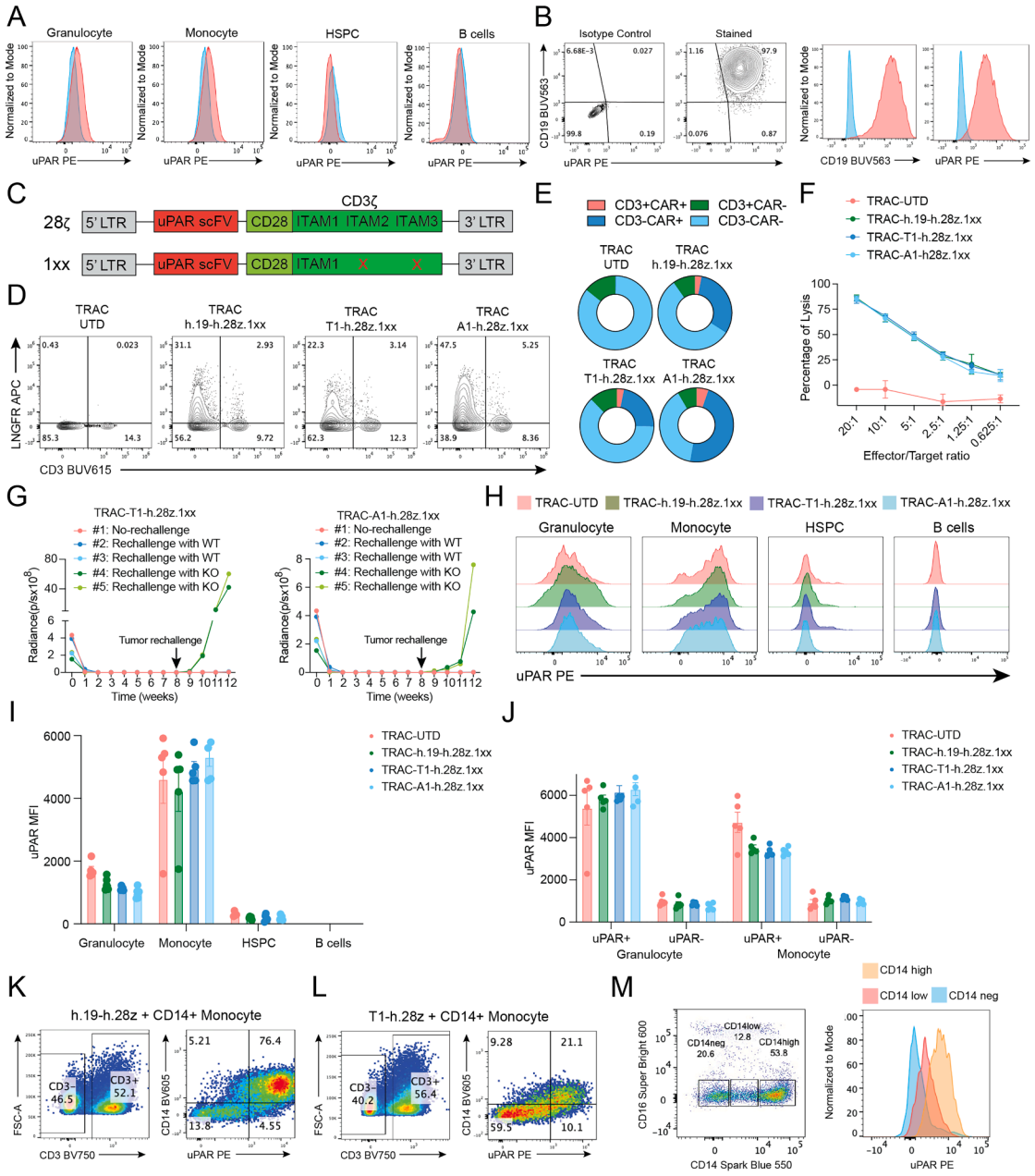

Figure S11. Safety evaluation using mice with humanized immune system, related to Figure 6

(A) Flow cytometry analysis of human CD45+ cells showing uPAR expression in immune cell subpopulations from bone marrow in humanized immune system mice at baseline.

(B) Flow cytometry analysis of Tyk-nu cells with ectopic CD19 expression, confirming uPAR and CD19 expression.

(C) Schematic showing human uPAR CAR T cell designs: 28ζ (CD28-CD3ζ) and 28ζ-1XX (CD28-CD3ζ with ITAM2/3 inactivated).[50]

(D) Flow cytometry plot showing expression of CD3 and LNGFR (marker for CAR) in TRAC-edited human T cells.

(E) Pie charts showing the proportions of T cells with surface expression of CD3 and CAR after TRAC editing: CD3-CAR+ (TRAC-edited CAR T), CD3+CAR+ (unedited CAR T cells), CD3+CAR− (WT T cells), and CD3-CAR− (TRAC-edited WT T cells).

(F) Cytotoxic activity of CAR T cells derived from TRAC-edited human T cells against luciferase-expressing Tyk-nu cells, assessed using an 18 h bioluminescence assay.

(G) Radiance measurement reflecting tumor burden in mice with a humanized immune system and rechallenged with Tyk-nu or Tyk-nu-uPAR^{KO} cells.

(H) Representative flow cytometry histograms showing uPAR expression on the indicated cell types at 1 week post-treatment with 1 × 10^6 of control (TRAC-UTD), TRAC-edited CD19-CAR T (TRAC-h.19-h.28z.1XX), or TRAC-edited uPAR-CAR T (TRAC-h.uPAR-h.28z.1XX CAR T cells [T1 or A1]).

(I) Bar plot showing uPAR median fluorescence intensity (MFI) in human immune cells 1 week post-treatment with TRAC-edited untransduced or CAR T cells.

(legend continued on next page)

(J) Bar plot showing uPAR expression (MFI) in uPAR^{+} or uPAR^{-} granulocytes and monocytes 1 week post-treatment with TRAC-edited UTD or CAR T cells.
(K and L) Representative flow cytometry plots showing effects of co-culturing freshly isolated human primary CD14^{+} monocytes from peripheral blood mononuclear cells with (K) h.19-h.28z or (L) h.uPAR-h.28z CAR T cells.
(M) Flow cytometry plots showing expression of uPAR in CD14^{neg}, CD14^{low}, and CD14^{high} monocyte populations from bone marrow of humanized mice.
Error bars indicate SD (F) or SEM (I and J).

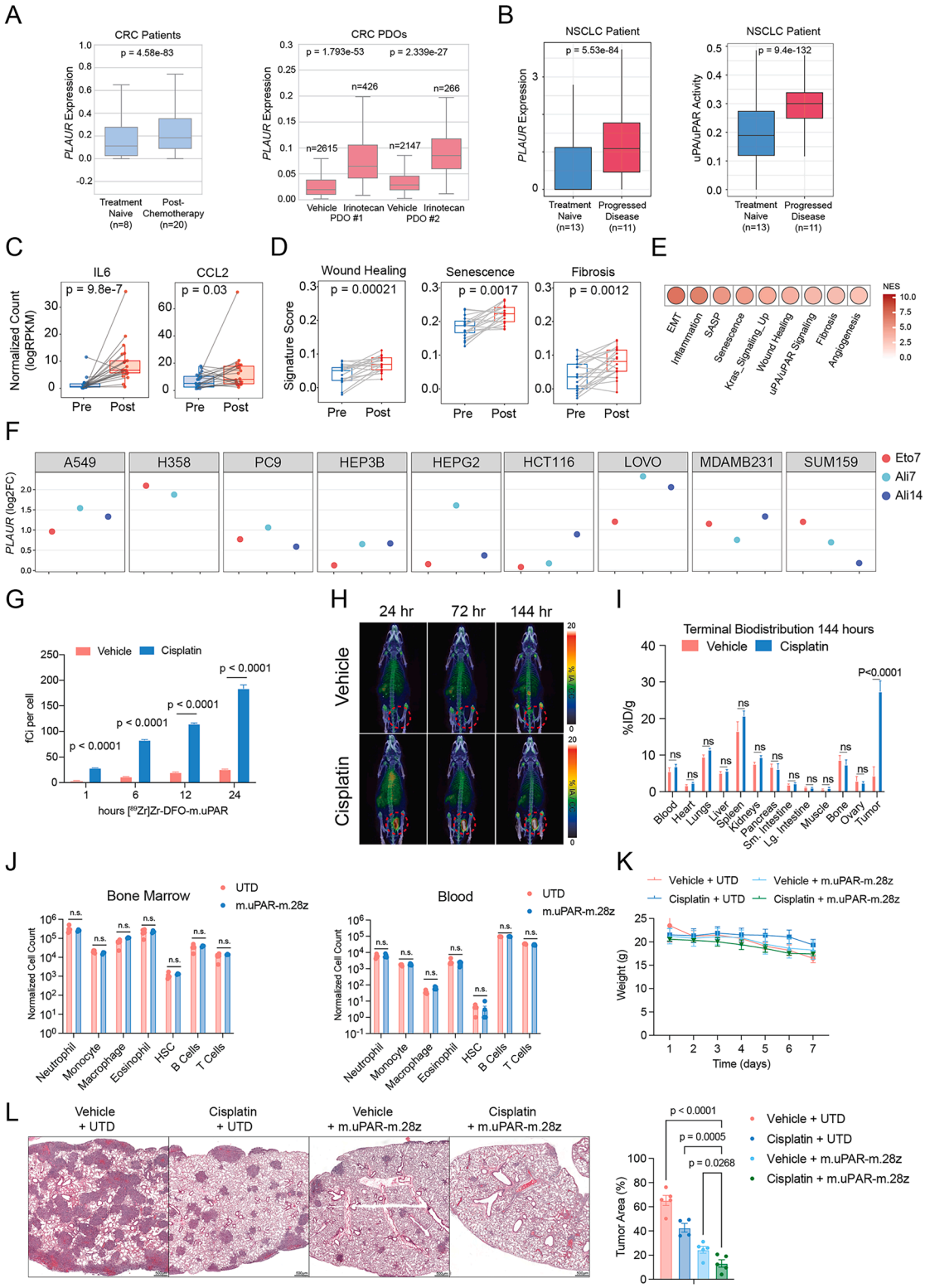

Figure S12. Therapy-induced senescence enhances uPAR CAR T efficacy, related to Figure 7

(A) scRNA-seq analysis of *PLAUR* expression in the tumor-cell clusters from CRC patients (left)[77] and CRC PDOs (right) treated with irinotecan (1 μM).

(B) scRNA-seq analysis of *PLAUR* expression (left) and uPAR activity signature score (right) in NSCLC patients with disease progression after treatment with the tyrosine kinase inhibitor osimertinib (EGFR inhibitor) or alectinib (ALK inhibitor)[78]

(legend continued on next page)

(C and D) Boxplots from bulk RNA-seq showing expression of senescence-associated secretory factors IL-6 and CCL2 (C) and wound-healing, senescence, and fibrosis signature scores (D) in matched treatment-naive versus chemotherapy-treated ovarian cancer patients.[61]
(E) Dot plot showing signaling pathway enrichment score in *in vitro* MPB1 cells treated with cisplatin versus vehicle control.
(F) Analysis of *PLAUR* expression from bulk RNA-seq in 9 human cell lines treated with etoposide for 7 days (Eto7) or alisertib for 7 and 14 days (Ali7 and Ali14) compared with vehicle control.[26]
(G) Uptake of radiolabeled uPAR antibody *in vitro* in MPB1 cells treated with cisplatin or vehicle.
(H) uPAR PET imaging with [^{89}Zr]Zr-DFO-m.uPAR showing increased uPAR signal on MPB1 tumors of mice treated with cisplatin compared with vehicle control.
(I) Terminal biodistribution analysis at 144 h post-treatment (related to H).
(J) Bar graph of results from flow cytometry analysis of different immune cell populations in bone marrow (left) and blood (right) at 30 days post-treatment with untransduced T cells vs. m.uPAR CAR T cells.
(K) Body weight of MPB1 tumor-bearing mice treated with the indicated therapies. $n = 5$ mice per group.
(L) Representative H&E images (left) and quantification (right) of murine *Kras*^{G12D}/*Trp53*^{R172H} lung tumor burden treated with cisplatin (3 mg/kg), untransduced T cells (UTD), m.uPAR-m.28z CAR T cells (1×10^6), or the combination. Lung tissues were collected 1 week post-treatment.
Statistical significance was determined using the Wilcoxon test (A–D) and Student's *t* test (G, I, J, and L). Error bars indicate SEM (J) or SD (other panels).